Evolution and molecular properties of bacterial actin MreB involved in *Spiroplasma* swimming

(スピロプラズマ遊泳運動にかかわる

細菌アクチン MreB の進化と分子特性)

理学研究科

生物地球系専攻

令和 4 年度

DAICHI TAKAHASHI

(高橋 大地)

Abstract

Actin superfamily is a group of cytoskeletal proteins important for viability of most organisms. MreB is an actin superfamily protein conserved for the bacterial kingdom. It polymerizes into a non-helical filament, in which two protofilaments interact each other in an antiparallel manner. Many bacteria possess one MreB isoform as a key factor of a protein complex for synthesizing bacterial cell-wall peptidoglycan, although MreBs are even found in wall-less bacteria. *Spiroplasma* is a genus of bacteria characterized by wall-less helical cell morphology. *Spiroplasma* species swim in a viscous liquid by transmitting the switching of their cell helicities from the cell tips to the ends without relying on conventional types of bacterial motility machinery such as flagellum. Five classes of *Spiroplasma* MreB isoforms (SMreB1–5) probably have distinct roles for driving *Spiroplasma* swimming. Here, I analyzed the evolution and properties of SMreBs to clarify the origin and molecular mechanism of *Spiroplasma* swimming. Phylogenetical analyses using an amino acid sequence set suggest that all SMreBs have evolved from an MreB isoform which is conserved for related species of *Bacillus subtilis* and is not essential for their viability. Sequence comparisons suggest that each class of SMreBs is distinct for the polymerization abilities, ATPase activities, and membrane binding properties. Next, I recombinantly expressed, purified, and analyzed SMreB5, which is one of the essential SMreBs for *Spiroplasma* swimming, and SMreB3, which is phylogenetically distinct from the other classes of SMreBs. Both SMreBs possessed distinct properties for filament structures, ATPase activities, polymerization activities, and bundle formation. These results indicate that *Spiroplasma* swims by cooperating with SMreBs having different properties. During these studies, I constructed models for the polymerization dynamics coupled with reaction steps of ATPase and ATP hydrolysis

mechanism including a proton elimination step for, to the best of my knowledge, the first time in MreB family proteins. Based on these findings, I discuss a molecular mechanism of *Spiroplasma* swimming and evolution of SMreBs and, moreover, actin superfamily proteins.

Contents

Abbreviations and Acronyms

I will use the following abbreviations and acronyms in this thesis.

2D: two-dimensional

3D: three-dimensional

AMPPNP: 5'-adenylylimidodiphosphate

BMreB: *Bacillus* MreB

BMreBH: *Bacillus* MreBH

CcMreB: *Caulobacter crescentus* MreB

CHES: *N*-cyclohexyl-2-aminoethanesulfonic acid

CPR: candidate phyla radiation

DMAB: dimethylamine borane

DTT: (+/−)-dithiothreitol

EcMreB: *Escherichia coli* MreB

EDTA: 2,2',2'',2'''-(ethane-1,2-diyldinitrilo)tetraacetic acid

EM: electron microscopy

HEPES: 4-(2-hydroxyethl)-1-piperazineethanesulfonic acid

HMreB: *Haloplasma* and *Candidatus* Izimaplasma MreB

IPTG: isopropyl β-D-thiogalactopyranoside

LB: "Luria broth" or "lysogeny broth"

MALDI-TOF: matrix assisted laser desorption/ionization-time of flight

MD: molecular dynamics

MES: 2-morpholinoethanesulfonic acid

MESG: 2-amino-6-mercapto-7-methylpurine riboside

MR: molecular replacement

N.D.: not detected

Nf: nucleotide free

NTA: nitrilotriacetic acid

OD_{600}: optical density at 600 nm light

PARSE: parameters for solvation energy

PDB: protein data bank

PEG: polyethylene glycol

P_i: phosphate ion

RMSD: root mean square deviation

S.D.: standard deviation

SMreB: *Spiroplasma* MreB

SciMreB: *Spiroplasma citri* MreB

SpeMreB: *Spiroplasma eriocheiris* MreB

TmMreB: *Thermotoga maritima* MreB

Tris: 2-amino-2-hydroxymethyl-propane-1,3-diol

General Introduction

Bacterial cytoskeleton

Cytoskeleton is an intracellular network structure built by polymerized proteins (1). Owing to these structures, cells are shaped to various morphologies, unlike spherical liposomes (2-6). Cytoskeletal filaments do not only stay static but also repeat polymerizations and depolymerizations (7-13). These dynamics supply mechanical forces to power various biological phenomena (6, 14-19). Eukaryotic cytoskeletal proteins are divided into three types: actin, tubulin, and intermediate filament (1). Actin is composed of four subdomains (subdomains 1, 2, 3, and 4 or IA, IB, IIA, and IIB) (Fig. 1A) and forms right-handed double-stranded filaments which repeat polymerizations and depolymerizations using ATP (Fig. 1B) (12, 13, 20-23). Actin is one of the most abundant proteins in vertebrate cells (5–10% of the protein mass amounts), and its intracellular concentration is up to 150–200 μM (24, 25). By orchestrating with over 100 of actin-binding proteins, actin participates in various phenomena such as cell motility, cytokinesis, and endocytosis (6, 26, 27). Therefore, actin has been actively studied since its discovery in 1942 (22, 23), and the publication number by a PubMed search on "actin" is as many as around 140,000 in late October 2022. One of the intriguing features of actin filaments is the distinct properties of those ends in which one (barbed-end or plus-end) grows and shrinks fast and the other (pointed-end or minus-end) is static (Fig. 1B) (8, 9, 12, 13). This asymmetric feature is important for phenomena that require polarity, such as cell migration (6, 15, 19, 27).

Until the 1990s, it had been thought that the cytoskeleton is specific for eukaryotes and absent in prokaryotes. However, this consensus was overthrown by the discoveries of bacterial proteins FtsZ and MreB. In the early 1990s, several groups reported that FtsZ

is a GTPase assembled onto the division plane of bacteria (28-32). The following structural analyses revealed that FtsZ belongs to the tubulin superfamily (33-35). In 1992, Bork *et al*. predicted that MreB has similar structural features to actin (36). Nine years after this report, MreB was proved to belong to the actin superfamily and form filamentous structures in bacterial cells (Fig. 1C and D) (37, 38).
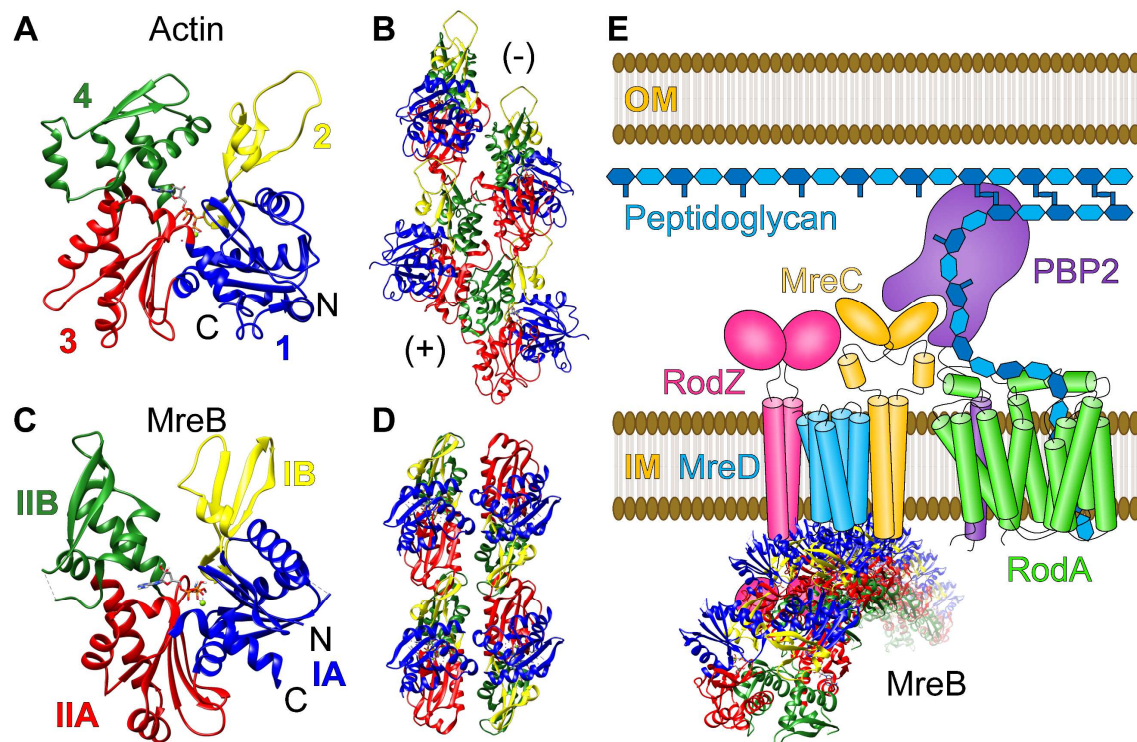
Figure 1. Structures and functions of actin and MreB. (**A**) An actin subunit structure. Subdomains 1, 2, 3, and 4 are colored blue, yellow, red, and green, respectively. The N- and C-termini are labeled on the structure. A nucleotide binds to the cleft among the four subdomains. (**B**) The structure of an actin filament with four subunits. Its barbed and pointed ends are labeled by (+) and (−), respectively. (**C**) An MreB subunit structure. Subdomains IA, IB, IIA, and IIB are colored blue, yellow, red, and green, respectively. The N- and C-termini are labeled on the structure. A nucleotide binds to the cleft among the four subdomains. (**D**) The structure of an MreB filament with four subunits. The actin and MreB structures are referred from PDB ID 6DJM and 4CZJ, respectively. (**E**) The schematic diagram of an elongasome complex in a Gram-negative bacterium in which the cell compartment is composed of the outer membrane (OM), a peptidoglycan layer, and the inner membrane (IM).

After 30 years of their discoveries, several dozens of prokaryotic cytoskeletal

proteins have been now reported to be involved in various phenomena of prokaryotes (39-41). The bacterial cell divisions are driven by the divisome complex including FtsZ filaments and its membrane anchor FtsA which is a member of the actin superfamily (42, 43). The bacterial cell shapes (especially those with elongated morphologies) are mediated by the elongasome complex which is composed of bacterial cell wall (peptidoglycan) synthases assembled on membrane-bound MreB filaments (Fig. 1E) (44). Segregations of low-copy number plasmids to the daughter cells often require dynamics of a bacterial tubulin TubZ or bacterial actins ParM or AlfA (45-50). Magnetotactic bacteria use the dynamics of a bacterial actin MamK to align magnetosomes, which are the organelle for sensing magnetism (51, 52). Archaeal cytoskeletal proteins have been less characterized due to the difficulty of cultivation for many species (53). However, two research groups reported that FtsZs in *Haloferax volcanii* and *Methanobrevibacter smithii* in the phylum Euryarchaeota are involved in their cell divisions (54-56). A recent study reported that filaments of lokiactin in the superphylum Asgardarchaeota support tentacle-like cellular protrusions (57). Although cellular functions have not been reported, crenactin from the phylum Crenarchaeota and odintubulin from the superphylum Asgardarchaeota take monomeric structures like corresponding homologs in eukaryotes and polymerize depending on nucleotides (58-62). These researches have revealed that prokaryotes have obtained various kinds of cytoskeletal proteins each of which has a few cellular functions for their viability, unlike eukaryotes, which have limited kinds of cytoskeletal proteins involved in countless phenomena (39, 40). As a result of their diversity, the filament structures of prokaryotic cytoskeletal proteins are also diverse (39, 63). Prokaryotic tubulin filaments are diverse in the number of protofilaments which are the unit of the longitudinally assembled subunits (64-67). In contrast, prokaryotic actin

filaments are diverse in phase shifts in inter-subunit interactions, filament helicities, and protofilament polarities while the protofilament number is often two with a few exceptions (59, 68-76).

Although the functions mentioned in the last paragraph are the most known for each protein, some bacterial cytoskeletal proteins are involved in other functions. The cause of this phenomenon probably comes from the sequence diversities within each homolog (40, 41) presumably resulting from the diversity of bacterial species (77, 78) and small numbers of accessory proteins which constrict the evolution of eukaryotic cytoskeletal proteins (79). Such secondary functions are often reported in MreB. *Chlamydia trachomatis*, which lacks conventional division machinery including FtsZ, divides by budding using MreB filaments (80). *Myxococcus xanthus* MreB works as a rail for its motility machinery (81). *Helicobacter pylori* MreB is related to its urease activity and chromosome segregation (82). MreBs of a helical bacterium *Spiroplasma* are essential for its helical cell formation and motility in a liquid (83-85). As these phenomena have been found recently, these evolutional histories and molecular bases are actively researched in the field of bacterial cytoskeletons.

Evolution of *Spiroplasma* swimming

Motility is the ability of organisms to directionally move from an original point to another point using mechanical energy converted from chemical energy. This ability is not only found in macroscopic scales but also present in single cells (86, 87). As motility is one of the defining characteristics of organisms, it has attracted many researchers since the era of Leeuwenhoek (approximately 350 years ago) (25). The survival of organisms often relies on events involved in motility such as nutrient acquisition and escaping from

predators. Therefore, many organisms have acquired motility in their evolutionary paths (87). Swimming in a liquid is one of the most widely distributed motility modes in microbes when motility is divided based on its propulsive environment (86). As microbes in a liquid are under an environment with a low Reynolds number in which viscosity is more dominant than inertia because of their small mass sizes, microbes cannot be propelled by reciprocal motions like dolphin and flutter kicks. This phenomenon has been well known as the "Scallop theorem" (88). Instead, microbes have developed several types of motility machinery with time-irreversible motions to propel in a liquid (86, 87).

The most researched motility machinery in bacteria is the flagellum which propels a cell by screw-like motions (89). Flagella are composed of three parts: a basal body embedded in the cell membrane and the peptidoglycan layer, a helical filament with several micro-meter lengths, and a hook that works as the universal joint of the basal body and the filament (90-92). Stator subunits bound on the basal body rotate the flagellum with the energy supply of ion transports, and then the cell is propelled (92-95). Flagella are widely distributed for the bacterial kingdom (87) probably because of their high efficiency and throughput (96, 97) and their early appearance in which the origin is predicted to be traced back to the last-bacterial common ancestor (98). However, as flagella need a peptidoglycan layer for their rotation, wall-less bacteria cannot equip them (87, 99), which leads to develop other motility systems.

The phylum Tenericutes is a group of parasitic and commensal bacteria that evolved from the phylum Firmicutes including *Bacillus subtilis* (77, 78). The tenericutes species are characterized by their small genome sizes which result in lacking the synthesis pathways for some amino acids, nucleic acids, and phospholipids. Probably to retain the pathogenicity in the host cells, tenericutes have evolved to abandon the peptidoglycan

layer which is frequently targeted by host immune systems (87, 100-104). As a result, they have developed motility systems unrelated to flagellar motility (87, 105, 106). A genus in Tenericutes, *Spiroplasma*, is characterized by its helical cell body with several micro-meter lengths and sub-micrometer widths (Fig. 2A) (107, 108). *Spiroplasma* species swim in a liquid by propagating the helicity switching point (kink) from the cell tip along the cell body (Fig. 2B) (109, 110). This motility system is unique to *Spiroplasma* (87). This motility is driven by conformational changes of the intracellular ribbon structure composed of fibril, a *Spiroplasma*-specific cytoskeletal protein, and SMreBs (Fig. 2C) (111-115). Each *Spiroplasma* species has five classes of SMreBs (SMreB1–5), and these are classified into three functional groups based on sequence similarities: SMreB1 and 4, SMreB2 and 5, and SMreB3 (116). Previous genetic analysis revealed that the combinations of SMreB5 and either SMreB1 or SMreB4 are minimum sets for *Spiroplasma* swimming (84). Therefore, *Spiroplasma* swimming is currently recognized as the sole bacterial motility system driven by endogenous cytoskeletal proteins (87). Of note, *Spiroplasma* swimming is completely distinct from motility of another bacterium with a spiral cell shape spirochete which swims using intra-cellular flagella (86, 87, 90, 117). Moreover, *Spiroplasma* swimming is also distinct from eukaryotic motility systems using cytoskeletal proteins because this swimming motility does not depend on motor proteins walking on cytoskeletons using ATP such as myosin, kinesin, and dynein (1).
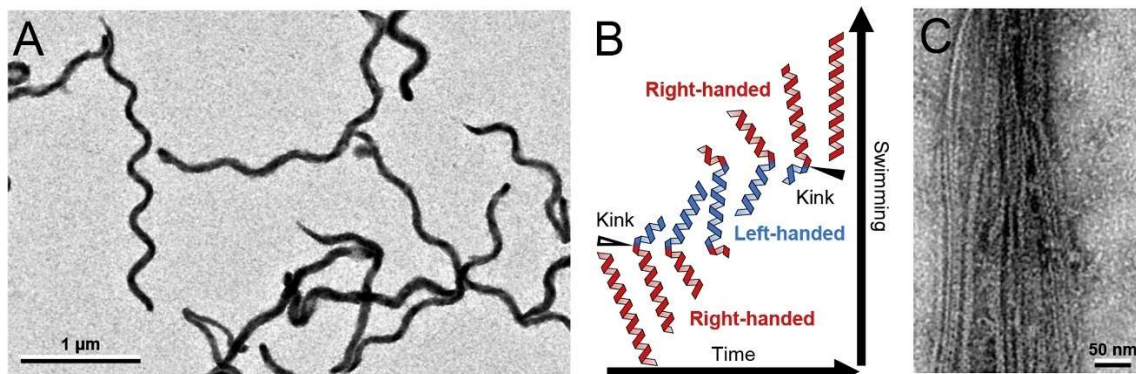
Figure 2. Morphology and swimming scheme of *Spiroplasma*. (**A**) Negative-staining EM image of *S. eriocheiris*. (**B**) Swimming scheme. *Spiroplasma* swim via the rotation of the cell body caused by kink propagation along the cell axis from front to back, which causes helicity shifts of right to left (open arrow head) and left to right (closed arrow head). (**C**) Negative-staining EM image of the isolated ribbon structure. Panels (**A**) and (**C**) were modified from a previous paper (111).

Upcoming questions of *Spiroplasma* swimming and MreB

The understanding of *Spiroplasma* swimming at the cell biology level has advanced to the point that a rheological model has been proposed based on optical-microscopic images (109, 110). However, evolution of *Spiroplasma* swimming was not unclear. The elongasome formation described in the first section is a housekeeping function of MreB, and its inhibition is lethal for walled bacteria (118). Although I introduced MreBs involved in other functions, these other than for *Spiroplasma* swimming are frequently dedicated together with shape determination by influencing peptidoglycan synthesis (80, 81, 119). It was unclear how SMreBs have escaped from the lethality of the loss of elongasome formation ability in the evolutionary path.

As well as the uncertainty of its evolution, the molecular mechanism of *Spiroplasma* swimming has not been revealed. MreBs of walled bacteria form non-helical double-stranded filaments in which two protofilaments interact antiparallelly (Fig. 1D) (75). Based on the antiparallel polarity, MreB filaments have been thought to be static in which polymerization and depolymerization are less active (120). In walled-bacterial cells, MreB filaments bind with the cell membrane via their membrane binding sequences at subdomain IA and move in a direction perpendicular to the cell major axis. However, these movements are driven by peptidoglycan synthesis by the elongasome complex rather than polymerization dynamics of MreB filaments (121-123). Therefore, SMreBs should acquire some characteristic properties to drive swimming motility, although their

details were poorly understood.

To understand of cytoskeletal proteins at the molecular level in depth, the coupling of each reaction step in ATPase and polymerization dynamics need to be elucidated. In eukaryotic actin, the reaction steps of ATPase and polymerization dynamics are linked as follows. First, ATP-bound monomeric actins (G-actin) polymerize into filamentous actins (F-actin) (124, 125). After the polymerization, F-actin hydrolyzes ATP to be a meta-stable state, ADP-P_i bound state. F-actin stochastically releases the phosphate to be ADP-bound state which is the most unstable state as a filament, and depolymerizes to be ADP-bound G-actins (8, 13, 126-128). Finally, the ADP-bound G-actin replaces the bound nucleotide to ATP and returns to the polymerization cycle. During the ATP hydrolysis step, a proton of the nucleophilic water is eliminated by the bridge water molecule interacting with D154 and H161 residues and the backbone oxygen of V159 to facilitate the reaction (the numbering of residues depends on skeletal actin) (126, 129, 130). The subtle conformational changes of the ATP moiety after the hydrolysis are sensed by the Q137 residue which forms a hydrogen bond with the nucleophilic water. This sensing mechanism transmits the subtle conformational change over the actin structure, allowing to show different biochemical properties of actin filaments at different nucleotide states (126). Although the coupling of each reaction step in ATPase and polymerization dynamics have been thoroughly clarified in actin, that of prokaryotic actins including MreB was unclear.

Answering these questions is necessary for the deep understanding of SMreBs which are a part of the unique motility machinery and probably have characteristic properties in cytoskeletal proteins. To do so, the following three studies should be performed: 1) phylogenetical analyses of SMreBs and walled-bacterial MreBs, 2) structural analyses of

SMreBs to reveal their conformational dynamics, and 3) biochemical analyses of SMreBs to clarify their assembly dynamics. Although some researches have been performed on these topics, those did not achieve clear conclusions to answer these questions (85, 131, 132). In this thesis, I report my research data on these topics in the following three chapters. In chapter 1, I analyzed the phylogeny and amino acid-level differences between SMreBs and walled-bacterial MreBs by *in silico* methods. In chapter 2, I studied for structures, ATPase activity, and polymerization activity of *S. eriocheiris* MreB3 and MreB5 (SpeMreB3 and SpeMreB5) and found their distinct properties and the coupling of these ATPase reaction steps and polymerization dynamics. In chapter 3, I analyzed the formation dynamics of higher order structures of SpeMreB5 in more detail for a deep understanding of its properties.

# Chapter 1: Evolution of SMreBs and characterization of an adjacent gene

ABSTRACT

Spiroplasma are wall-less bacteria which belong to the phylum Tenericutes that evolved from Firmicutes. *Spiroplasma* swim by a mechanism unrelated to widespread bacterial motility, such as flagellar motility, and caused by helicity switching with kinks traveling along the helical cell body. The swimming force is generated by five classes of bacterial actin homolog MreBs (SMreBs 1–5). A gene for a hypothetical protein (SPE_1229, 7th protein) has been found in a locus coding *mreB*s. Here, I analyzed sequences of SMreBs and the 7th protein to clarify their phylogeny and sequence features. The maximum likelihood method based on around 5,000 MreB sequences showed that the phylogenetic tree was divided into several radiations. SMreBs formed a clade adjacent to the radiation of MreBH, an MreB isoform of Firmicutes. Catalytic glutamic acid and threonine are substituted in SMreB3 from conventional ones. SMreBs 2 and 4 respectively conserved unique sets of residues in the regions of inter- and intra-protofilament interactions compared with those in *Bacillus* MreBs. A membrane-binding region was not identified in most SMreBs 1 and 4 unlike many walled-bacterial MreBs. SMreB5 had a significantly longer C-terminal region than the other MreBs, which possibly forms an interaction with other molecules. The 7th protein is predicted to be a lipoprotein, whose gene is encoded downstream of *mreB3* and conserved in a subgroup of *Spiroplasma*. These features may support the functions responsible for the unique mechanism of *Spiroplasma* swimming.

INTRODUCTION

MreB polymerizes into the filaments depending on a nucleotide binding for its cellular functions (Fig. 1D). The groove of the subunit (nucleotide-binding pocket) binds to a purine-nucleotide such as ATP and GTP (Fig. I-1A) (75). MD simulations suggest that the inter- and intra-protofilament interactions for the polymerization are comprised of four helices, two strands, and three loops (H3, H5, and H8 shown in Fig. I-1A for inter-protofilament interaction; H9, S12, S13 and loops between S6-H1, S9-S10, and S10-S11 shown in Fig. I-1A for intra-protofilament interaction) (133). Unlike the eukaryotic actin, MreB filaments bind to the cell membrane directly (122). Many MreBs have two consecutive hydrophobic residues for membrane binding in the hydrophobic loops in domain IA, and some MreBs of Gram-negative bacteria have an amphipathic helix at the N-terminus as an additional factor for membrane binding (Fig. I-1A) (122).

In various phyla of rod-shaped bacteria, MreB is well-conserved in the genomes and is responsible for cell shape maintenance by forming an elongasome complex (Fig. 1E) (44). Many bacterial species represented by *Escherichia coli* have a single copy of the *mreB* gene on their genome (44), whereas the genome of *B. subtilis* has three genes to code MreB isoforms (MreB, Mbl, and MreBH), all of which are employed in cell shape maintenance (118). As SMreBs may have a role distinct from those of other MreBs, sequence analyses among SMreBs and walled-bacterial MreBs are useful for clarifying the origin and mechanism of *Spiroplasma* swimming. Moreover, amino acid sequences specific for MreB functions have not yet been characterized for SMreBs.
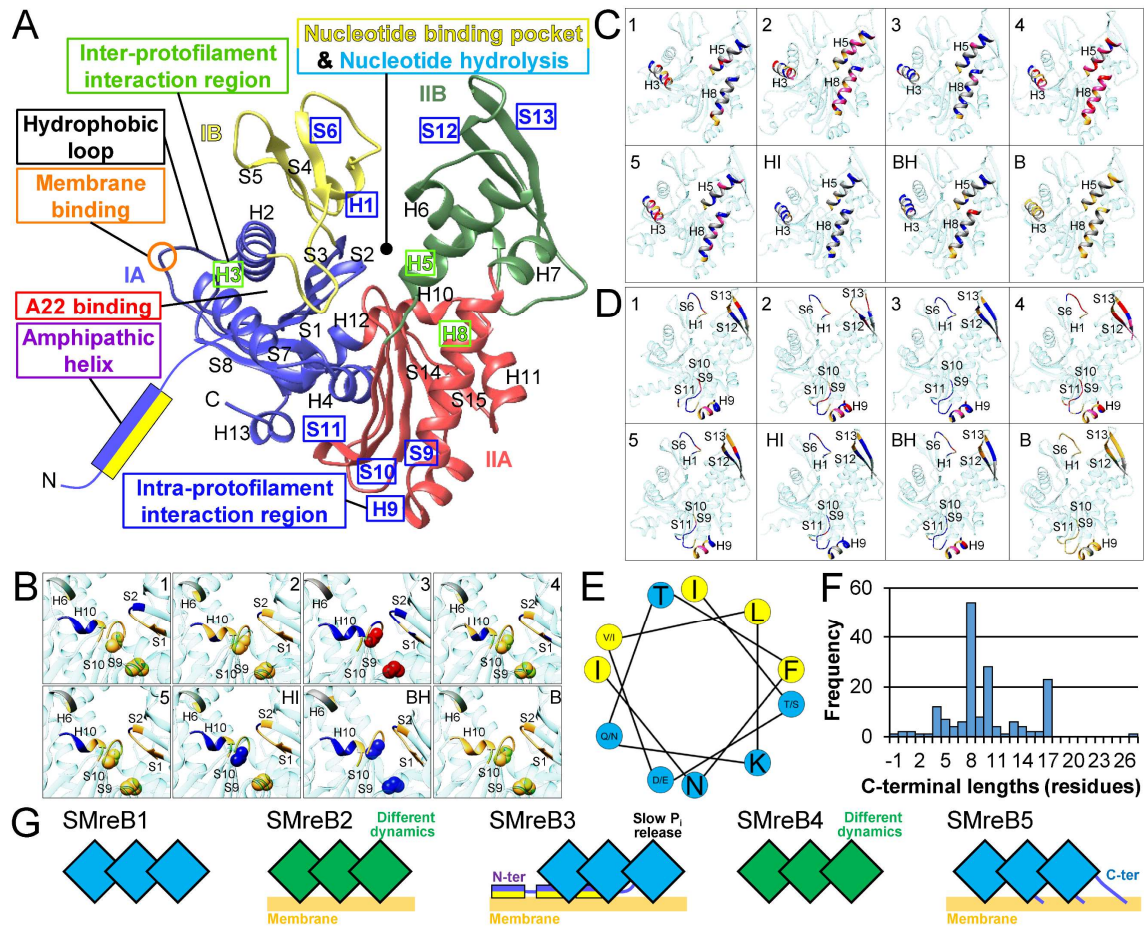
Figure I-1. Structural features of MreB proteins. (**A**) Captions of functional regions of MreB on a structural model of *B. subtilis* MreB predicted from the amino acid sequence (NP_390681.2). The structure is composed of 15 strands and 13 helices shown as S1–S15 and H1–H13, respectively. Individual domains are colored blue (IA), yellow (IB), red (IIA), and green (IIB). An N-terminal amphipathic helix carried by some Gram-negative bacterial MreBs is presented as a rectangle colored in purple. The nucleotide-binding pocket, catalytic region for nucleotide hydrolysis, A22 binding region, inter- and intra-protofilament interaction regions, hydrophobic loop, membrane binding residues in the hydrophobic loop, and N-terminal amphipathic helix are marked with a box common in style to those in Fig. I-3. (**B-D**) Focused amino acids are shown in 3D structures. The structures for SMreBs 1–5, HMreB, BMreBH, and BMreB are marked as 1–5, HI, BH, and B, respectively. The residues are colored red, pink, blue, or gold, based on the conservation levels compared to BMreBs (red: conserved residues whose corresponding ones in BMreB were conserved as different residues, pink: conserved residues whose corresponding ones in BMreB were not conserved, blue: not conserved residues whose corresponding ones in BMreB were conserved, gold: conserved residues whose corresponding ones in BMreB were conserved as the same residue). The numbers of helices and strands are indicated for colored parts. (**B**) Nucleotide-binding pocket. The backbone atoms of

Figure I-1 (continued) catalytic residues for nucleotide hydrolysis are indicated by spheres. (**C**) Inter-protofilament interaction region. (**D**) Intra-protofilament interaction region. (**E**) The helical wheel view of the third to thirteenth residues of SMreB3. Hydrophobic and hydrophilic residues are colored yellow and blue, respectively. (**F**) The length distribution of C-terminal excess regions of SMreBs compared to *B. subtilis* MreB sequence. (**G**) Summary of predicted characters of each SMreB presenting SMreB molecules (squares), slow P_i release (only statement), different polymerization dynamics (green color of squares), membrane binding (thick yellow line), N-terminal membrane binding region (purple rectangle), and C-terminal interacting region (blue line). Membrane binding and N-terminal membrane binding region are presented based on Citri group SMreBs, and the others are presented based on both Apis and Citri groups.

In a locus coding *mreB*s, a hypothetical gene *SPE_1229* was found to be encoded. Although SPE_1229 was not essential in swimming reconstruction experiments (83, 84), its homologs are found in many *Spiroplasma* species with a corresponding position (85). However, SPE_1229 is poorly characterized.

In this study, I analyzed the sequences of SMreBs and SPE_1229. Phylogenetic analyses suggested that SMreBs evolved from MreBH in Firmicutes. Sequence comparisons of SMreBs and *Bacillus* MreBs clarified their sequence features for ATP hydrolysis, interactions for filament formation, and membrane binding. SPE_1229 was predicted as a lipoprotein. In the following sections, I call SPE_1229 and its gene by tentative names "7th protein" and "*7th gene*", respectively, because the gene position is adjacent to one of the "six" cytoskeletal proteins for *Spiroplasma* swimming.

RESULTS AND DISCUSSION

Sequence acquisitions of SMreBs and 7th protein–

First, I performed BLAST searches to obtain amino acid sequences of MreB family proteins and 7th protein. For MreB family proteins, 5,002 sequences were obtained including all 170 non-redundant sequences of SMreBs with those of three new species (*S.*

sp. TU-14, *S.* sp. ChiS, and *S.* endosymbiont of *Megaselia nigra*) (134-136). I also

obtained 14 sequences of the 7th protein (Table I-1). Sequences from species other than

Spiroplasma were not found, suggesting that the 7th protein is specific for *Spiroplasma*.

Table I-1. Accession IDs and the source species of the 7th proteins obtained by the BLAST search and their predicted lengths of signal sequences.

Accession ID	species	Predicted length of signal sequence
WP_047791952.1	*S. eriocheiris*	18
WP_025317915.1	*S. mirum, S. atrichopogonis*	18
WP_070407230.1	*S.* sp. TU-14, *S.* NBRC 100390	20
WP_127092450.1	*S. poulsonii*	20
WP_105298698.1	*S.* sp. ChiS	20
WP_253301537.1	*S.* endosymbiont of *Phyllotreta cruciferae*	20
WP_004028010.1	*S. melliferum*	20
WP_071938028.1	*S. citri*	20
WP_114565546.1	*S. phoeniceum*	23
WP_053390368.1	*S. kunkelii*	20
WP_126820764.1	*S.* endosymbiont of *Megaselia nigra*	23
MBH8623726.1	*S.* sp. Moj	23
WP_016339400.1	*S. chrysopicola*	20
WP_016341226.1	*S. syrphidicola*	20

Evolutional relationships between SMreBs and walled-bacterial MreBs

I first analyzed the phylogenetic relationships among SMreBs and other MreBs.

Based on the sequences taken by the BLAST search, I constructed a maximum likelihood

phylogenetic tree (Fig. I-2A). I adopted this phylogenetic tree because substantial

differences were not found among the topologies of a maximum likelihood phylogeny

using 4,000 sequences, the Neighbor-Joining phylogeny using 5,002 sequences, and the

phylogeny shown in Fig. I-2A. The largest radiation of the phylogenetic tree consisted of

MreB family proteins of conventional bacteria, which were further divided into Gram-

negative and positive bacteria. Previous studies of MreB family proteins have primarily

focused on proteins in these radiations (44). In my phylogenetic tree, an MreB radiation

of CPR (Patescibacteria in another name) (77, 78, 137, 138), which is composed of

Parcubacteria and Microgenomates superphyla, was formed next to the radiation of conventional MreBs. The CPR MreBs were split into two clades. Three candidate species of Parcubacteria in candidate phyla Yanofskybacteria, Taylorbacteria, and Zambryskibacteria, and a candidate species of Microgenomates in candidate phylum Woesebacteria had MreBs of both clades, suggesting the existence of two types of MreBs possessing different roles in CPR.

Firmicutes bacteria have more than one copy of a gene coding MreB isoforms on the genomes (118), and these isoforms formed three independent clades other than the radiation of conventional MreBs. One was mostly composed of class Bacilli MreB family proteins related to *Bacillus* Mbl. Another clade between clades of *Bacillus* Mbl and CPR MreB was primarily composed of proteins in class Clostridia and was distantly related to *Bacillus* MreB isoforms, suggesting the existence of a new group of MreB isoforms. The clade including BMreBH had a root distinct from other clades. SMreBs formed a radiation near the BMreBH clade. A clade of MreBs from tenericutes bacteria *Haloplasma* and *Candidatus* Izimaplasma (*Xianfuyuplasma* in a newly suggested nomenclature (139)) (HMreB) was identified between clades of SMreB and BMreBH (Fig. I-2A). *Haloplasma contractile* is known to have characteristic motility via tentacle-like structures extending from a coccoidal body (140). HMreB may be involved in this characteristic motility of *Haloplasma* (132, 140), while previously cultured Izimaplasma was non-motile (139).
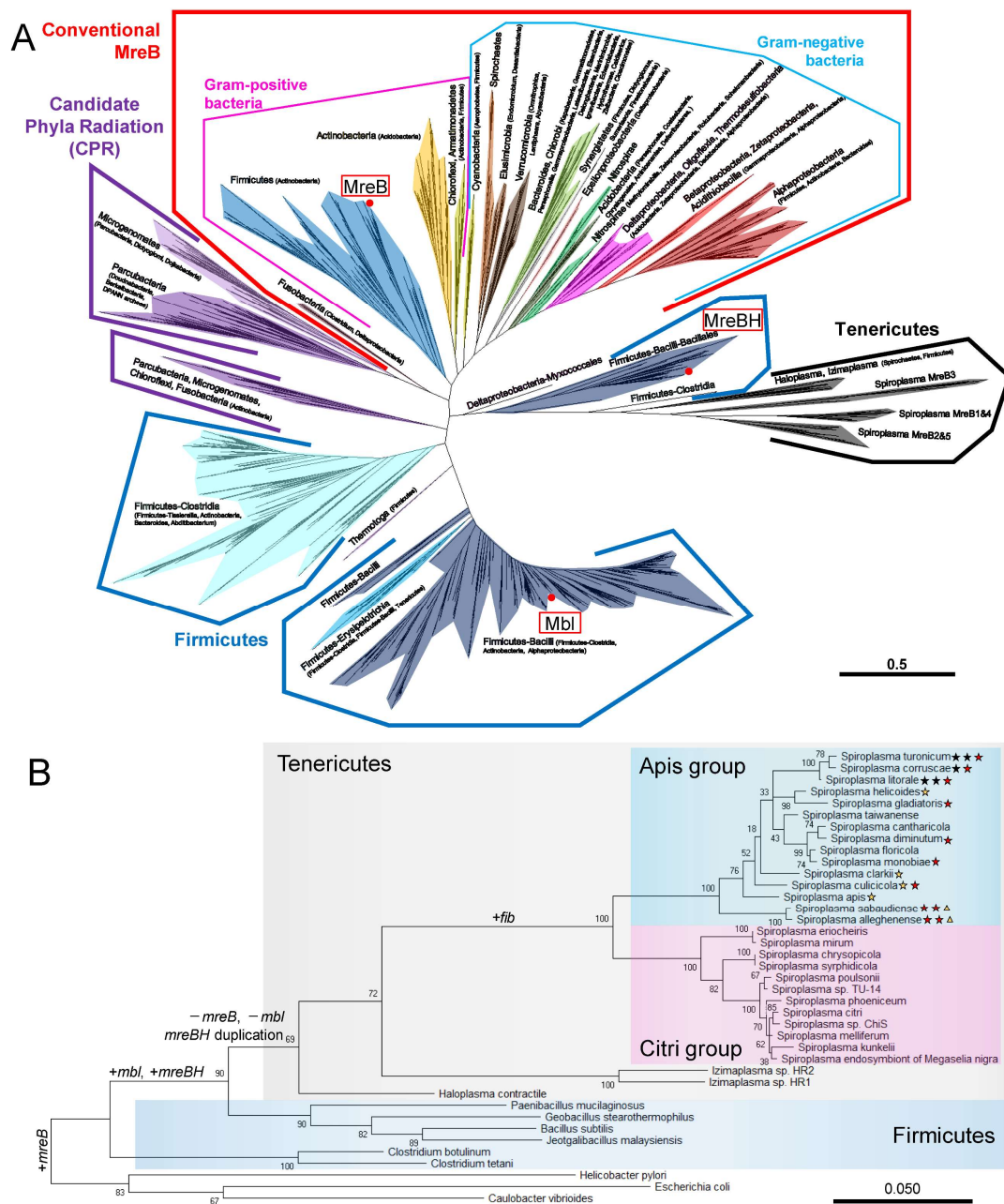
Figure I-2. Phylogenies of SMreBs and *Spiroplasma* species. (**A**) Unrooted maximum likelihood phylogenic tree for 5,002 amino acid sequences of MreB family proteins. The radiation of conventional MreBs, which are conserved for various walled bacteria, is indicated by a red polygon. The other radiations composed of Firmicutes MreB isoforms, CPR MreBs, and Tenericutes MreBs are indicated by blue, purple, and black polygons, respectively. Each clade is colored according to the major phyla (or classes). Major and minor taxa in each clade are indicated without and with parentheses, respectively. The branches of MreB isoforms in *B. subtilis* are marked by red circles. The scale bar is in units of the number of amino acid substitutions per site. (**B**) Maximum likelihood phylogeny for 16S rRNA of the organisms that are related to the evolution of *Spiroplasma*.

- 23 -

Figure I-2 (continued) Sequences for 16S rRNA of proteobacteria (*E. coli*, *Caulobacter vibrioides*, and *H. pylori*) were used as the outgroup. Bootstrap support values estimated from 100 alignment samples are indicated on each node. Stars and triangles marked for each species indicate one duplication and deletion, respectively for genes of SMreBs colored differently as yellow: SMreB1, green: SMreB2, black: SMreB4, and red: SMreB5. The scale bar is in units of the number of nucleotide substitutions per site.

Development of *Spiroplasma* swimming

Based on the phylogeny result, I assessed the evolutional background prior to *Spiroplasma* acquiring swimming motility based on a phylogenetic tree of 16S rRNA (Fig. I-2B). A Firmicutes species ancestral for Tenericutes probably possessed MreB, Mbl, and MreBH because the Firmicutes species closest to Tenericutes had these three MreB isoforms (77, 141, 142). The ancestral bacterium then likely lost MreB and Mbl and duplicated MreBH before *Haloplasma* and other Tenericutes bacteria separated. Among the three MreB isoforms, MreB and Mbl are essential under the normal growth condition (143, 144). In contrast, MreBH is not required under the normal growth condition (145), suggesting that MreBH is prone to accumulate mutations. Therefore, SMreBs and HMreBs acquisitions from MreBH are the most plausible evolutional story because the evolutionary pressure is possibly lower than the evolutions from MreB and Mbl. After the duplication of MreBH, *Haloplasma* and Izimaplasma likely acquired HMreBs (Fig. I-2B). A previous study suggested that *Haloplasma* and *Spiroplasma* acquired their MreBs by independent gene duplications (132). However, HMreB was located closer to SMreB and MreBH than to the other clades in my phylogenetic tree (Fig. I-2B). Accordingly, *Spiroplasma* likely acquired SMreBs through the duplication of MreBH (Fig. I-2B). The other component of the intra-cellular ribbon structure, fibril was likely acquired after *Spiroplasma* and Izimaplasma separated, because it is specific for *Spiroplasma* (111-113,

132).

The *Spiroplasma* genus can be divided into two subgroups: Apis and Citri-Chrysopicola-Mirum (Citri). In terms of the *Spiroplasma* genomes, duplications of SMreBs 1, 4, or 5 and deletions of SMreB1 were identified in almost all species of the Apis group unlike the Citri group (Fig. I-2B) (132). Previous studies on *Spiroplasma* swimming have mostly focused on four Citri species (*S. melliferum, S. citri, S. eriocheiris*, and *S. poulsonii*), all which swim via similar kink propagations (83-85, 109-114, 116, 146-148). The duplication and deletion of SMreBs in the Apis group may suggest their diverse swimming formats.

Sequence comparisons among SMreBs and BMreBs

I compared the amino acid sequences of SMreB, HMreB, BMreB, and BMreBH to characterize SMreBs (Fig. I-3). First, the conserved residues of SMreBs 1–5, HMreB, and BMreBH sequences were compared with those of 48 sequences of BMreBs. Each SMreB type showed specific conserved sequences different from those of BMreBs. SMreB 1–5 conserved 128, 187, 46, 210, and 121 residues in approximately 330 full-length amino acid sequences, respectively. Of these residues, 50, 102, 21, 122, and 53 residues were specific for each SMreB, respectively, and were not conserved in BMreBs (Fig. I-3). Residues that are specifically conserved among SMreBs may be essential for intrinsic functions of SMreBs.
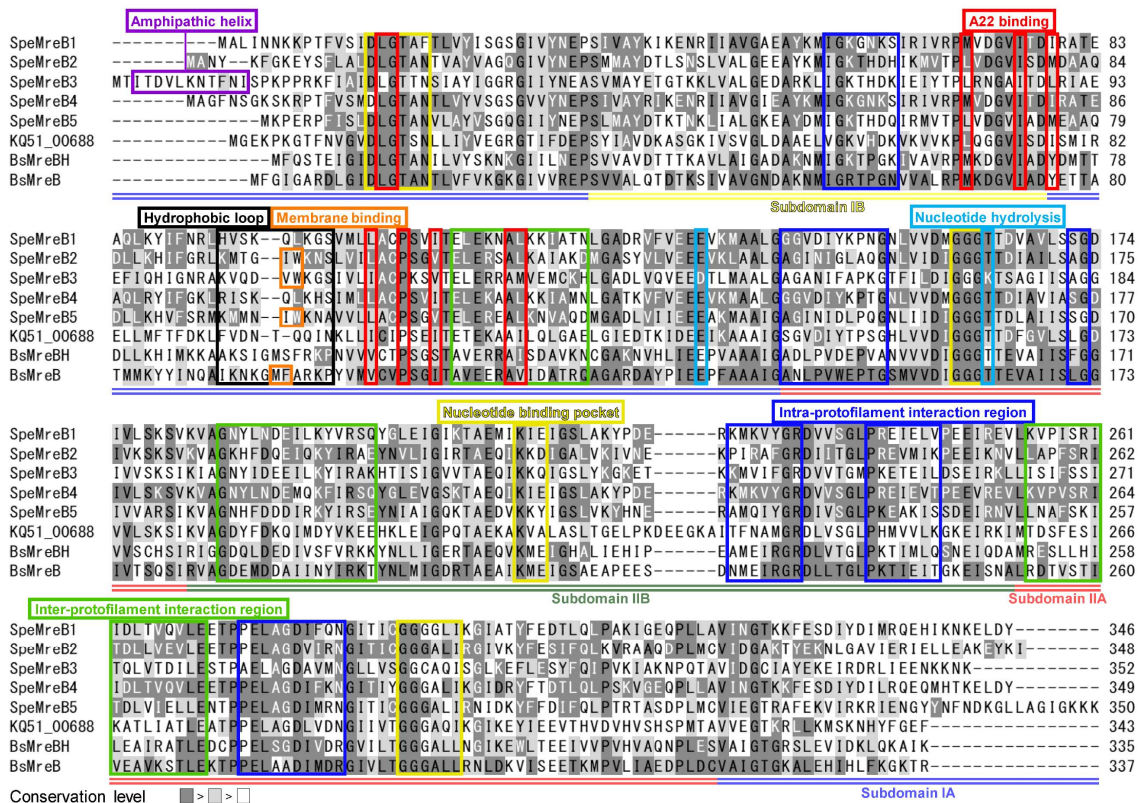
Figure I-3. Multiple alignment of SMreBs 1–5, HMreB, BMreB, and BMreBH using SpeMreBs 1–5, KQ51_00688 in Izimaplasma sp. HR1, *B. subtilis* MreBH, and *B. subtilis* MreB. The conservation levels for residues calculated from multiple alignments of each MreB are indicated by the gradient of gray markers (residues calculated as identical and strongly conserved based on the Gonnet PAM 250 matrix are marked by deep and light gray, respectively. The other residues are not colored). In SMreBs 1–5, HMreB, and BMreBH, the conserved residues, whose corresponding residues in BMreB were conserved as a different one or were not conserved, are indicated by white characters. Subdomains IA, IB, IIA, and IIB are identified by double underlines of coordinated colors with Fig. I-1A. Sequences important for the specific function of MreB are indicated by rectangles with different colors.

Characterization of SMreBs based on amino acid sequences

Next, to investigate the SMreB sequences corresponding to the sequences conserved in walled bacteria (75, 122, 133, 149, 150), I predicted the ancestral sequences and 3D structures for SMreBs 1–5, HMreB, BMreBH, and BMreB (Fig. I-1B-D). First, I focused on the 19 residues that construct the nucleotide-binding pocket (Fig. I-1A and B) (150).

In SMreB sequences, most of the 11 residues conserved in BMreBH were also conserved (Fig. I-1B, Fig. I-3 yellow boxes). I also focused on the catalytic residues for nucleotide hydrolysis (75). While a glutamate and threonine were conserved in almost all MreBs, interestingly, in SMreB3, these residues were replaced to an aspartate and lysine, respectively (Fig. I-1B, Fig. I-3 cyan boxes). As mutations on the catalytic residues reduce P_i release rates of eukaryotic actin (151), SMreB3 may also have slower P_i release rates than other SMreBs (Fig. I-1G). It has been reported that an antibiotic A22 inhibits MreB polymerization by interacting with the nucleotide in the MreB molecule (149). SMreBs also conserved the target residues of A22 (Fig. I-3 red boxes) (149). This result is consistent with a previous study, in which A22 was effective for *Spiroplasma* cells (146).

Next, I focused on 87 residues involved in the inter- and intra-protofilament interactions (H3, H5, H8, H9, S12, and S13 and loops between S6-H1, S9-S10, and S10-S11 in Fig. I-1A, C, and D) (133). In these regions, 31, 50, 14, 69, and 32 residues were conserved in SMreBs 1–5, respectively (Fig. I-1C and D, Fig. I-3 green and blue boxes). In these residues, 15, 26, 6, 40, and 16 were not conserved in BMreBs, respectively (red and pink residues in Fig. I-1C and D, white characters in light green and blue boxes in Fig. I-3). As these regions in a walled-bacterial MreB move toward an adjacent MreB molecule to interact with each other (133), these amino acid substitutions of SMreBs, especially SMreBs 2 and 4, may affect the flexibility and interaction strength, allowing them to show polymerization characters different to those of walled-bacterial MreBs (Fig. I-1G).

I also characterized regions required for membrane binding. Two consecutive hydrophobic residues are conserved in many walled-bacterial MreBs (Fig. I-1A) (122). However, SMreBs 1 and 4 of the Citri group did not have hydrophobic residues at the

corresponding position (Fig. I-3 orange boxes) (75, 122). Moreover, the consecutive hydrophobic residues cannot be found in 46 out of 88 sequences of the Apis group SMreBs 1, 3, 4, and 5. These SMreBs may not directly interact with the membrane. I next focused on the N-terminal amphipathic helix found in some MreBs of Gram-negative bacteria (Fig. I-1A). All N-terminal regions of the Citri group SMreB3, except for *S. melliferum* strain AS576 (QCO24517.1), were predicted to form amphipathic helices (Fig. I-1E, Fig. I-3 purple box). This suggests that Citri group SMreB3 proteins also have affinity to the membrane through the helix (Fig. I-1G).

The lengths of C-terminal sequences varied among 133 SMreBs, and over 79% of SMreBs were eight residues longer than that of BMreB (Fig. I-1F, Table I-2). SMreB5 had the longest C-terminal sequence of all SMreBs (Table I-2). Such a terminal extension is a feature reminiscent of a bacterial tubulin homolog, FtsZ, featured with a long unstructured region. This is the interaction region for several proteins, including FtsA, ZipA, and ZapD involved in the divisome formation (152). The extension of the SMreB C-termini may play a role in an interaction with other molecules. A recent study revealed the interaction with anionic lipid molecules of SciMreB5 via its C-terminus (131). My finding suggests that the membrane binding found in SciMreB5 is conserved in SMreB5 (Fig. I-1G).

Table I-2. Lengths and amino acid identities of SMreB terminal excess regions compared to the *B. subtilis* MreB sequence.

|	SMreB1	SMreB2	SMreB3	SMreB4	SMreB5	HMreB
N-ter. Apis (a.a. / Ident. (%))	−1~2 / 0	2 / 100	2~5 / 0	0~6 / 0	−2~6 / 0	−2~7 / 0
N-ter. Citri (a.a. / Ident. (%))	3 / 66.7	4 / 100	13(7) / 57.1	4~6 / 75.0	−1~0 / 0	
C-ter. Apis (a.a. / Ident. (%))	1~13 / 0	9~10 / 33.3	−1~12 / 0	7~10 / 0	10~17 / 10.0	0~3 / 0
C-ter. Citri (a.a. / Ident. (%))	8 / 50.0	9~10 / 44.4	3~4 / 66.7	8 / 75.0	16~27 / 37.5	

Characterization of 7th protein

I first searched for the distribution of 7th protein (Fig. I-4A). The 7th proteins are conserved in the Citri group but not in the Apis group. Next, I examined the order of genes coding for the 7th protein and the cytoskeletal proteins related to *Spiroplasma* swimming, that is, fibrils and the five classes of SMreBs. The *7th gene* is found at the same location in a locus that includes *mreB2*, *mreB3*, *mreB4*, and *mreB5*. The gene order from *mreB2* to *mreB5* was classified into four patterns (Fig. I-4B). In the genomes of 8 out of 10 species in the same clade as *S. citri* (species labeled as Citri in Fig. I-4B), *mreB2*, *mreB3*, *7th gene*, *mreB4*, and *mreB5* were tandemly encoded in the order shown (Fig. I-4B-3). The *S. melliferum* genome encoded another hypothetical gene immediately before *mreB3* (Fig. I-4B-4). In the genomes of three species (*S. eriocheiris*, *S. mirum*, and *S. atrichopogonis*), *alkA* (at the minus strand), *adaA*, and *adaB*, all of which are responsible for demethylations of DNA (153), are encoded between *mreB2* and *mreB3* (Fig. I-4B-1). *S. chrysopicola* and *S. syrphidicola* encoded a gene for NADH-flavin deaminase and *adaA* between *7th gene* and *mreB4* (Fig. I-4B-2). Although there is diversity in gene orders at the loci, the *7th gene* is still encoded downstream of *mreB3* (Fig. I-4B).

To characterize the 7th protein, its amino acid sequence was analyzed using Phobius, a prediction tool for membrane proteins (154). All the 7th protein sequences were predicted to possess signal sequences for extracellular secretion on the N-terminal 18–23 residues (Fig. I-4C, Table I-1). At the 21st to 25th position, around the end region of the signal sequence, the [V/L]-[V/T]-S-C-[S/L] motif was conserved in 13 out of 14 sequences of the 7th protein (Fig. I-4C red box). This motif matches the consensus sequence of the lipobox ([L/V/I]-[A/S/T/V/I]-[G/A/S]-C-X) conserved at the end of a signal sequence in bacterial prolipoproteins (155). The structure of the 7th protein

predicted by AlphaFold2 (156) excluding the signal sequence showed a globular fold enriched with α-helices (Fig. I-4D). The globular fold of the 7th protein is well conserved among phylogenetically distant species (*S. melliferum*, *S. eriocheiris*, and *S. chrysopicola*) (Fig. I-4A and E). Altogether, I suggest that the 7th protein is a lipoprotein that takes the globular fold on the extracellular side of the membrane. To predict the lipid modification of the 7th protein, I examined the conservation of genes encoding three key enzymes responsible for the maturation of bacterial lipoproteins: Lgt, which adds a diacylglycerol group on the cysteine residue in the lipobox of a prolipoprotein; Lsp, which cleaves off the signal sequence of the prolipoprotein; and Lnt, acylating the amino group of the N-terminus of the prolipoprotein to mature up to the lipoprotein (155, 157). Lgt and Lsp were conserved in *Spiroplasma*, whereas Lnt was absent (Fig. I-4A). This gene conservation pattern is the same as that of other Mollicutes species (157, 158). These results suggest that the 7th protein undergoes the addition of the diacylglycerol group and the cleavage of the signal sequence in the same way as in other bacteria. Although some lipoproteins in Mollicutes species are not *N*-acylated consistent with the absence of Lnt (159, 160), the *N*-acylation of many lipoproteins is reported in Mollicutes species including *S. melliferum* (161-163). Further studies will be needed to determine the *N*-acylation state of the 7th protein.

In this study, I predicted that the 7th protein is a lipoprotein whose gene is encoded downstream of *mreB3*. Bacterial genes encoded closely in the same locus are often functionally related (106). My analyses suggest that the 7th protein localizes to the extracellular side, whereas MreBs localize to the cells (111, 113, 114, 146). These suggest that the 7th protein and MreBs do not interact with each other for their functions. However, the position of the *7th gene* downstream of *mreB3* was conserved in every Citri group

species, suggesting that the 7th protein may take functions indirectly aided by *Spiroplasma* swimming. Motility of pathogenic microbes like *Spiroplasma* is involved in their pathogenic steps such as the invasion to and the spreading in the host cells (87). One of the possible functions of the 7th protein is then involved in their parasitic steps, such as host cell adhesion, invasion, and colonization, which are general roles for lipoproteins in parasitic bacteria (155, 164). It is true that a previous study did not determine the function of the 7th proteins (84). However, we believe that the 7th protein is involved in the life cycle of Citri group *Spiroplasma* because Mollicutes species suffer from genome reduction pressure due to their pathogenic lifestyle, so redundant genes are removed from the genomes (165).
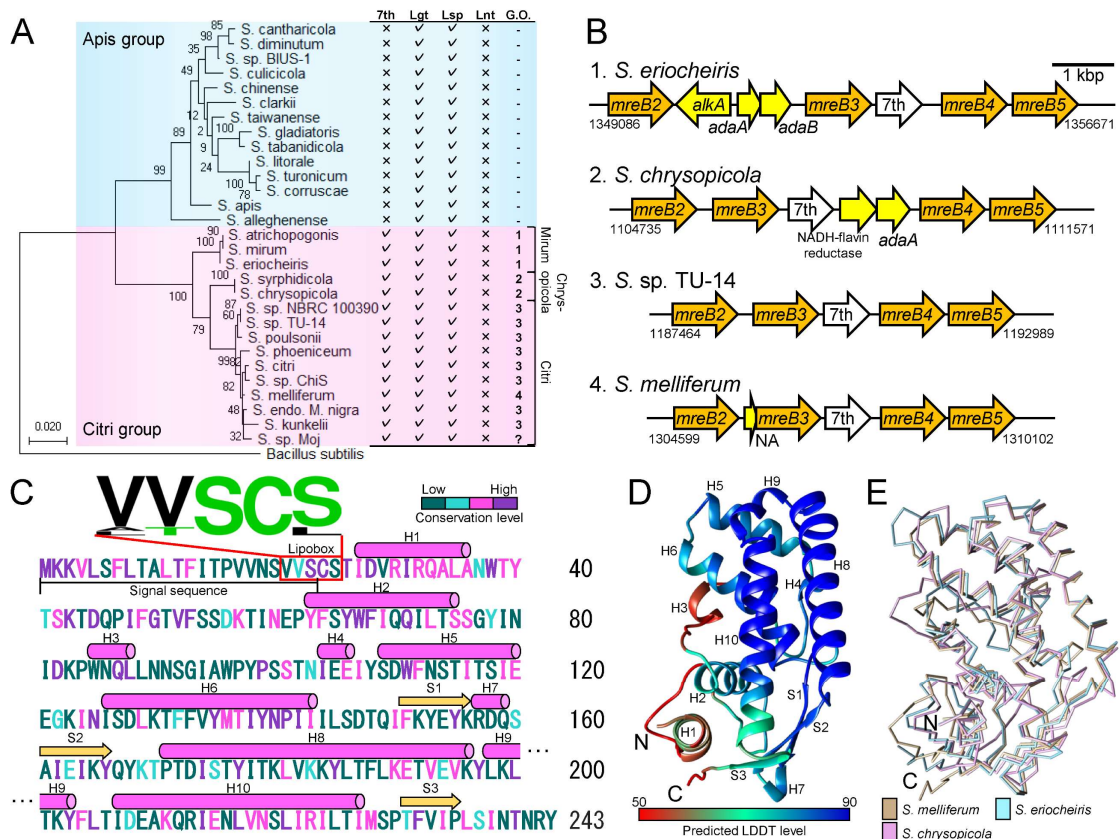
Figure I-4. Characterization of the 7th protein. (**A**) (Left) Maximum likelihood phylogeny of 16S rRNA of *Spiroplasma*. *B. subtilis* 16S rRNA sequence is used as the outgroup. Species belonging to Apis and Citri groups are highlighted using cyan and magenta boxes, respectively.

Figure I-4 (continued) Bootstrap support values were estimated from 500 alignment samples and indicated on each node. The scale bar is in units of the nucleotide substitution numbers per site. (Right) List summarizing the presence of genes for the 7th protein, Lgt, Lsp, and Lnt. The check and cross symbols indicate whether the corresponding gene is present or absent, respectively, on the genome. Column G.O. indicates the patterns of the gene orders from *mreB2* to *mreB5* shown in panel B. Gene organization pattern of *S.* sp. Moj could not be determined owing to the insufficient length of the reported contig sequence including the *7th gene*, denoted using "?" in the G.O. column. Three classifications in Citri group (Mirum, Chrysopicola, and Citri) are indicated on the right of the list. (**B**) Four patterns of gene orders from *mreB2* to *mreB5* found in Citri group species. The nucleotide numbers of the *mreB2* initiation and *mreB5* termination points on the genomes are indicated below the corresponding sites. (**C**) Amino acid sequence of the 7th protein of *S. melliferum*. Each amino acid is colored based on the four conservation levels (purple for identical, magenta for strongly similar, cyan for weakly similar, and green for diverse) estimated by the multiple alignment of 14 amino acid sequences of the 7th protein. The signal sequence region is indicated using a solid line. The lipobox region is indicated using a red box with its WebLogo on the sequence. The regions for the α-helix and β-strand predicted by AlphaFold2 are indicated using a magenta cylinder and yellow arrow, respectively. (**D**) Ribbon representation of *S. melliferum* 7th protein structure predicted by AlphaFold2. The first 24 residues at the N-terminus including the signal sequence and lipobox are excluded from the model. Each residue is colored by the predicted pre-residue confidence score (LDDT). (**E**) Structural comparison among the 7th proteins of *S. melliferum* (beige), *S. eriocheiris* (cyan), and *S. chrysopicola* (magenta).

CONCLUSIONS

In this chapter, I suggested that the five classes of SMreBs evolved from MreBH (Fig. I-2A) and clarified that the classes can be characterized by ATP hydrolysis, interactions for filament formation, and membrane binding. Based on these results, I suggest the functions for individual SMreBs (Fig. I-1G). I also analyzed for the 7th protein and suggested that it is a lipoprotein (Fig. I-4). The presence of the 7th protein suggests distinct survival strategies in the two *Spiroplasma* subgroups.

MATERIALS AND METHODS

Sequence acquisitions

Protein BLAST searches on non-redundant protein sequences was performed for SMreBs and the 7th protein. For SMreBs, 5,000 amino acid sequences were obtained in ascending order of E-value (the maximum value was calculated as 2×10^{-63} for MAV90490.1) with the template of SpeMreB3 (WP_047791951.1) on July 14, 2019. Sequences of *B. subtilis* MreB isoforms annotated to MreB (AQR87043.1) and MreBH (BAA07047.1) were added to the 5,000 sequences as representative sequences. Sequences of the 7th protein were obtained as the reference for *S. eriocheiris* (WP_047791952.1) with the E-value threshold of 0.05, on August 22, 2022. Sequences that were duplicated and misannotated were excluded from the sequence set for analysis (WP_004028916.1, CAK98229.1, and WP_252157057.1). Thus, the sequence set contains 14 amino acid sequences of the 7th protein (Table I-1). The sequence of the 7th protein from *S.* endosymbiont of *Phyllotreta cruciferae*, whose 16S rRNA sequence was not reported, was excluded from the phylogenetic and gene organization analyses.

Phylogenetic analyses

The sequence alignments and construction of phylogenetic trees were performed via the MUSCLE program, and maximum likelihood and Neighbor-joining methods, respectively, using MEGA-X ver. 10.1 (166). For the ancestor estimation, maximum likelihood phylogenetic trees by each MreB group were constructed with a *B. subtilis* MreB (an *E. coli* MreB for the estimation of BMreB) as an outgroup, and the ancestral sequences were estimated by the ancestor estimation program of MEGA-X ver. 10.1 (166).

Structure prediction and sequence analyses

All monomeric MreB structures in this study were predicted using Rosetta comparative modeling by templating a structure of CcMreB (PDB ID: 4CZJ), using Robetta software (75, 167). The structures of the 7th proteins were predicted from their full-length sequences by the CoLab version of AlphaFold2 (156), and the structural visualizations and the removal of the signal sequence were performed on UCSF Chimera ver. 1.13.1 (168). Sequence comparisons among amino acid sequences were performed by Clustal Omega (169, 170). The conservation of the 7th protein lipobox was further evaluated by WebLogo (171). Duplicated SMreBs 1, 4, and 5 in the Apis group species were incorporated into the analyses. Seven of the 19 amino acid sequences contained in SMreB3 of the Apis group had no annotation. Since these proteins were coded in a position suggesting SMreB3 as an ortholog on the genome, they were included in the analyses. SMreB3 of the *S. melliferum* strain CH-1 (AHA83319.1) was excluded from the analyses because it was approximately 40% shorter than the other SMreB3 sequences. Two sequences, SMreB4 of *S. eriocheiris* strain CCTCC_M_207170 (AHF58342.1) and a protein from *S. culicicola*, which is unannotated but can be classified to SMreB3 (WP_025363622.1), were not used for the analyses because the initiation codons were miss-assigned. The predictions of secondary structures and amphipathic helices were performed using PSIPRED 4.0 and AmphipaSeeK software, respectively (172, 173). Sequence identity and similarity were calculated as the ratio of amino acids with identity and strong similarity defined by the Gonnet PAM 250 matrix over the total amino acid number excluding gap regions. Signal peptide regions of the 7th proteins were predicted using Phobius (154).

Chapter 2: ATP-dependent polymerization of SpeMreB3 and SpeMreB5

ABSTRACT

MreB is a bacterial protein belonging to the actin superfamily. This protein polymerizes into an antiparallel double-stranded filament that determines cell shape by maintaining cell wall synthesis. *Spiroplasma eriocheiris*, a helical wall-less bacterium, has five MreB homologs (SpeMreB1–5) that likely contribute to swimming motility. Here, I investigated the structure, ATPase activity, and polymerization dynamics of SpeMreB3 and SpeMreB5. Upon nucleotide binding, SpeMreB3 polymerized into a double-stranded filament with possible antiparallel polarity, while SpeMreB5 formed sheets which contained the antiparallel filament. SpeMreB3 showed slow P_i release owing to the lack of an amino acid motif conserved in the catalytic center of MreB family proteins. My SpeMreB3 crystal structures and P_i release analyses of SpeMreB3 and SpeMreB5 variants showed that the amino acid motif most likely plays a role in eliminating a nucleophilic water proton during ATP hydrolysis. Sedimentation assays suggest that SpeMreB3 has a lower polymerization activity than SpeMreB5, though their polymerization dynamics are qualitatively similar to those of other actin superfamily proteins, in which pre-ATP hydrolysis and post-P_i release states are unfavourable for them to remain as filaments.

INTRODUCTION

In chapter 1, I characterized each SMreB by *in silico* analyses and suggested their distinct features (Fig. I-1G). Previous studies on SMreBs have been focusing on their cellular behaviors (83, 84, 116). To understand the swimming mechanism, it is necessary

to clarify the molecular features of SMreBs. Previous studies revealed the structure, polymerization, and membrane and fibril bindings of SciMreB5 (85, 131), although these studies did not fully reveal its polymerization dynamics and ATP hydrolysis mechanism, which are important to understand the molecular mechanism of *Spiroplasma* swimming. Here, I studied MreB3 and MreB5 in *S. eriocheiris* (SpeMreB3 and SpeMreB5, respectively), a model for studying *Spiroplasma* swimming (111, 146, 147, 174, 175). Upon nucleotide binding, SpeMreB3 polymerizes into a double-stranded filament with possible antiparallel polarity, while SpeMreB5 forms an asymmetric sheet, which contains the antiparallel filament. The SpeMreB3 crystal structures of SpeMreB3 and P_i release measurements suggest that SpeMreB3 lacks an amino acid motif for ATP hydrolysis conserved in other MreB family proteins, resulting in low ATPase activity. These differences between SpeMreB3 and SpeMreB5 are likely basis of their distinct cellular functions. I also suggest the two MreB features: 1) ATP hydrolysis mechanism in MreB family proteins, including a possible proton transfer pathway and 2) the polymerization dynamics of SpeMreB3 and SpeMreB5, which are qualitatively similar to other actin superfamily proteins (8, 12, 13, 127, 128).

RESULTS

Nucleotide binding induces SpeMreB3 and SpeMreB5 polymerization into double-stranded filaments and asymmetric sheets, respectively

I individually expressed all five SpeMreBs in *Escherichia coli* as fusions with a 6×His-tag. SpeMreB1, SpeMreB2, and SpeMreB4 were not obtained from the soluble fraction. In contrast, SpeMreB3 and SpeMreB5 were soluble and were successfully purified as monomers (Fig. II-1), enabling me to assay the polymerization reactions.
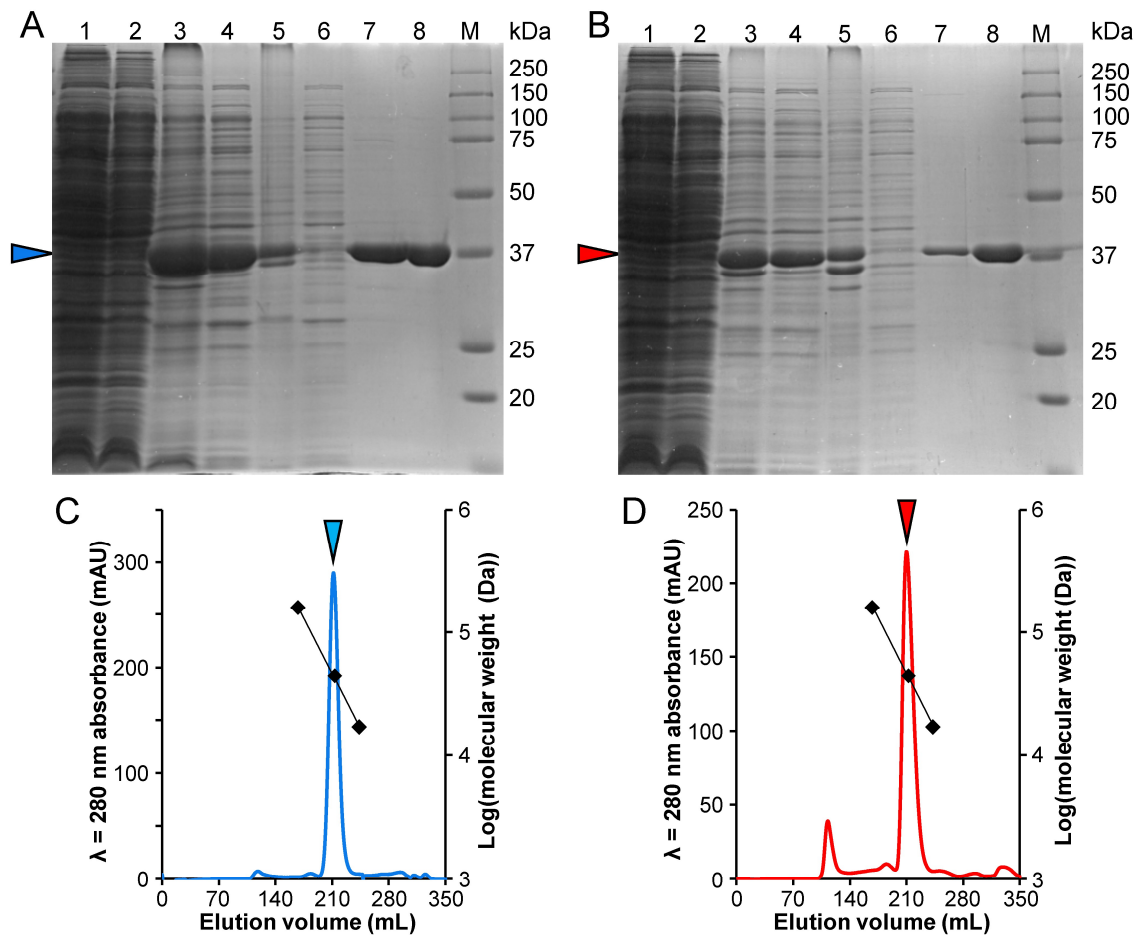
Figure II-1. Purification and gel filtration profiles of SpeMreB3 and SpeMreB5. (**A-B**) Purification procedure of (**A**) SpeMreB3 and (**B**) SpeMreB5 from *E. coli* BL21 (DE3) carrying a codon-optimized *spemreB* cloned into pET-15b. The following fractions were visualized by a Coomassie stained 12.5% Laemmli gel: lane 1: lysate of *E. coli* carrying no plasmids; lane 2: lysate of uninduced *E. coli* carrying a plasmid for SpeMreB expression; lane 3: lysate of *E. coli* expressing an SpeMreB after IPTG induction; lanes 4 and 5: soluble (4) and insoluble (5) fractions of an SpeMreB expressing *E. coli* lysate; lanes 6 and 7: flow through (6) and elution (7) fractions of Ni^{2+}-NTA affinity chromatography; lane 8: a peak fraction of gel filtration. Protein size standards are visualized in lane M, with the molecular masses of each band on the right side. Arrow heads indicate the regions where the histidine-tagged SpeMreB bands appear. (**C-D**) Gel filtration profile of (**C**) SpeMreB3 and (**D**) SpeMreB5 after elution from a HiLoad 26/600 Superdex 200 pg column. Triangles indicate the peaks of the SpeMreB elution fractions. The elution volume of bovine γ-globulin (158 kDa), chicken ovalbumin (44 kDa), and horse myoglobin (17 kDa) are plotted as diamonds over the log of their molecular masses. From these elution spectra, the molecular masses of histidine-tagged SpeMreB3 and SpeMreB5 were estimated to be 44 and 46 kDa, respectively, indicating that both SpeMreBs were purified as monomers.
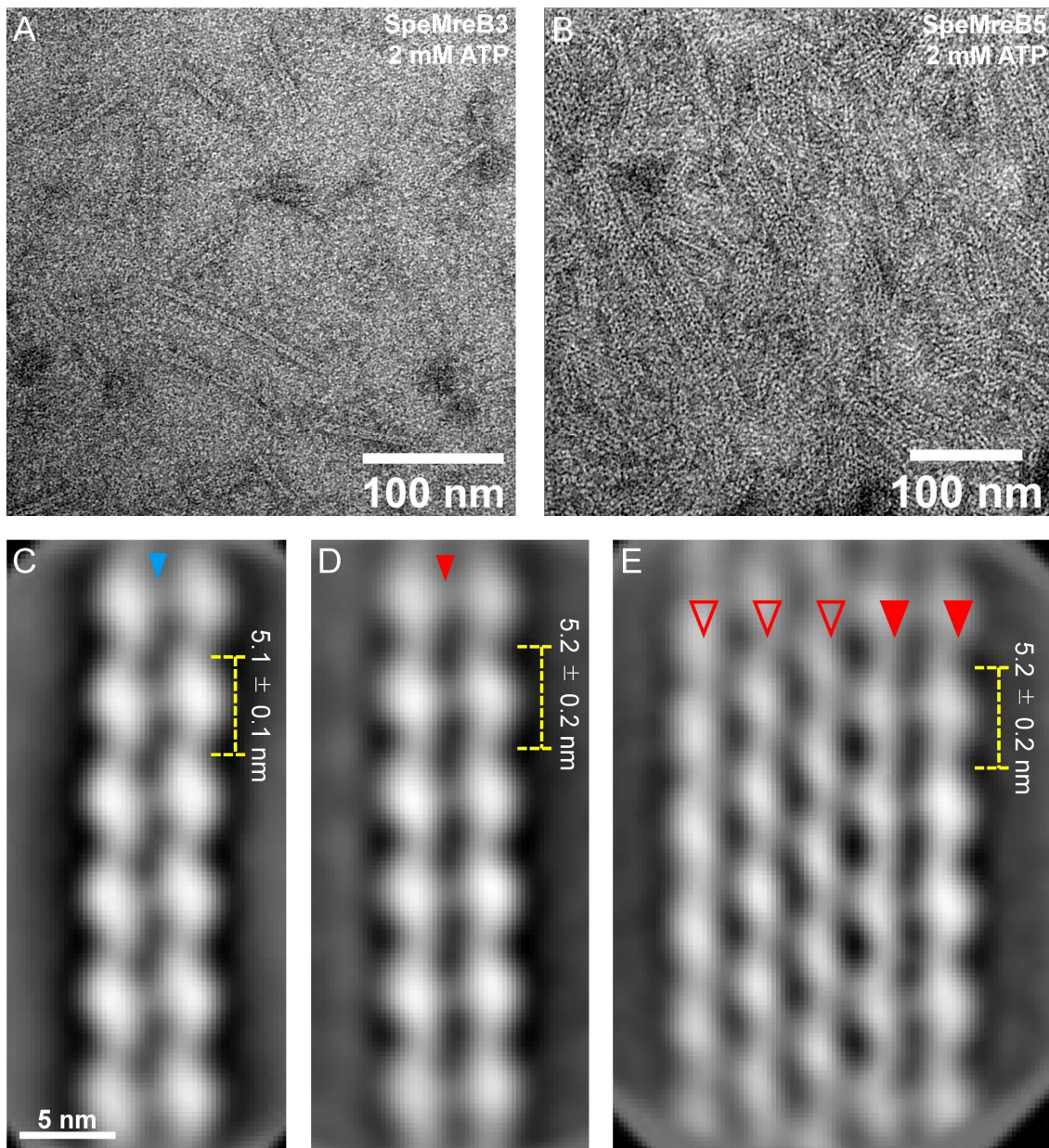
Figure II-2. Structures of SpeMreB3 and SpeMreB5 filaments observed by EM. (A-B) Negative-staining EM image of (**A**) 10 μM SpeMreB3 and (**B**) 5 μM SpeMreB5. The samples were diluted to 3 μM prior to placement onto an EM grid. (**C-D**) 2D averaged image of (**C**) SpeMreB3 and (**D**) SpeMreB5 filaments averaged from 2,874 and 652 particles, respectively. The estimated subunit repeats are 5.1 ± 0.1 and 5.2 ± 0.2 nm for SpeMreB3 and SpeMreB5, respectively. A weak electron density connecting the protofilaments is indicated by an arrow head. (**E**) 2D averaged image of the five-stranded SpeMreB5 sheet structure averaged from 1,575 particles. The estimated subunit repeat is 5.2 ± 0.2 nm. The protofilaments in the juxtaposed filament and the other protofilaments are indicated by solid and open arrow heads, respectively.
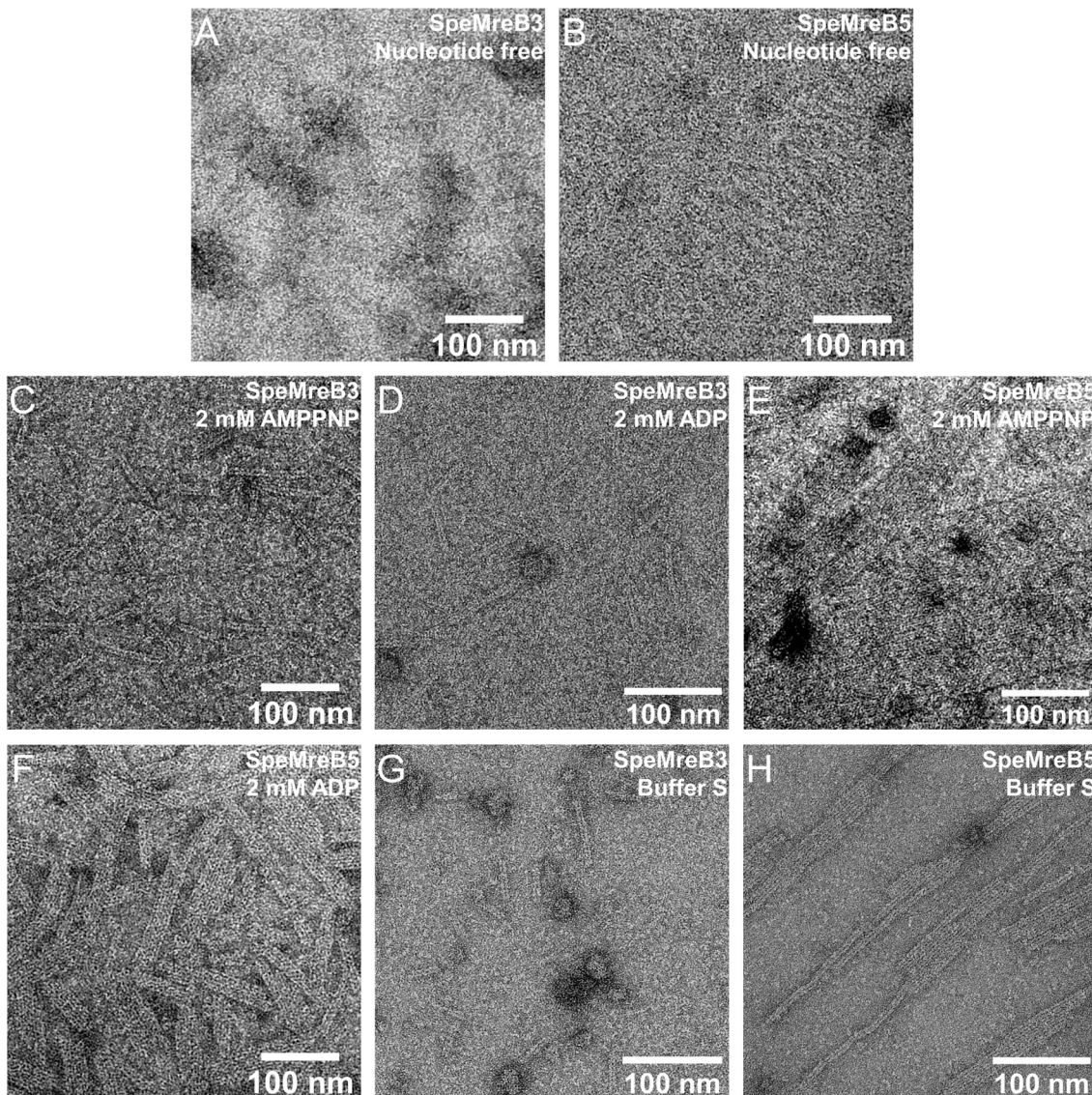
Figure II-3. Structures of SpeMreB3 and SpeMreB5 filaments under various conditions. The samples were diluted to 3 μM prior to placement on an EM grid. (**A-B**) Negative-staining EM images of (**A**) 10 μM SpeMreB3 and (**B**) 5 μM SpeMreB5 in the absence of Mg-ATP. (**C-D**) Negative-staining EM images of 10 μM SpeMreB3 polymerized with (**C**) 2 mM Mg-AMPPNP and (**D**) 2 mM Mg-ADP instead of Mg-ATP. (**E-F**) Negative-staining EM image of 5 μM SpeMreB5 polymerized with (**E**) 2 mM Mg-AMPPNP and (**F**) 2 mM Mg-ADP instead of Mg-ATP. (**G-H**) Negative-staining EM image of (**G**) 10 μM SpeMreB3 and (**H**) 5 μM SpeMreB5 polymerized in buffer S.

These SpeMreBs were individually incubated with or without 2 mM Mg-ATP in standard buffer (20 mM Tris-HCl pH 7.5, 100 mM KCl, and 5 mM DTT) and were imaged using negative-staining EM. In the presence of Mg-ATP, SpeMreB3 polymerized into

double-stranded filaments approximately 100 nm in length and without helicity (Fig. II-2A). This structure is comparable to that of CcMreB filaments (75). In contrast, SpeMreB5 formed sheet structures composed of multiple protofilaments with sub-micrometre length and width (Fig. II-2B). I did not find single protofilament structures for either SpeMreB, suggesting the necessity of inter-protofilament interactions in the assembly. Filamentous structures were not observed in the absence of Mg-ATP (Fig. II-3A and B), indicating that the polymerization is nucleotide-dependent.

To elucidate the subunit arrangement in these structures, I averaged the EM images using RELION ver. 3.1 or 4.0 software (176). I selected 13,077 SpeMreB3 and 117,740 SpeMreB5 images and obtained SpeMreB3 and SpeMreB5 filaments (Fig. II-2C and D) and SpeMreB5 sheets (Figs. II-2E, II-4A). The SpeMreB3 and SpeMreB5 filaments showed subunit repeats of 5.1 ± 0.1 and 5.2 ± 0.2 nm, respectively (Fig. II-2C and D). The two protofilaments were linked via a weak density in a juxtaposed manner. These features resemble those of CcMreB filaments (75). The SpeMreB5 sheets consisted of variable numbers of protofilaments aligned in a staggered manner (Figs. II-2E, II-4A open arrow heads) with a juxtaposed protofilament pair on one side (Figs. II-2E, II-4A solid arrow heads). The image of juxtaposed protofilament pair tended to be sharper than the other strands, indicating that the interactions to form juxtaposed pairs are less flexible than those of the staggered pair. Neither sheets composed of staggered protofilament pairs nor sheet composed of juxtaposed protofilament pairs were observed. Moreover, none of the sheets had juxtaposed double-stranded filaments on either side. These results indicate that the SpeMreB5 sheets are highly asymmetric and is composed of two distinct sets of inter-protofilament interactions.

To assess the polarity of these structures, I processed the 2D averaged images. I first

fitted each subunit density into an ellipse to determine each subunit axis, showing that the angles of all subunit axes are common for the juxtaposed filaments and SpeMreB5 sheet (Fig. II-4B, E, and K). Next, to assess the protofilament structural anisotropy, I overlaid two corresponding juxtaposed protofilament pairs. One pair was unprocessed and the other was rotated 180° or translated along the x-axis. The images rotated by 180° fit well with the original images (Fig. II-4C, F, and L), indicating that the juxtaposed pairs possess rotational symmetry and that the projection angle is only slightly different between the protofilaments in each pair. The SpeMreB3 filament exhibited mismatches at the pole regions (Fig. II-4C), reflecting filament bending. The juxtaposed protofilament pair in the SpeMreB5 sheet shows that the density of the edge-most protofilament is more evident than that of the adjacent protofilament, probably because of the flexibility of the adjacent protofilament (Fig. II-4L). However, the overlay of the translated SpeMreB5 images shows mismatches in the intra-protofilament interaction regions (Fig. II-4G and M), indicating that the protofilaments are asymmetric in the transverse direction. These results indicate that the juxtaposed protofilament pair of SpeMreB5 possesses antiparallel polarity, similar to the CcMreB filament (Fig. II-4H and I) (75). Although the mismatches in the overlay of the translated SpeMreB3 image were less obvious than those of SpeMreB5 (Fig. II-4D, G, and M), antiparallel polarity is the most plausible arrangement for the SpeMreB3 filament, as it resembles the antiparallel filaments of SpeMreB5 and CcMreB. I also overlaid two SpeMreB5 sheet images, one of which was unprocessed and the other was translated along the x- and y-axes. The protofilament adjacent to the antiparallel protofilament pair fit well with the neighbouring protofilaments on both sides (Fig. II-4N), indicating that the staggered protofilaments were aligned in a parallel manner (Fig. II-4J).
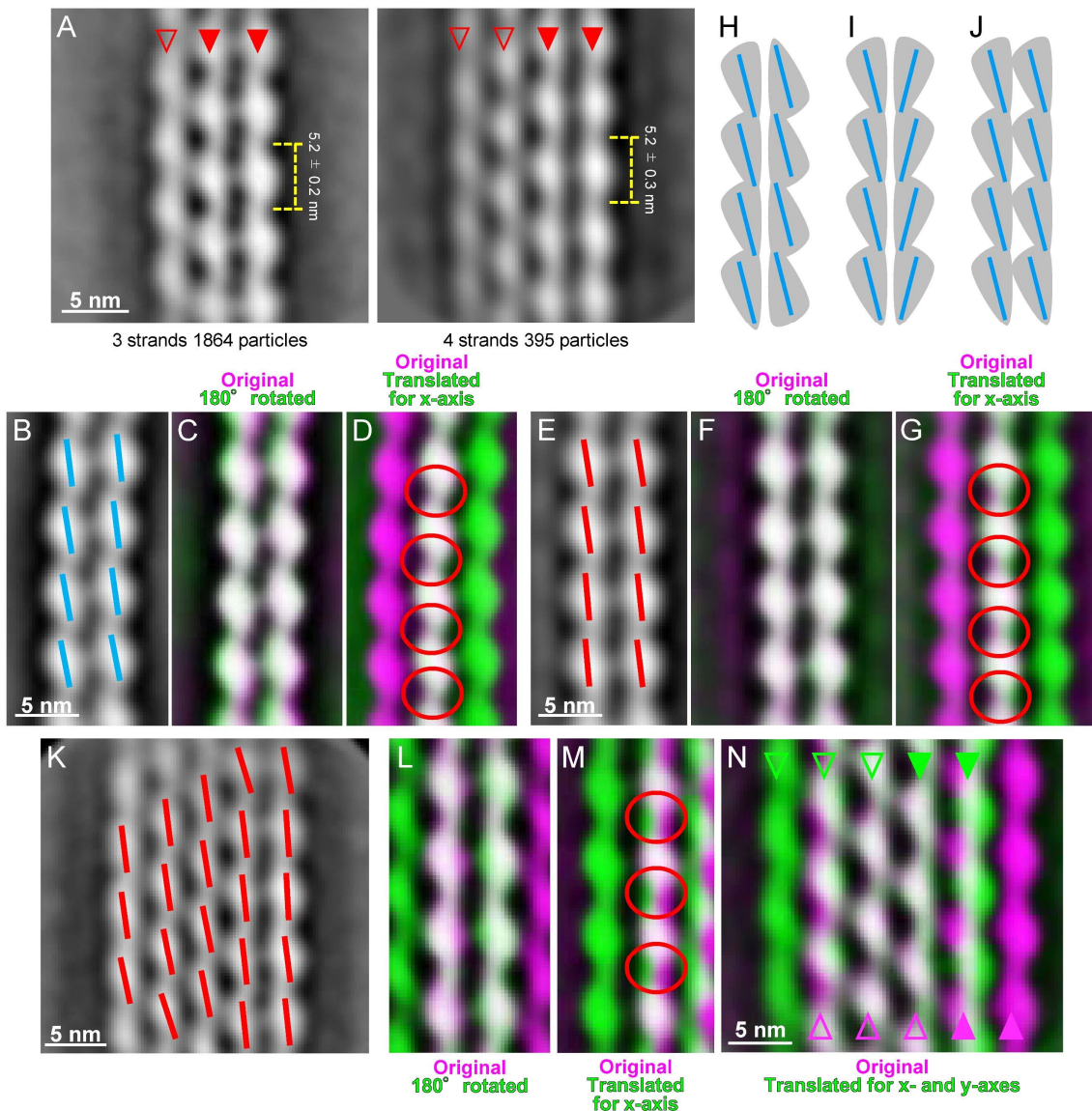
Figure II-4. Structural characteristics of SpeMreB3 and SpeMreB5 filaments. (**A**) SpeMreB5 sheet images composed of three (left) and four (right) protofilaments. The subunit repeats of the protofilaments and the particle number of triple- and quadruple-stranded sheets are 5.2 ± 0.2 and 5.2 ± 0.3 nm, respectively, and 1,864 and 395, respectively. The protofilaments in the juxtaposed filaments and the other protofilaments are indicated by solid and open arrow heads, respectively. (**B**) 2D averaged image of the SpeMreB3 filament with the axis of each subunit shown as cyan lines. (**C-D**) Merged images of two SpeMreB3 filament images. One filament image is colored green and (**C**) rotated 180° and (**D**) translated with a distance corresponding to a protofilament width toward the x-axis. The original image is colored magenta. Merged regions are shown in white. The unmatched intra-protofilament interaction regions in panel D are indicated by red circles. (**E**) 2D averaged image of the SpeMreB5 filament with the axis of each subunit shown with a cyan line. (**F-G**) Merged images of two SpeMreB5 filament images. One filament image is colored green and (**F**) rotated 180° and

Figure II-4 (continued) (**G**) translated with a distance corresponding to a protofilament width toward the x-axis. The original image is colored magenta. Merged regions are shown in white. The unmatched intra-protofilament interaction regions in panel G are indicated by red circles. (**H-J**) Schematic illustrations of non-helical filaments showing (**H**) antiparallel and (**I-J**) parallel polarity with intra-protofilament interaction regions directed on the (**H-I**) opposite and (**J**) same sides. The axis of each subunit is shown by a cyan line. (**K**) 2D averaged image of the five-stranded SpeMreB5 sheet, with the axis of each subdomain shown with red lines. (**L-N**) Merged images of two SpeMreB5 sheet images with five protofilaments. (**L-M**) The juxtaposed protofilament pair of a sheet image (green) was extracted, (**L**) rotated 180° or (**M**) translated with a distance corresponding to a protofilament width toward the x-axis, and overlayed to an unprocessed sheet image (magenta). For panel L, magenta and green show higher intensities than the other colors for the left and right original protofilaments, respectively, indicating that the edge-most protofilament is more obvious than the adjacent one. The unmatched intra-protofilament interaction regions in panel M are indicated by red circles. (**N**) A sheet image (green) was shifted with distances corresponding to a protofilament width toward the x-axis and a half of a subunit length toward the y-axis to fit protofilaments in a staggered alignment. The processed image was overlayed to an unprocessed sheet image (magenta). Protofilament positions of the sheet images are indicated with triangles with corresponding colors.

Filament formation by EcMreB requires nucleotide hydrolysis (177). To determine whether this was also the case for SpeMreB3 and SpeMreB5, I conducted negative-staining EM of SpeMreB3 and SpeMreB5 incubated in the presence of 2 mM Mg-AMPPNP or Mg-ADP. SpeMreB3 incubated with Mg-AMPPNP or Mg-ADP formed double-stranded filaments (Fig. II-3C and D), while SpeMreB5 incubated with Mg-AMPPNP or Mg-ADP formed sheet structures (Fig. II-3E and F). These results indicate that SpeMreB3 and SpeMreB5 polymerization is driven by nucleotide binding, rather than hydrolysis.

SpeMreB3 crystal structure

SpeMreB3 crystals suitable for X-ray experiments grew under several conditions but they showed merohedral twinning. To overcome this problem, I methylated the lysine

residues of SpeMreB3 (178, 179) and crystallized the modified protein (Fig. II-5A and B). The crystal structures of Nf-SpeMreB3 and SpeMreB3-AMPPNP complex were determined at 1.90 and 1.75 Å resolution, respectively (Figs. II-6A, II-7A, Table II-1). SpeMreB3 adopts a canonical actin fold composed of four subdomains (IA, IB, IIA, and IIB) and consists of the same secondary structure elements as CcMreB, TmMreB, and SciMreB5, except for the C-terminal region (37, 75, 85, 131). The N-terminal amphipathic helix (Figs. I-1E, I-3 purple box) was not modeled for either the Nf-SpeMreB3 or SpeMreB3-AMPPNP complexes because of poor electron density.
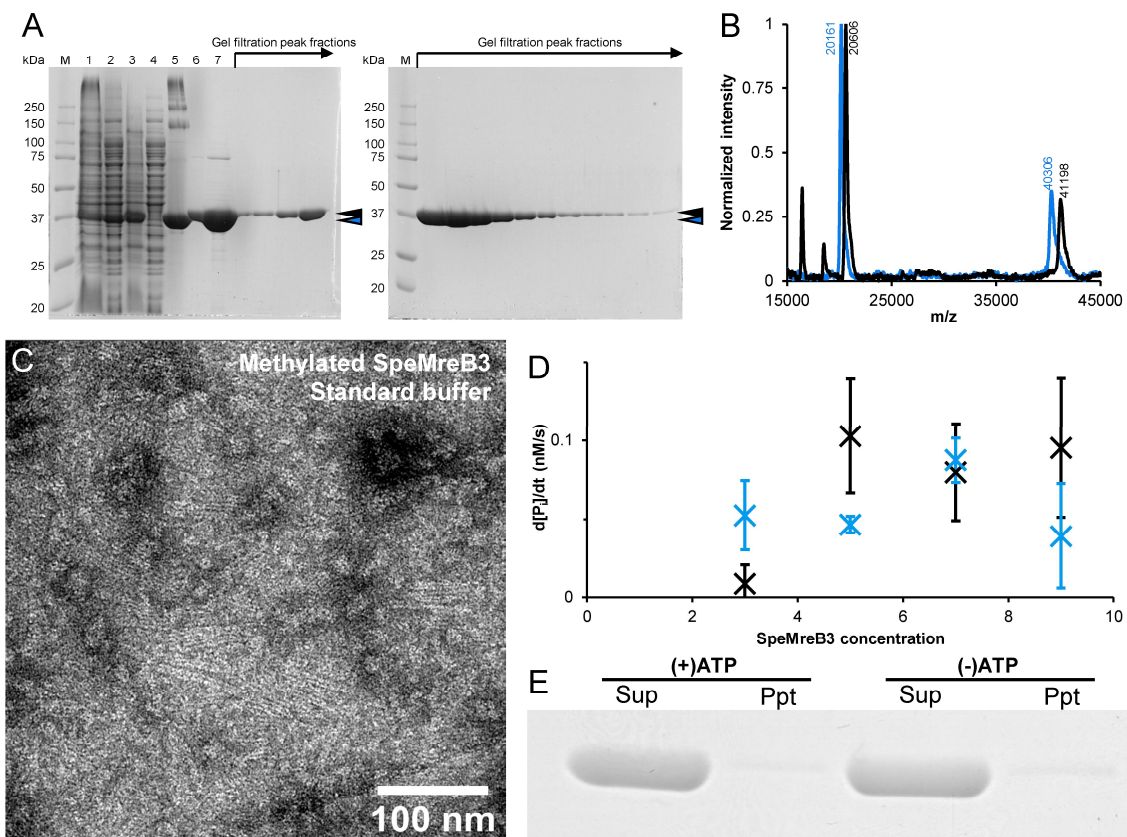

Figure II-5. Purification and polymerization of methylated SpeMreB3. (**A**) Procedure for purifying methylated SpeMreB3 from *E. coli* C43 (DE3) carrying codon-optimized *spemreB3* cloned into pCold-15b. The following fractions were visualized by Coomassie staining of a 12.5% Laemmli gel: lane 1: lysate of *E. coli* expressing SpeMreB3 after IPTG induction; lanes 2 and 3: soluble (2) and insoluble (3) fractions of SpeMreB3-expressing *E. coli* lysate; lanes 4 and 5: flow through (4) and elution (5) fractions of Ni^{2+}-NTA affinity chromatography; lane 6: SpeMreB3 after methylation;

Figure II-5 (continued) lane 7: load fraction for gel filtration; others: elution fractions of gel filtration. Protein size standards are visualized in lane M, with the molecular masses of each band on the left side. The cyan and black arrow heads indicate the regions for unmethylated SpeMreB3 and methylated SpeMreB3, respectively. (**B**) Mass spectra of unmethylated SpeMreB3 (cyan) and methylated SpeMreB3 (black). From these spectra, the increased SpeMreB3 molecular mass after methylation was calculated as 891 ± 20 Da. The estimated methylating ratio was $96.5 \pm 2.2\%$, because SpeMreB3 has 33 lysine residues, and the molecular mass is increased by 28 Da per lysine by the reaction. (**C**) Negative-staining EM image of 75 µM methylated SpeMreB3 polymerized in standard buffer. (**D**) Concentration dependence of P_i release rates from unmethylated SpeMreB3 (cyan) and methylated SpeMreB3 (black). Error bars indicate the S.D. from three repeated measurements. (**E**) Sedimentation assay of 8 µM methylated SpeMreB3, which was polymerized for 3 h with buffer S and subjected to centrifugation at $436,000 \times g$ for 120 min at 23°C. Each fraction was diluted three times to prepare the sample for SDS-PAGE.

Table II-1. X-ray data collection and refinement statistics. Values in parentheses are the highest resolution shell. $R_w = \sum \| F_o | - | F_c \| / \sum | F_o |$, $R_{free} = \sum \| F_o | - | F_c \| / \sum | F_o |$.

| Crystal	Nf-SpeMreB3	SpeMreB3-AMPPNP
Space group	$P2_1$	$P2_1$
Cell dimensions		
a, b, c (Å)	52.4, 68.1, 54.6	50.3, 56.3, 120.5
α, β, γ (deg)	90.0, 91.7, 90.0	90.0, 90.6, 90.0
Wavelength (Å)	1.000	1.000
Resolution (Å)	54.5–1.90 (1.94–1.90)	56.3–1.75 (1.78–1.75)
R_{merge}	0.094 (0.542)	0.101 (0.570)
$CC_{1/2}$	0.996 (0.866)	0.993 (0.658)
$I/\sigma I$	9.8 (2.7)	6.8 (1.8)
Completeness (%)	100.0 (100.0)	97.2 (95.8)
Redundancy	5.3 (5.2)	3.3 (3.3)
Resolution range (Å)	54.5–1.90 (1.95–1.90)	51.0–1.75 (1.79–1.75)
No. of reflections working	28,311 (2032)	64,014 (4479)
No. of reflections test	2001 (127)	2006 (148)
R_w (%)	18.5 (22.1)	17.4 (22.8)
R_{free} (%)	25.4 (28.1)	21.4 (25.3)
Rms deviation bond length (Å)	0.004	0.006
Rms deviation bond angle (deg)	0.614	0.891
B-factors		
Protein atoms	27.4	25.1
Ligand atoms	20.4	17.9
Solvent atoms	28.5	26.0
Ramachandran plot (%)		
Most favored	98.6	97.4
Additionally allowed	1.4	2.6
Generously allowed	0.0	0.0
Disallowed	0.0	0.0
No. of protein atoms	2519	5170
No. of ligand atoms	5	64
No. of solvent atoms	333	763
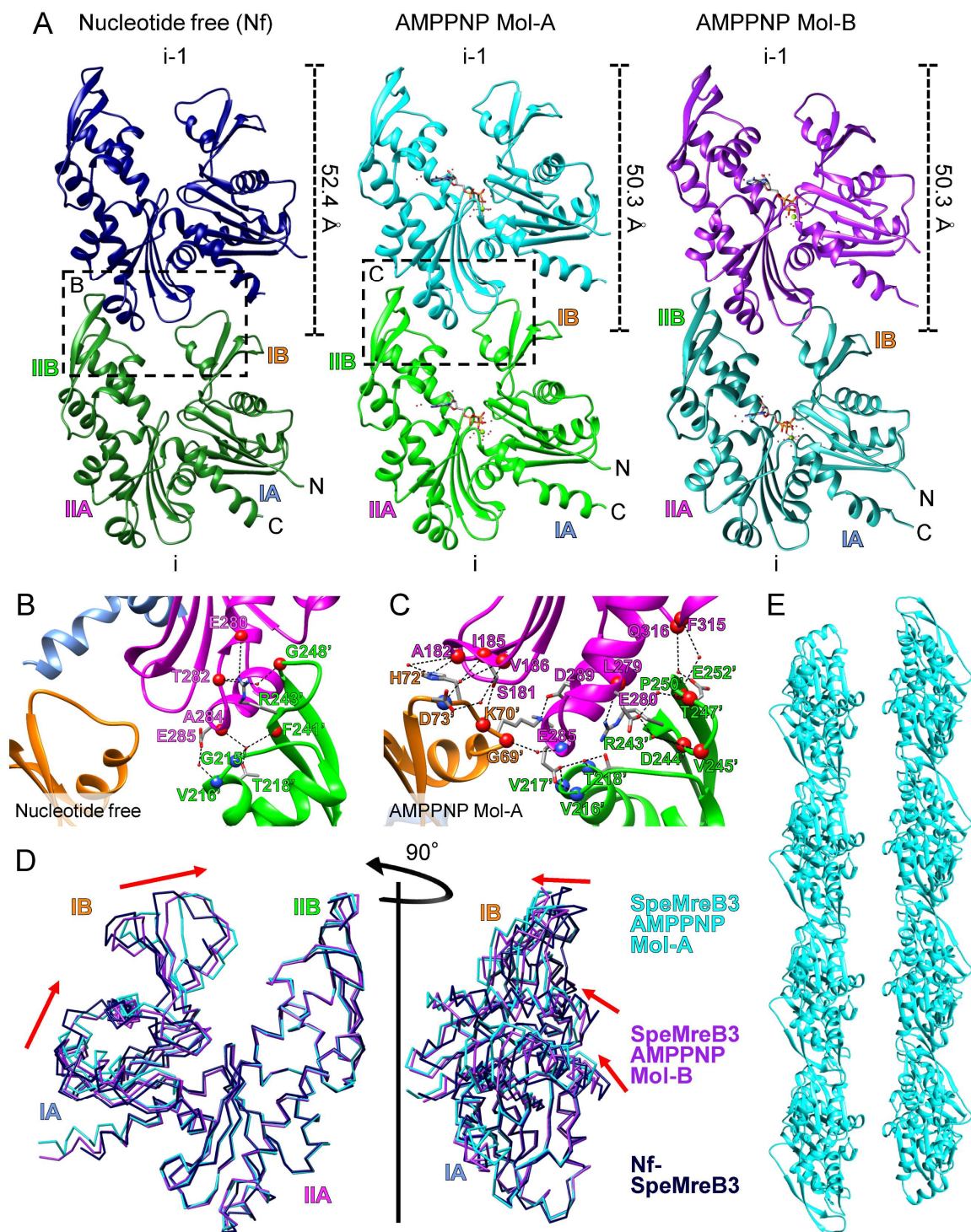
Figure II-6. Crystal structures of SpeMreB3. Figure II-6. (A) Protofilament structures in crystals of Nf-SpeMreB3 and SpeMreB3-AMPPNP complexes. Two different conformations (Mol-A and B) in the asymmetric unit of the SpeMreB3-AMPPNP complex crystal are shown in the center and right panels, respectively. Two subunits in the protofilaments are labelled as i and i−1. The subunit repeat is indicated at the right of each i−1 subunit. The four subdomains (IA, IB, IIA, and IIB) and N- and

Figure II-6 (continued) C-termini are labelled on the i subunit. The boxed regions on Nf and AMPPNP complex Mol-A protofilaments are magnified in panel B and C, respectively, to represent the intra-protofilament interactions. (**B-C**) Close up view of the subunit interface in protofilaments in the crystal of (**B**) Nf-SpeMreB3 and (**C**) the SpeMreB3-AMPPNP complex Mol-A. Subdomains IA, IB, IIA, and IIB are indicated by ribbon representations colored with light blue, orange, magenta, and green, respectively. Hydrogen bonds and electrostatic interactions are indicated by broken lines. The residues involved in the hydrogen bonding or electrostatic interaction network are indicated by stick models or blue (backbone nitrogen atom) or red (backbone oxygen atom) spheres with labels. Water molecules involved in the interactions are shown as small red spheres. (**D**) Structural comparison of Mol-A and B in the SpeMreB3-AMPPNP complex and Nf-SpeMreB3. The structures are superimposed onto the subdomains IIA and IIB of Mol-A. Movement of the subdomain IA and IB relative to Nf-SpeMreB3 is indicated by red arrows. (**E**) A ribbon representation of the filament structure of SpeMreB3-AMPPNP Mol-A fit to the EM image (Figs. II-2C, II-7E).

The Nf-SpeMreB3 crystal belongs to the space group $P2_1$ and contains a single molecule in an asymmetric unit. Nf-SpeMreB3 forms protofilaments along the crystal a axis in the $P2_1$ crystal. Thus, the protofilaments are arranged in an antiparallel manner (Fig. II-8A). The subunit arrangement in the protofilament (Fig. II-6A) resembles that of CcMreB, TmMreB, and SciMreB5 protofilaments in their respective crystals (37, 75, 85, 131). The interaction between IIA and IB' (with and without a prime indicating i and i−1 subunits, respectively), which has been observed in CcMreB, TmMreB, and SciMreB5 protofilaments, is not found in the Nf-SpeMreB3 protofilament, whereas the IIA-IIB' interaction is conserved in Nf-SpeMreB3 (Fig. II-6B). This IIA-IIB' interaction is mediated by a hydrogen-bonding network and is stabilized by an electrostatic interaction between E285 and the N-terminal end of the α-helix starting from V216'.
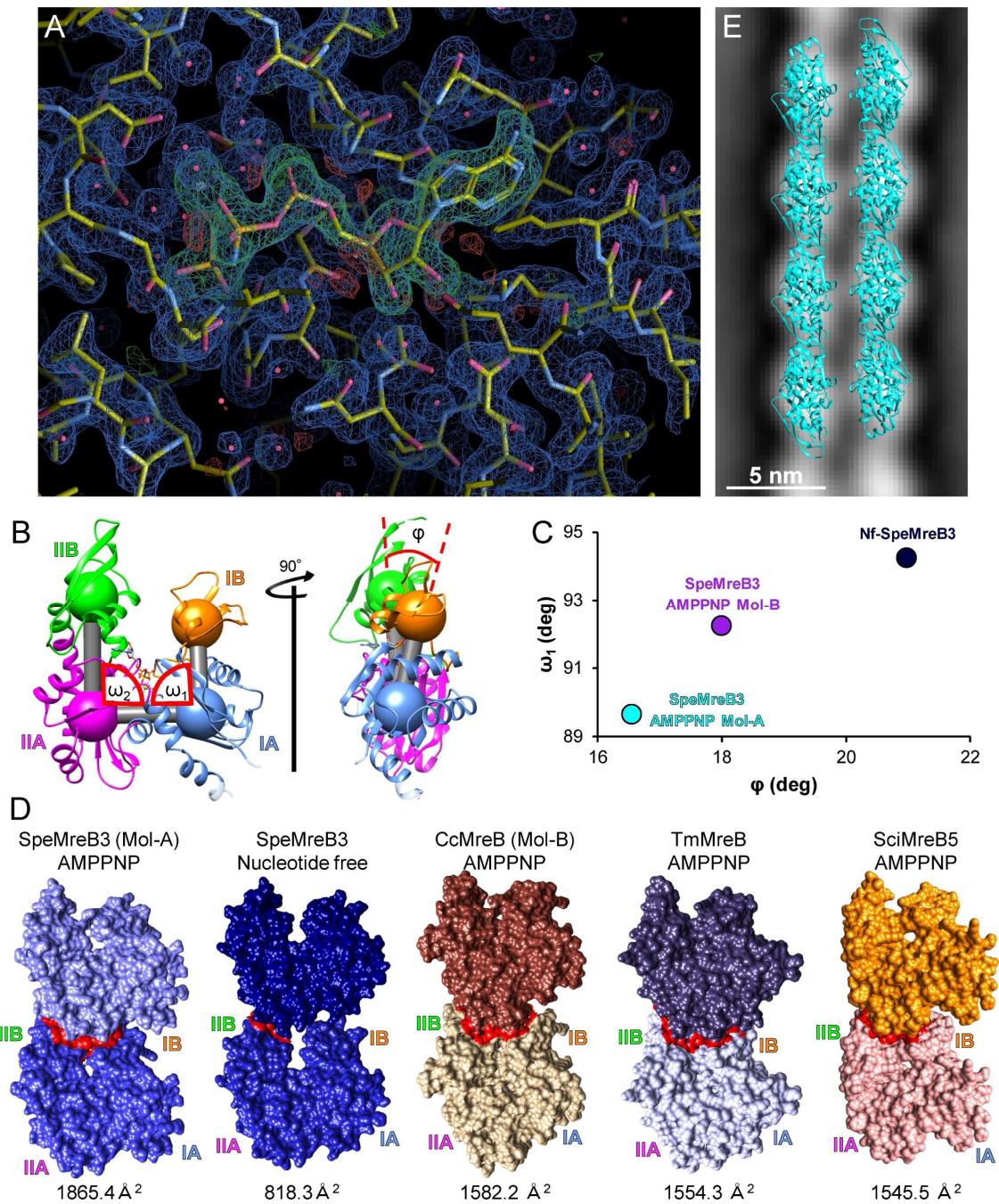
Figure II-7. Electron density map of the SpeMreB3 active site and structural features of MreB protofilaments. (**A**) Nucleotide binding site. The 2Fo−Fc density map contoured at 2.0 sigma (blue) and the Fo−Fc density map contoured at 2.0 sigma (green) are superimposed onto the refined model. The Mg-AMPPNP moiety was omitted from the model for phase calculation. (**B**) Scheme of the domain angle analyses. (Left) Front view of a ribbon representation of the SpeMreB3-AMPPNP complex Mol-A in which the subdomains IA, IB, IIA, and IIB are colored light blue, orange, magenta, and light green, respectively. Centroids of each subdomain are shown in spheres with

Figure II-7 (continued) the colors corresponding to each subdomain and connected with a grey cylinder. The transparent regions on IA were excluded from the centroid calculation because the regions corresponding to the N- and C-termini are not modeled in SpeMreB3-AMPPNP complex Mol-B and Nf-SpeMreB3, respectively. The angles composed of centroids of subdomains IIA-IA-IB and IIB-IIA-IA are defined as ω_1 and ω_2, respectively. (Right) Side view of a ribbon representation of Nf-SpeMreB3. The dihedral angle composed of the subdomains IIB-IIA-IA-IB is defined as φ. (**C**) Correlation of φ and ω_1 among my SpeMreB3 crystal structures. (**D**) Surface representation of two subunits in the protofilaments of SpeMreB3-AMPPNP Mol-A, Nf-SpeMreB3, CcMreB (PDB ID: 4CZJ), TmMreB (PDB ID: 1JCG), and SciMreB5 (PDB ID: 7BVY). The four subdomains (IA, IB, IIA, and IIB) of i subunit are labeled. The subunit interface is colored with red. The subunit interface area with a 2.5 Å cut-off (calculated using Chimera ver. 1.13.1) is shown below each model. (**E**) Fitted ribbon representing SpeMreB3 protofilaments composed of Mol-A of AMPPNP complexes (Fig. II-6A) in the 2D averaged EM image (Fig. II-2C).
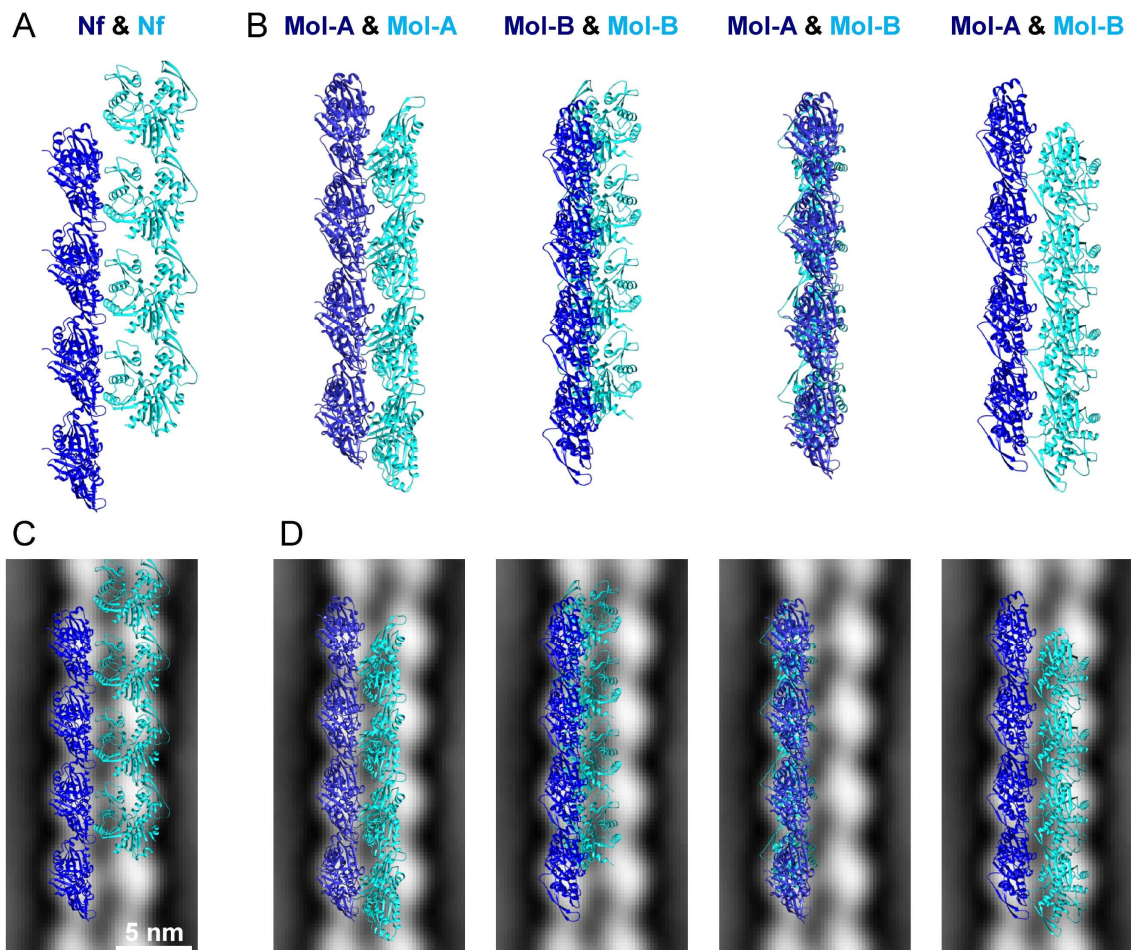
Figure II-8. All protofilament pairs in SpeMreB3 crystals. (**A**) A ribbon representation of the antiparallel protofilament pair found in Nf-SpeMreB3 crystal. (**B**) The ribbon representation of one parallel protofilament pair (the right most) and three antiparallel protofilament pairs (the others)

Figure II-8 (continued) found in crystals of the SpeMreB3-AMPPNP complex. The shown molecule is indicated above each antiparallel pair with corresponding colors. (**C-D**) Overlay of the protofilament pairs of (**C**) Nf-SpeMreB3 and (**D**) SpeMreB3-AMPPNP complex onto the 2D averaged image of the SpeMreB3 filament.

The asymmetric unit of SpeMreB3-AMPPNP complex includes two molecules (Mol-A and Mol-B) with an RMSD value estimated for Cα atoms of 0.891 Å (Fig. II-6A). These molecules are related by a pseudo two-fold symmetry axis perpendicular to the crystal *a* axis in an asymmetric unit. Each SpeMreB3 molecule in the asymmetric unit forms a protofilament with those in the neighbouring unit cells along the crystal *a* axis. Thus, the SpeMreB3-AMPPNP complex crystal also contains antiparallel pairs of the protofilaments (Fig. II-8B), although their arrangement differs from that of the Nf-SpeMreB3 crystal (Fig. II-8A). To quantitatively evaluate the domain opening, I measured the angles within the subdomains (Fig. II-7B). The two molecules showed small differences in domain conformation, in which the angles composed of centroids of subdomains IIA-IA-IB (ω_1) and the dihedral angle (φ) of SpeMreB3-AMPPNP complex Mol-A were 2.6° and 2.0° narrower than those of Mol-B, respectively (Fig. II-7B and C). Therefore, Mol-A had a slightly narrower nucleotide-binding cleft and a more flattened overall conformation compared to Mol-B (Fig. II-6D). Nf-SpeMreB3 had larger ω_1 and φ values than SpeMreB3-AMPPNP complex Mol-A (4.6° and 3.5°, respectively; Fig. II-7C), showing a wider nucleotide-binding cleft and a more uneven overall conformation (Fig. II-6D). This conformational difference is similar to that between CcMreB monomers and protofilaments (180). The angle composed of centroids of subdomains IIB-IIA-IA (ω_2) was more constant than ω_1 among my crystal structures (ω_2 = 88.9° for SpeMreB3-AMPPNP complex Mol-A, 90.3° for Mol-B, and 91.2° for Nf-SpeMreB3), indicating that major structural changes upon nucleotide binding contribute to swing the subdomain IB.

These conformational changes lead to the interaction between subdomains IIA and IB', which is absent in the Nf-SpeMreB3 protofilament (Fig. II-6B and C). The interaction in SpeMreB3-AMPPNP complex Mol-A is mediated through a hydrogen-bonding network and is stabilized by an electrostatic interaction between D289 and K70' (Fig. II-6C). The IIA-IIB' interaction area of SpeMreB3-AMPPNP complex Mol-A is also wider than that of Nf-SpeMreB3 (Fig. II-6B and C). As observed for Nf-SpeMreB3, E285 in the SpeMreB3-AMPPNP complex interacts electrostatically with the N-terminal end of the α-helix starting from V216'. The subunit interface area in the protofilament of SpeMreB3-AMPPNP is comparable to that of the other MreB protofilaments, whereas that of Nf-SpeMreB3 is much smaller (Fig. II-7D).

The subunit repeats along the protofilament in the crystal are in good agreement with those of the protofilament in the EM image (Figs. II-2C, II-6A). Therefore, I fitted the filament model in the crystal onto the 2D averaged EM image of the SpeMreB3 filament. The protofilament model of the SpeMreB3-AMPPNP complex fits well with the protofilament image in an antiparallel manner (Figs. II-6E, II-7E), suggesting that the protofilament structure in the double-stranded filament (Fig. II-2C) is the same as that in the crystal. However, none of the antiparallel protofilament pairs in the crystal fit onto the double-stranded filament in the EM image (Fig. II-8C and D), indicating that the interaction that stabilizes the double-stranded filament in solution differs from that in the crystal.

The "E ⋯ T - X - [D/E]" motif is involved in P_i release from SpeMreB3 and SpeMreB5

Next, I measured ATPase activity of SpeMreB3 and SpeMreB5 using a P_i release assay. The reactions were initiated by adding a mixture of $MgCl_2$, ATP, and MESG, a

molecular probe for P_i (181-185), to SpeMreBs in standard buffer. SpeMreB5 hydrolyzed ATP and released P_i over time (Fig. II-9A and B). The P_i release rate constant was 1.5 ± 0.2 nM (P_i)/s/μM (protein), as estimated from the linear-fit slope of SpeMreB5 concentration-dependent P_i release rates (Fig. II-9C). This value is consistent with those of SciMreB5, TmMreB, EcMreB, and actin (Table II-2) (131, 177, 183, 184, 186). However, the P_i release of SpeMreB3 was too slow to estimate the rate constant, even at 10 μM (Fig. II-9A-C, Table II-2), a concentration at which I observed filaments using EM (Figs. II-2A, II-3C and D).

- 52 -
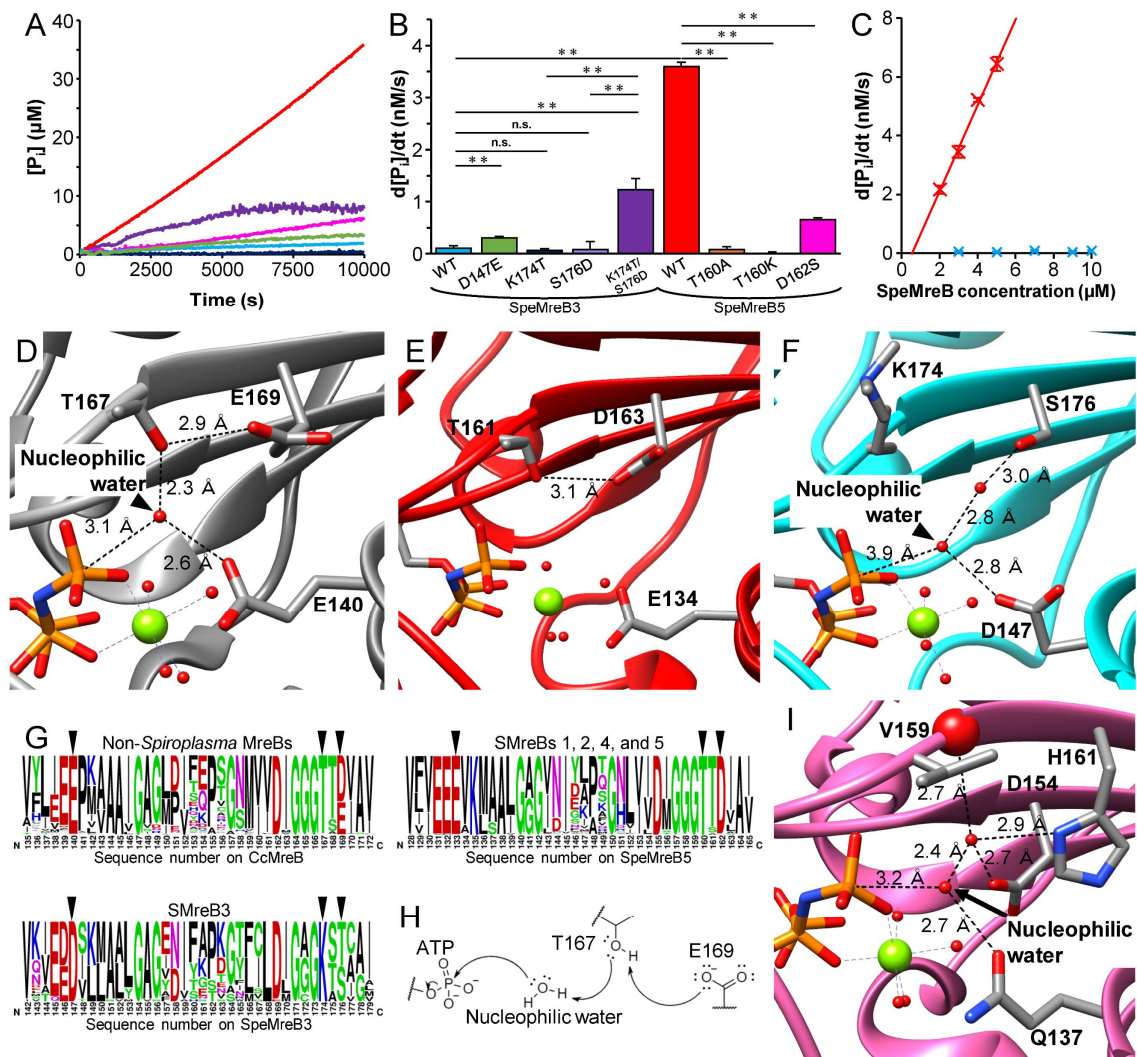
Figure II-9. P_i release measurement and comparison of active site structures of SpeMreB3 and SpeMreB5. (**A**) Time course plots of P_i release from 3 μM SpeMreB3 WT (cyan), SpeMreB3 D147E (light green), SpeMreB3 K174T (navy blue), SpeMreB3 K174T/S176D (purple), SpeMreB5 WT (red), and SpeMreB5 D162S (pink) in the presence of 2 mM ATP. The measurements were performed three times, and a representative curve is plotted in the graph. (**B**) P_i release rates from SpeMreBs estimated from the time course plots. Error bars indicate S.D. from three repeated measurements. Symbols indicate *p*-value supported by Student's *t*-test (** $p < 0.01$, n.s. $p > 0.05$). (**C**) Concentration dependence of P_i release from SpeMreB3 (cyan) and SpeMreB5 (red). Error bars indicate the S.D. from three repeated measurements. (**D-F**) Close up view of the active sites of (**D**) the CcMreB-AMPPNP complex (PDB ID: 4CZJ), (**E**) the SciMreB5-AMPPNP complex (PDB ID: 7BVY), and (**F**) the SpeMreB3-AMPPNP complex (Mol-A). Mg^{2+} and water molecules are indicated as green and red spheres, respectively. (**G**) WebLogos of amino acid sequences around the ATP hydrolysis region from: (left upper) 4,832 MreB family proteins from non-*Spiroplasma* bacteria used for phylogenetical analyses (Fig. I-2A), (left lower) 29 SMreB3, and (right) 171 SMreBs (except for SMreB3). The corresponding amino acid for the core amino acids motif for ATP hydrolysis (E140, T167, and E169 in CcMreB) are indicated by arrow heads. (**H**) A working model for ATP hydrolysis in MreB family proteins. Residues corresponding to T167 and E169 in CcMreB, the nucleophilic water molecule, and the γ-P_i of ATP are shown in the model. The unshared electron pairs of each atom on the residues and the water are indicated by two neighbouring dots. A putative electron transfer pathway is indicated by arrows. (**I**) Close up view of the active sites of AMPPNP-bound F-actin (PDB ID: 7W4Z). Mg^{2+} and water molecules are indicated as green and red spheres, respectively.

Table II-2. Summary of P_i release rates of actin superfamily proteins including SpeMreB3 and SpeMreB5.

|	SpeMreB3	SpeMreB5	SciMreB5	TmMreB	EcMreB
k_{obs} (nM(P_i)/s/μM(protein))	N.D.	1.5 ± 0.2	2.5 ± 0.1	1.7 ± 0.2	2.8 ± 0.2
Reference	This study	This study	(131)	(186)	(177)
	Actin	Actin	MamK	AlfA	FtsA
k_{obs} (nM(P_i)/s/μM(protein))	2.2	2.6 ± 0.4	3.3	>6.7	11.7 ± 1.5
Reference	(183)	(184)	(187)	(188)	(189)

To elucidate the structural basis of the slow P_i release rate, I compared the active site structures of CcMreB (PDB ID: 4CZJ), SciMreB5 (PDB ID: 7BVY), and SpeMreB3 all complexed with AMPPNP (Fig. II-9D-F). In the CcMreB structure, E140 and T167 coordinate with a putative nucleophilic water molecule that attacks the γ-P_i of ATP. T167 also forms a hydrogen bond with E169, which is thought to be unrelated to ATP hydrolysis

(Fig. II-9D) (75). These residues are structurally conserved in SciMreB5 (E134, T161, and D163 in Fig. II-9E), although no nucleophilic water molecules were observed in the SciMreB5 structure. In the SpeMreB3 structure, D147 and K174 are located at positions corresponding to E140 and T167 in CcMreB, respectively. However, D147 is far from the putative nucleophilic water molecule and K174 does not interact with water molecules. The residue corresponding to E169 is replaced by serine (S176) in SpeMreB3, which does not interact with K174 (Fig. II-9F). Therefore, the slow P_i release rate of SpeMreB3 can be attributed to these three residues.

To elucidate the role of these residues in SpeMreBs ATPase activity, I designed four SpeMreB3 variants (D147E, K174T, S176D, and K174T/S176D) and three SpeMreB5 variants (T160A, T160K, and D162S, which are equivalent to the T161A, T161K, and D163S mutations on SciMreB5, respectively). All the variants formed filamentous structures (Fig. II-10). The P_i release rate of SpeMreB3 D147E was higher than that of the WT. P_i release by SpeMreB3 K174T and SpeMreB3 S176D was similar to that of the WT, whereas P_i release by SpeMreB3 K174T/S176D was as high as 1.2 nM/s at 3 μM protein concentration (Fig. II-9A and B). The P_i release rates of SpeMreB5 T160A, T160K, and D162S were at least 5.6-fold slower than those of the WT (Fig. II-9A and B). These results indicate that the amino acid motif "E ⋯ T - X - [D/E]" is important for P_i release from SpeMreBs and that the Thr–Asp/Glu pair plays a role in ATPase activity distinct from that of the first glutamate in the motif.

To determine whether "E ⋯ T - X - [D/E]" is conserved in MreB family proteins, I analyzed the amino acid sequences of MreBs from all bacterial phyla (Fig. II-9G). The motif was conserved in 95.8% of MreB family proteins in non-*Spiroplasma* species and in 98.2% of SMreBs, except for SMreB3 (Fig. II-9G, left upper and right). In all known

SMreB3, the residues corresponding to E140 and T167 in CcMreB were replaced with aspartate and lysine, respectively. Moreover, the residue corresponding to E169 in CcMreB was replaced with serine or threonine (Fig. II-9G, lower left). These findings suggest that the "E ⋯ T - X - [D/E]" motif is important for P_i release by MreB family proteins, except for SMreB3.
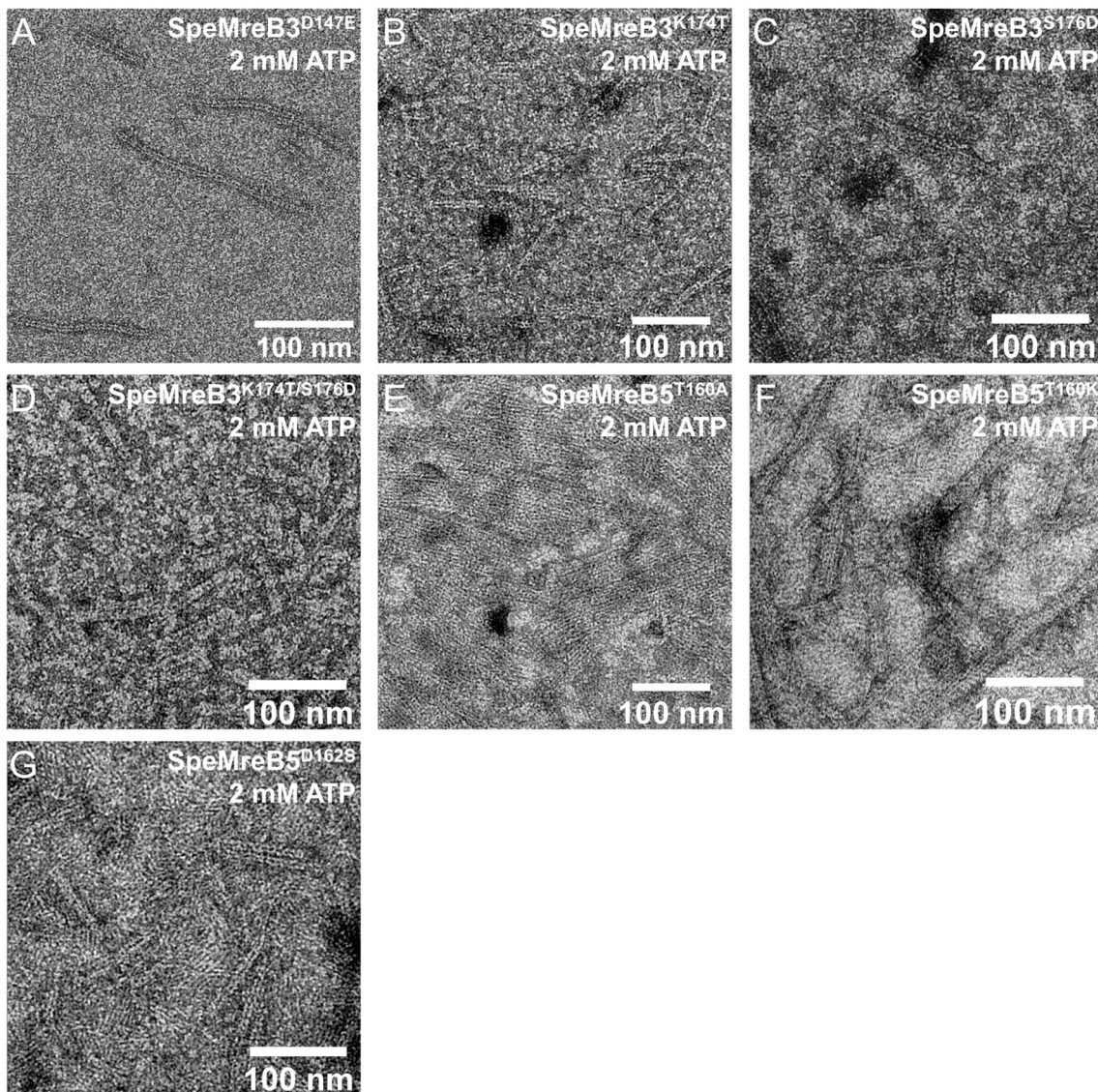
Figure II-10. Filamentous structures of SpeMreB3 and SpeMreB5 variants. The samples were diluted to 3 μM prior to placement on an EM grid. (**A-F**) Negative-staining EM images of (**A**) 10 μM SpeMreB3 D147E, (**B**) 10 μM SpeMreB3 K174T, (**C**) 10 μM SpeMreB3 S176D, (**D**) 10 μM SpeMreB3 K174T/S176D, (**E**) 5 μM SpeMreB5 T160A, (**F**) 5 μM SpeMreB5 T160K, and (**G**) 5 μM SpeMreB5 D162S polymerized in standard buffer.

Critical concentrations of SpeMreB3 and SpeMreB5 and their variants

To evaluate SpeMreB3 and SpeMreB5 polymerization activity, I measured their critical concentrations, which reflect the minimum concentration required for polymerization and the steady state filament amounts, by sedimentation assays. However, significant amounts of proteins precipitated even without nucleotides in standard buffer used for EM observation and P_i release assay, while no filamentous structure was observed by EM in the nucleotide-free condition (Figs. II-3A and B, II-11A), suggesting that the amorphous aggregation affected the measurements. Therefore, I searched for a solution in which the proteins did not form aggregates without Mg-ATP but polymerized in the presence of Mg-ATP. I found that a solution containing 20 mM Tris-HCl pH 8.0, 1 M NaCl, 200 mM L-arginine-HCl pH 8.0, and 5 mM DTT (buffer S) was suitable for sedimentation assays (Figs. II-3G and H, II-11B and C).

To estimate the time required to a reach steady state, protein samples in buffer S were incubated with 2 mM Mg-ATP for 1, 3, and 6 h and centrifuged. No significant differences were found in pellet amounts (Fig. II-11D), indicating that SpeMreB polymerization reached a steady state within 1 h. Therefore, sedimentation assays were conducted after incubation for 1 h.

The critical concentration of SpeMreB5 was estimated to be 0.14 ± 0.07 μM which is comparable to that of actin polymerized in a standard buffer for the actin polymerization, KMEI buffer (0.12–0.24 μM), and of walled-bacterial MreBs in buffers akin to KMEI buffer (0.5 μM) (Fig. II-11E and F, Table II-3) (12, 182, 190, 191). In contrast, the critical concentration of SpeMreB3 was estimated to be 18 times higher than that of SpeMreB5 (Fig. II-11E and G, Table II-3). In actin sedimentation assays, the actin concentration in

the supernatant fraction is consistent with the critical concentration (192). However, for SpeMreB3 and SpeMreB5, the concentrations in the supernatant fractions were not constant as seen in the linear-fit slope of the pellet amounts which was not 1 (Fig. II-11E).

Table II-3. Bulk critical concentrations of SpeMreBs polymerized with buffer S as measured by sedimentation assays. The values are indicated as the mean ± S.D. from five repeated measurements for SpeMreB5 WT polymerized with ATP and ATP-analogues and three repeated measurements for the others except for SpeMreB3 WT polymerized with AMPPNP or ADP and SpeMreB3 S176D whose critical concentrations could not be determined due to the low amounts of pellets. The row below the critical concentrations indicates the *p*-value of the critical concentration compared to the associated WT protein polymerized with ATP, as calculated by Student's *t*-test. *$p < 0.05$, **$p < 0.01$, and n.s., $p > 0.05$.

	SpeMreB3 WT ATP	SpeMreB3 WT AMPPNP	SpeMreB3 WT ADP	SpeMreB3 D147E ATP	SpeMreB3 K174T ATP	SpeMreB3 S176D ATP	SpeMreB3 K174T/S176D ATP
C_C (μM)	2.80 ± 0.34	N.D.	N.D.	1.26 ± 0.66	2.20 ± 0.50	N.D.	2.15 ± 0.43
t-test (v.s. WT ATP)	-	-	-	＊(0.02)	n.s. (0.16)	-	n.s. (0.11)

	SpeMreB5 WT ATP	SpeMreB5 WT AMPPNP	SpeMreB5 WT ADP	SpeMreB5 T160A ATP	SpeMreB5 T160K ATP	SpeMreB5 D162S ATP
C_C (μM)	0.14 ± 0.07	0.29 ± 0.11	0.39 ± 0.09	0.15 ± 0.15	≈ 0	0.07 ± 0.03
t-test (v.s. WT ATP)	-	＊(0.03)	＊＊(0.001)	n.s. (0.87)	-	n.s. (0.20)

Next, I determined the critical concentrations of SpeMreB3 and SpeMreB5 variants used in the P_i release assay. SpeMreB3 D147E showed a 2.2-fold lower critical concentration than WT SpeMreB3. SpeMreB3 S176D formed little amounts of pellets, thus the critical concentration could not be determined. The critical concentration of SpeMreB5 T160K was estimated to be ≈0 μM, because it formed higher amounts of precipitates than the WT. These results suggest that these mutations affect SpeMreB3 and SpeMreB5 polymerization activity. In contrast, the critical concentrations of the other variants (SpeMreB3 K174T, SpeMreB3 K174T/S176D, SpeMreB5 T160A, and SpeMreB5 D162S) were not significantly different from those of their respective WTs

(Fig. II-11E-G, Table II-3), suggesting that the filament amounts of these variants were

not significantly different from those of the corresponding WTs.
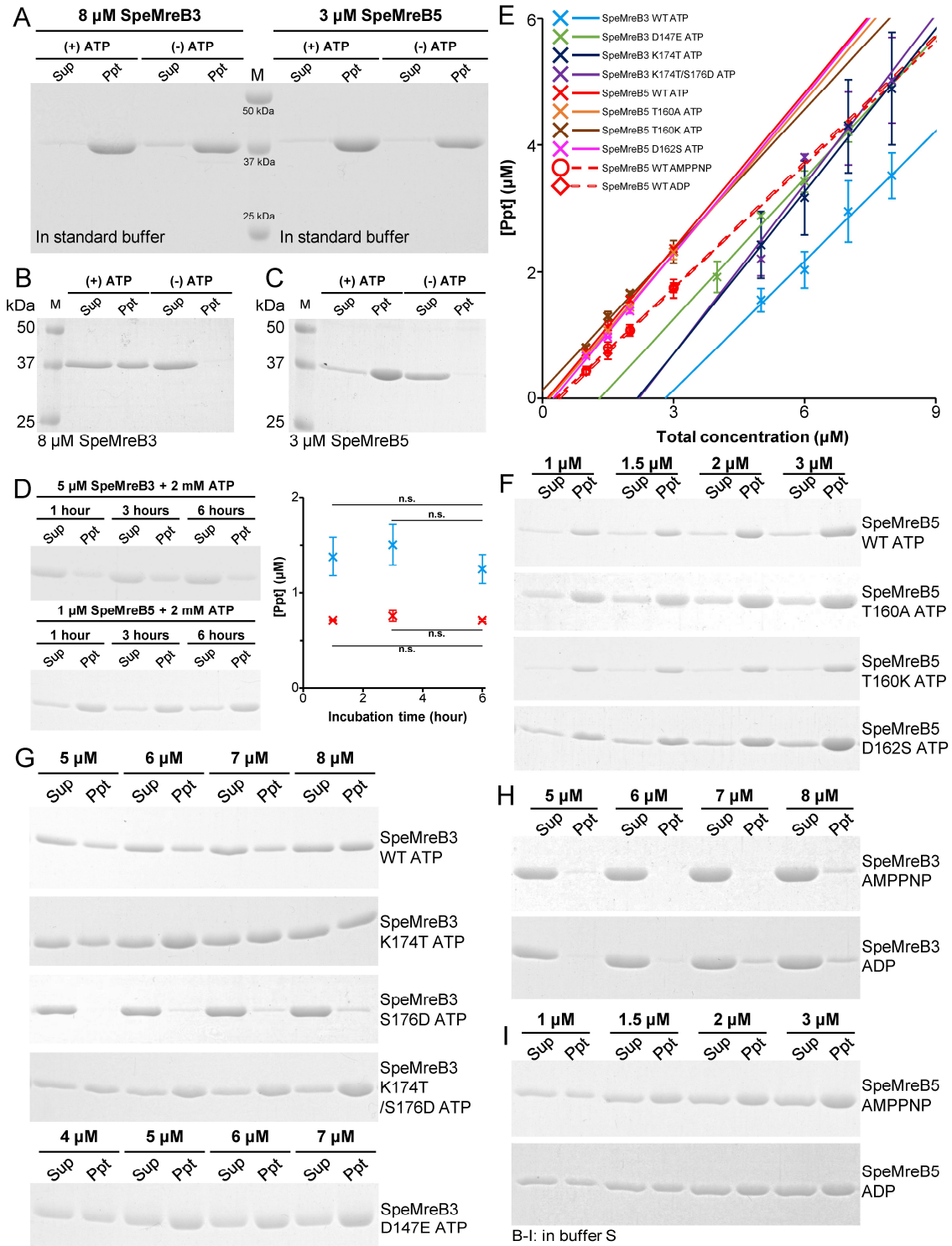
Figure II-11. SpeMreB sedimentation assays. Each SpeMreB was incubated with buffer S (20 mM

Tris-HCl pH 8.0, 1 M NaCl, 200 mM Arginine-HCl pH 8.0, 5 mM DTT, 2 mM MgCl$_2$, and

Figure II-11 (continued) 2 mM ATP) for 1 h after initiating polymerization and were ultracentrifuged at 436,000 × *g* for 120 min at 23°C, unless otherwise stated. Precipitates were resuspended with water equivalent to the sample amount. For SpeMreB3 and its variants, each fraction was diluted three times before the preparation of the sample for SDS-PAGE. Each fraction was loaded onto a 12.5% Laemmli gel and stained with Coomassie brilliant blue to quantify the protein concentration. Fractions derived from the same sample were loaded onto adjacent lanes, and the total concentration of the sample is indicated on the lanes. (**A**) Sedimentation assay of 8 μM SpeMreB3 (left side of lane M) and 3 μM SpeMreB5 (right side of lane M) polymerized for 3 h with standard buffer in the presence ((+) ATP) or absence ((−) ATP) of Mg-ATP. Protein size standards are shown in lane M, with the molecular masses of each band beside the band. (**B-C**) Sedimentation assay of (**B**) 8 μM SpeMreB3 and (**C**) 3 μM SpeMreB5 in the presence (left half lanes of each panel, (+) ATP) or absence (right half lanes of each panel, (−) ATP) of Mg-ATP. Protein size standards are visualized in lane M, with the molecular masses of each band on the left side. (**D**) (left) Sedimentation assays of 5 μM SpeMreB3 (top) and 1 μM SpeMreB5 (bottom) (the minimum concentrations to determine each critical concentration) dependent on polymerization time before centrifugation. The SpeMreBs polymerized for 1, 3, or 6 h were subjected to ultracentrifugation. (Right) The pellet concentrations were quantified from the gels on the left and plotted over the incubation time as cyan and red crosses for SpeMreB3 and SpeMreB5, respectively. Error bars indicate the S.D. from three repeated measurements. "n.s." indicates *p*-values greater than 0.05, as calculated by Student's *t*-tests. (**E**) Quantified precipitation amounts of sedimented SpeMreBs. The concentrations of the precipitated fractions were plotted over the total SpeMreB concentrations with linear fitting. Error bars indicate the S.D. from five repeated measurements for SpeMreB5 WT polymerized with ATP and ATP-analogues and three repeated measurements for the others. Critical concentrations were estimated as the x-intercept of each linear fit and are summarized in Table II-3. (**F-G**) Sedimentation assays for various concentrations of (**F**) SpeMreB5 and (**G**) SpeMreB3 WT and variants in the presence of 2 mM Mg-ATP. (**H-I**) Sedimentation assays for various concentrations of (**H**) SpeMreB3 and (**I**) SpeMreB5 polymerized with AMPPNP (top of each panel) or ADP (bottom of each panel) instead of ATP.

ATP hydrolysis enhances SpeMreB polymerization activity

To analyze the relationship between ATPase activity and polymerization dynamics, I determined the critical concentrations of SpeMreB3 and SpeMreB5 in the presence of Mg-ADP or Mg-AMPPNP. SpeMreB3 polymerized with AMPPNP or ADP pelleted less than those polymerized with ATP (Fig. II-11G and H). It was difficult to determine the

critical concentrations because the pellet amount was too low to be applied to linear fitting. The critical concentration of SpeMreB5 was lowest in the presence of ATP and was 2- and 3-fold higher in the presence of AMPPNP and ADP, respectively (Fig. II-11E and I, Table II-3). These results suggest that SpeMreB3 and SpeMreB5 in the pre-hydrolysis and post-P_i release states are unstable as filaments.

DISCUSSION

A model for SpeMreB polymerization dynamics

EM and sedimentation assays of SpeMreB3 and SpeMreB5 revealed the necessity of nucleotide binding for polymerization and unstable nucleotide states as filaments (Figs. II-2, II-3, II-11). Based on these results, I construct a working model for SpeMreB3 and SpeMreB5 polymerization dynamics (Fig. II-12). First, SpeMreBs bind ATP and polymerize into filaments, while the pre-hydrolysis state is unfavourable for them to remain as filaments (Fig. II-11E, H, and I, Table II-3). Polymerized SpeMreBs hydrolyze ATP. Then, SpeMreBs in the ADP-P_i state release P_i after a certain duration and are converted to a state with an increased critical concentration, the ADP-bound state, possibly leading to depolymerization. Eventually, the depolymerized SpeMreBs in the ADP state replace ADP with ATP and return to the initial state in the polymerization cycle.

This model is qualitatively applicable to SpeMreB3 and SpeMreB5, although their rate constants differ each other. While my Nf-SpeMreB3 crystal structure forms a protofilament (Fig. II-6A), I suppose that ATP binding is necessary to polymerize SpeMreB3, since filaments were not observed in the absence of nucleotides under solution conditions (Figs. II-3A and B, II-11B and C). Although some intra-protofilament interactions along the filament axis were observed in Nf-SpeMreB3, the interaction area

is smaller than that in SpeMreB3-AMPPNP (Figs. II-6B and C, II-7D). This difference is derived from domain closure upon AMPPNP binding (Fig. II-6D), suggesting that this conformational change is necessary to form filaments in solution. In contrast to my model, the ATP hydrolysis-deficient variants used in this study except for SpeMreB3 S176D showed lower or similar critical concentrations compared with the corresponding WTs (Fig. II-11E-G, Table II-3). This result may be caused by subtle differences in active site structures between the variants and the corresponding WTs, which can change the overall conformation, thereby leading to different polymerization ability (75, 126, 131).

The working model is qualitatively consistent with that of other actin superfamily proteins (8, 12, 13, 127, 128). However, the equilibrium balance of polymerization dynamics is likely uncommon. The critical concentration of actin polymerized with ADP is 18-fold higher than that of actin polymerized with ATP (8, 12). In contrast, the critical concentrations of SpeMreBs polymerized with ADP were only approximately two times higher than those polymerized with ATP (Fig. II-11E, H, and I, Table II-3), suggesting that SpeMreB3 and SpeMreB5 depolymerization is not substantially stimulated by P_i release compared to actin filaments. Structural differences between actin and SpeMreB may cause differences in their critical concentrations. In the actin filament, the D-loop in subdomain IB (subdomain 2 in actin nomenclature) forms a major intra-protofilament interaction that is attenuated upon P_i release (129). SpeMreB3 and SpeMreB5 lack a loop corresponding to the D-loop of actin, as well as MreB of walled bacteria, and their intra-protofilament interaction via subdomain IB is less than that of actin (Fig. II-6C) (37, 75, 85, 131). These findings suggest that SpeMreB subunit turnover rates are slower than those of actin. This may be a fundamental feature of MreB family proteins, because the critical concentration of TmMreB polymerized with ADP is approximately 2-fold higher

than that polymerized with ATP, as well as SpeMreB5 (182).
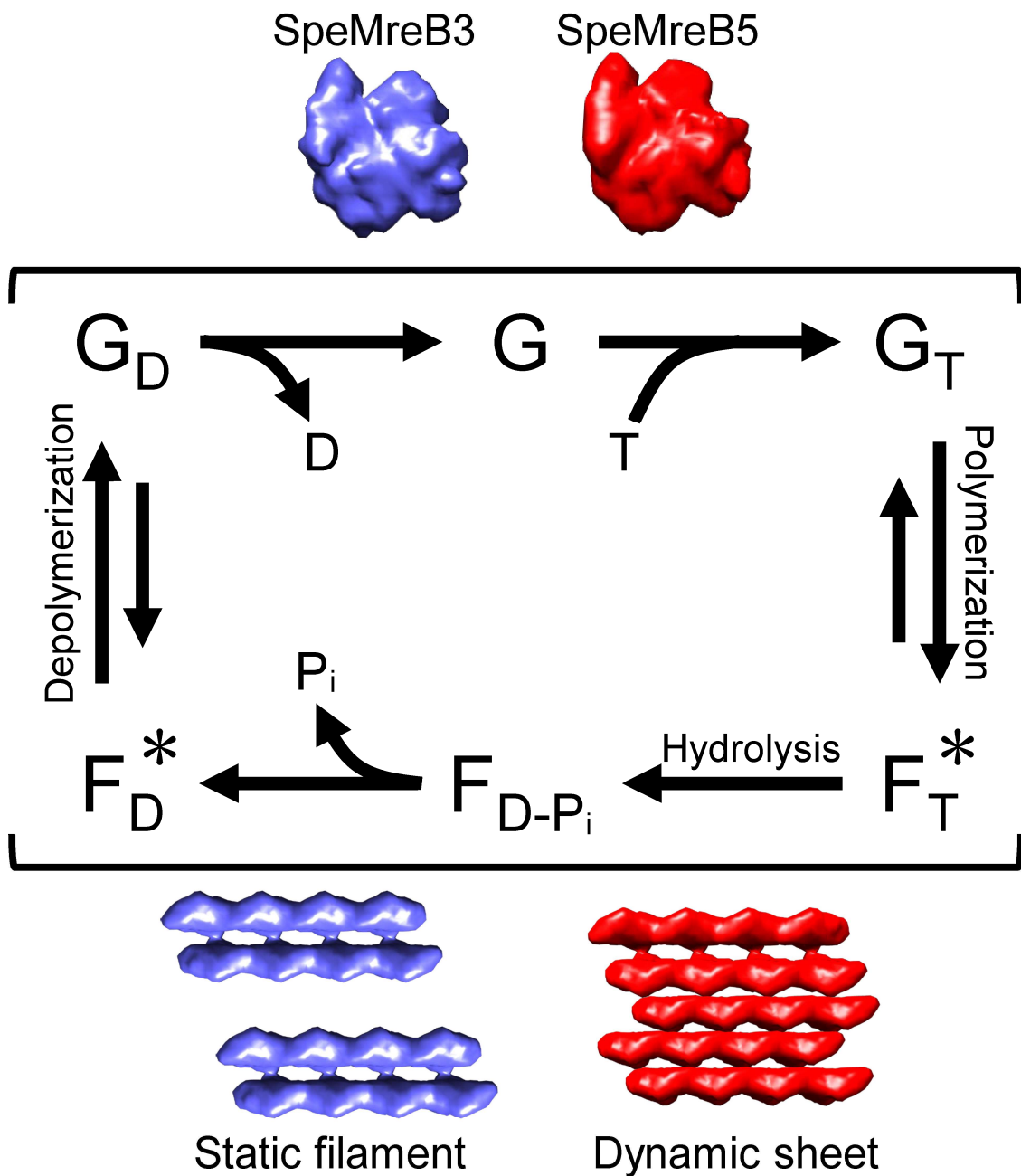
Figure II-12. Working model of SpeMreB polymerization. ATP and ADP are denoted as "T" and "D", respectively. The characters "G" and "F" indicate SpeMreBs in the monomeric and polymerized states, respectively, named analogous to actin states. Bound nucleotides on SpeMreBs are indicated as subscripts. In the filamentous states, the pre-hydrolysis and post-P_i release states, which showed high critical concentrations are indicated with asterisks. The schematic structures of monomeric and polymerized SpeMreB3 (cyan) and SpeMreB5 (red) are indicated beside the corresponding positions on the polymerization cycles with the filament characters.

ATP hydrolysis mechanism of MreB family proteins

My P_i release assays for SpeMreB3 and SpeMreB5 identified two players in ATPase activity — the threonine–acidic residue pair and the conserved glutamate corresponding to E140 in CcMreB (Fig. II-9A-F). These residues form a hydrogen-bonding network with a putative nucleophilic water molecule in the CcMreB structure (Fig. II-9D), suggesting that these residues play a role in ATP hydrolysis. E140 and T167 in CcMreB align the nucleophilic water into an appropriate position for ATP hydrolysis (75). Previously, it was not clear which residue plays a role in proton elimination from the water molecule, which is a necessary step for ATP hydrolysis. Based on my findings, I propose a hypothesis for the role of active-site residues in ATP hydrolysis using CcMreB as a model (Fig. II-9H). E169 eliminates the proton of the T167 side chain hydroxy group to activate this residue as an acidic catalyst for proton elimination from nucleophilic water. E140 adjusts the position of the nucleophilic water to be suitable to attack the γ-P_i of ATP. This reaction mechanism is similar to that proposed for skeletal actin, where Q137 (corresponding to E140 in CcMreB) is responsible for positioning nucleophilic water, while the water molecule (corresponding to the hydroxy group of T167 in CcMreB) interacting with D154 and H161 (corresponding to E169 in CcMreB) is responsible for the proton elimination from nucleophilic water (Fig. II-9I) (130). The amino acid motif "E ⋯ T - X - [DE]" is mostly conserved in MreB family proteins, except for SMreB3 (Fig. II-9G), suggesting that the ATP hydrolysis mechanism proposed here is conserved in most MreB family proteins.

Proposed role of SpeMreB3 and SpeMreB5 on *Spiroplasma* swimming

A previous study of *S. poulsonii* MreBs using a heterologous expression system

suggested that SMreB3 and SMreB5 play distinct roles in the cell (116). My results show that SpeMreB3 and SpeMreB5 polymerize into different filamentous structures with distinct ATPase activities and critical concentrations (Figs. II-2, II-9, II-11). These differences in polymerization characteristics may be related to the differences in the roles of SpeMreB3 and SpeMreB5. SMreB5 is likely an actuator that changes the conformation of the internal ribbon structure to drive the cell (116). My EM observations revealed that SpeMreB5 forms sheet structures with two patterns of inter-protofilament interactions (Figs. II-2E, II-4A). These interactions were not observed in the walled-bacterial MreBs. Because of these distinct interaction patterns, the sheets exhibit both parallel and antiparallel alignment of the two protofilaments. Parallel alignment can lead to anisotropy in the overall sheet structure which meets the requirement of directional movement of *Spiroplasma* swimming. Interestingly, I did not find a sheet structure with an interior antiparallel filament, although both sides of the filament should be structurally identical. This suggests that SpeMreB5 has a mechanism that leads to the structural anisotropy of the sheet. One possible explanation is that the growth of parallel protofilaments may change the conformation of the free side of the antiparallel filament to reduce the affinity of the parallel protofilament. Another possibility is that the binding rate of a new protofilament may be much faster on the parallel protofilament than on the free side of the antiparallel pair. SMreB3 likely anchors SMreB1 and/or SMreB4 filaments to the membrane to form a fixed structure (116). This role does not require filament polarity. SpeMreB3 forms a double-stranded filament with possible antiparallel polarity (Fig. II-4B-D), which is consistent with this requirement.

SpeMreB3 exhibits low ATPase activity (Fig. II-9A-C). To the best of my knowledge, this is one of the lowest activities of the actin superfamily proteins (Table II-2) (131, 177,

183, 184, 186-189). The amino acid residues responsible for low ATPase activity were conserved in SMreB3 (Figs. I-3, II-9G left lower). These findings suggest that low ATPase activity is involved in SpeMreB3 function. Since subunit turnover requires the completion of the ATPase cycle (Fig. II-12), low ATPase activity leads to slow subunit turnover, suggesting that the SpeMreB3 filament is stable and may stably anchor the SpeMreB1 and/or SpeMreB4 filaments onto the membrane. This is consistent with a previous study that showed that *S. poulsonii* MreB3 forms static filaments in a heterologous expression system (116).

Effect of SpeMreB3 methylation on polymerization

Lysine residues were methylated to obtain SpeMreB3 crystals suitable for structural determination (Fig. II-5A and B). Similar to unmethylated filaments, methylated SpeMreB3 polymerized into double-stranded filaments (Fig. II-5C). The P_i release rate of methylated SpeMreB3 was also low (Fig. II-5D). However, in sedimentation assays using 8 μM methylated SpeMreB3, pellets were not detected (Fig. II-5E), indicating that polymerization activity is attenuated by methylation. One reason may be that methylation inhibits the lysine residue-mediated interactions involved in filament formation. My crystal structure of the SpeMreB3-AMPPNP complex showed that K70, which is involved in intra-protofilament interactions, is di-methylated (Fig. II-6C). In methylated SpeMreB3, this interaction may be disturbed in solution, most likely because of a decrease in the degree of freedom of the interaction. In the SpeMreB3-AMPPNP complex, K174 is also di-methylated. I cannot rule out the possibility that this methylation changes the position of the residue, thus preventing interaction with nucleophilic water (Fig. II-9F) and slowing the ATP hydrolysis rate, as suggested by the decreased pellet amount in

the sedimentation assay (Fig. II-11B, G, and H). However, this methylation is unlikely to affect the above discussion on ATP hydrolysis because the P_i release rate was not changed by introducing the single K174T mutation (Fig. II-9A and B).

CONCLUSIONS

In this study, I clarified the distinct features of SpeMreB3 and SpeMreB5, which likely play different roles in *Spiroplasma* swimming (116). SpeMreB3 polymerizes into a double-stranded filament, whereas SpeMreB5 forms asymmetric sheet structures (Fig. II-2). The ATPase and polymerization activities of SpeMreB5 were higher than those of SpeMreB3 (Figs. II-9, II-11). The low ATPase activity of SpeMreB3 was caused by the lack of the core amino acid motif "E ⋯ T - X - [DE]," which is conserved in the catalytic center of most MreB family proteins (Figs. I-3, II-9G). These results indicate that *Spiroplasma* has diversified SMreB characteristics to acquire unique swimming motility. My results suggest two features presumably common to MreB family proteins: the ATP hydrolysis mechanism including a proton elimination step from the nucleophilic water molecule (Fig. II-9H), and the coupling of ATPase activity and polymerization dynamics (Fig. II-12). These findings will shed light on the chemistry and relationship between polymerization and the cellular functions of MreB family proteins.

MATERIALS AND METHODS

SpeMreB cloning and expression

The DNA sequences of SpeMreB1 to SpeMreB5 (111) were codon-optimized for *E. coli* expression and were individually synthesised by fusion with pUC57 (GenScript, Piscataway, NJ). The DNA fragments encoding the SpeMreBs were excised using NdeI

and BamHI restriction enzymes and inserted into pET-15b (Novagen, Madison, WI) or pCold-15b, which was constructed from pCold I (Takara Bio Inc., Kusatsu, Japan) by replacing the histidine tag and proteinase digestion site sequences with that of pET-15b. Each construct was transformed into *E. coli* BL21 (DE3) and C43 (DE3) cells. *E. coli* carrying the constructed plasmid was grown overnight in LB medium in the presence of 50 μg/mL ampicillin at 37°C. The culture was then diluted with fresh medium and incubated at 37°C. When the OD_{600} value reached 0.4–0.6, IPTG was added to a final concentration of 1 mM and the cultures were incubated for 24 h at 15°C. Cells were harvested, washed twice with PBS (10 mM Na_2HPO_4, 2 mM NaH_2PO_4, 3 mM KCl, and 137 mM NaCl), and stored at –80°C until further use.

SpeMreB purification

The WT and its variants of SpeMreB3 were purified by fusion with a 6× histidine tag at the N-terminus as follows. Cell pellets harvested from 1-L cultures were resuspended in 20–40 mL buffer A (50 mM Tris-HCl pH 8.0 at 25°C, 300 mM NaCl, and 50 mM imidazole-HCl pH 8.0 at 25°C) and sonicated with a probe sonicator (Nissei, Ultrasonic Homogenizer). The cell lysate was then centrifuged (100,000 × *g* at 4°C for 30 min). The supernatant was loaded onto a HisTrap HP column (Cytiva, Wauwatosa, WI, USA), washed with 10 column volumes of buffer A, and eluted with 13 mL of arranged buffer A containing 230 mM imidazole-HCl pH 8.0 at 25°C. The eluted SpeMreBs were further purified using a HiLoad 26/600 Superdex 200 pg column (Cytiva) at 4°C equilibrated with buffer B (20 mM Tris-HCl pH 8.0 at 25°C and 300 mM NaCl). For SpeMreB5 and its variants, the centrifugation strength was decreased to 12,000 × *g*. For purification of SpeMreB3 for the crystallization experiments, buffer C (10 mM Tris-HCl

pH 8.0 at 25°C, and 150 mM NaCl) was used for gel filtration with a HiLoad 26/600 Superdex 200 pg column instead of buffer B. Protein concentrations were determined from the absorbance at 280 nm measured using NanoDrop One (Thermo Fisher Scientific) with the following absorption coefficients: 0.474 $(mg/mL)^{-1}$ cm^{-1} for SpeMreB3 and its variants and 0.578 $(mg/mL)^{-1}$ cm^{-1} for SpeMreB5 and its variants.

SpeMreB3 methylation

SpeMreB3 eluted from Ni^{2+}-NTA chromatography was subjected to HiPrep 26/10 Desalting column (Cytiva) equilibrated with buffer D (50 mM HEPES-NaOH pH 7.5 at 25°C and 250 mM NaCl) or dialysed with buffer D to replace the buffer. To methylate lysine residues in SpeMreB3, DMAB (Merck) and formaldehyde (Merck) were added at final concentrations of 20 and 40 mM, respectively (178, 179), and the sample was incubated for 2 h at 4°C. The methylated sample was desalted with a HiPrep 26/10 Desalting column equilibrated with buffer D to remove excess DMAB and formaldehyde, concentrated to less than 13 mL using an Amicon Ultra 10 K dialysis cassette (Merck), and subjected to gel filtration chromatography on a HiLoad 26/600 Superdex 200 pg column. The column was equilibrated with buffer B at 4°C. The methylation ratio of methylated SpeMreB3 reached 96.5 ± 2.2%, as confirmed by MALDI-TOF mass spectrometry (Fig. II-5B). To prepare methylated SpeMreB3 for crystallization, the following three steps were modified from the method described above: (I) after Ni^{2+}-NTA affinity chromatography, the mixture of the sample and 100 units of thrombin (Cytiva) was dialysed overnight at 4°C in buffer D to cleave the histidine tag from SpeMreB3. (II) after 2 h of incubation with 20 mM DMAB and 40 mM formaldehyde, two incubation steps were added before the removal of excess DMAB and formaldehyde. DMAB and

formaldehyde were added at concentrations of 40 mM and 80 mM, respectively, and the sample was incubated for 2 h at 4°C. Then, an additional 10 mM DMAB (total 50 mM) was added and the sample was incubated overnight at 4°C. In this procedure, although the terminal 7–13 residues of methylated SpeMreB3 were cleaved, and small amounts of degraded products appeared even after the final purification step, methylated SpeMreB3 was successfully crystallized. (III) Buffer C was used for gel filtration on a HiLoad 26/600 Superdex 200 pg column instead of buffer B.

SpeMreB polymerization

To prepare samples for EM observations and to measure P_i release rates, SpeMreBs were polymerized in standard buffer (20 mM Tris-HCl pH 7.5 at 25°C, 100 mM KCl, 5 mM DTT, 2 mM $MgCl_2$, and 2 mM ATP). For sedimentation assays, SpeMreBs were polymerized in buffer S (20 mM Tris-HCl pH 8.0 at 25°C, 1 M NaCl, 200 mM L-arginine-HCl pH 8.0, 5 mM DTT, 2 mM $MgCl_2$, and 2 mM ATP). Prior to polymerization, the SpeMreB buffer was replaced from buffer B to the desired buffer in the absence of DTT, $MgCl_2$, and ATP by overnight dialysis at 4°C with a buffer volume 50–100 times higher than that of the sample solution. Monomeric SpeMreBs with a concentration lower than the desired concentration were concentrated using Amicon Ultra 10 K cassettes. The samples were centrifuged to remove aggregates. Then, DTT, $MgCl_2$, and ATP were added to initiate polymerization. All polymerization reactions were performed at room temperature (approximately 25°C).

Electron microscopy

The SpeMreBs were polymerized for 3 h, which was long enough to obtain steady-

state samples for the other MreBs (177, 182, 186, 191, 193, 194). A sample (4 µL) was placed onto a 400-mesh copper grid coated with carbon for 1 min at room temperature, washed with 10 µL of water, stained for 45 s with 2% (w/v) uranyl acetate, air-dried, and observed under a JEOL JEM-1010 transmission electron microscope (Tokyo, Japan) at 80 kV equipped with a FastScan-F214T charge-coupled device camera (TVIPS, Gauting, Germany). To obtain SpeMreB3 and SpeMreB5 images for 2D averaging, 10 µM SpeMreB3 and 5 µM SpeMreB5 polymerized with standard buffer were diluted to 3 µM immediately before sample placement onto a grid. For image averaging, SpeMreB images were automatically selected as helical objects and were segmented in a box of 128 × 128 pixels with 90% overlap using RELION ver. 3.1 (176). The images were processed using the estimation of the contrast transfer function and reference-free 2D class averaging using RELION ver. 3.1 or 4.0 (176). For the image averaging of SpeMreB3, 13,077 particles were extracted from 51 field images and classified into 50 classes, yielding a class composed of 2,874 particles as the final particle set. For SpeMreB5, 117,740 particles were extracted from 70 field images and classified into 200 classes, yielding initial classes of images with two, three, four, and five protofilaments. The particle sets in each class (2,104, 4,155, 5,201, and 3,992 particles for the classes of images with two, three, four, and five protofilaments, respectively) were individually subjected to 2D classification into 50 classes, excluding some particles from the initial particle sets that interfered with image averaging. This step was repeated two more times with class numbers of 25 and 3 at each classification step. Three sets of SpeMreB5 images with two, three, four, and five protofilaments were obtained by averaging 1,593, 2,211, 1,191, and 928 particles, respectively (Figs. II-2D and E, II-4A). The subunit repeats in the 2D averaged images were estimated as the distances between the minimal values of the

grayscale profiles quantified using ImageJ (National Institutes of Health; http://rsb.info.nih.gov/ij/). To determine each subunit axis of the 2D averaged images, the images were subjected to black and white inversion and binarized with a grey value threshold of 75 (for the SpeMreB3 and SpeMreB5 filaments) and 68 (for the SpeMreB5 five-stranded sheet), in which the densities for intra- and inter-protofilament interaction regions were excluded using ImageJ. Each separated subunit density was subjected to elliptical fitting using ImageJ and the major axis was defined as the subunit axis.

Crystallization and structural determination

Crystallization conditions were screened using the sitting-drop vapour-diffusion technique with the following screening kits: Wizard Classic I–II (Rigaku Reagents, Inc., Bainbidge Island, USA), Wizard Cryo I–II (Rigaku Reagents, Inc.), PEG/Ion Screen I–II (Hampton Research, Alison Viejo, USA), Crystal Screen I–II (Hampton Research), SaltRx I–II (Hampton Research), and PEG/Ion 400 (Hampton Research), at 4°C and 20°C. Nf-SpeMreB3 crystals used for X-ray data collection were grown at 4°C from drops prepared by mixing 0.5 μL of protein solution (5 mg/mL) in buffer C with an equivalent volume of reservoir solution containing 100 mM MES-NaOH pH 6.0, 20% (w/v) PEG-8000, and 200 mM calcium acetate. The crystals belonged to the space group $P2_1$ with unit cell dimensions of $a = 52.4$, $b = 68.1$, $c = 54.6$ Å, and $\beta = 91.7°$. The SpeMreB3-AMPPNP complex crystals used for X-ray data collection were obtained at 20°C from drops prepared by mixing 0.5 μL of protein solution (5 mg/mL) in buffer C containing 5 mM $MgCl_2$ and 5 mM Li_4AMPPNP with an equivalent volume of reservoir solution containing 100 mM acetate-NaOH pH 4.6, 30% (w/v) PEG-4000, and 200 mM ammonium acetate. The crystals belonged to the space group $P2_1$ with unit cell

dimensions of $a = 50.3$, $b = 56.3$, $c = 120.5$ Å, and $\beta = 90.6°$.

X-ray diffraction data were measured at 100 K at synchrotron beamlines BL41XU and BL45XU at SPring-8 (Harima, Japan) with the approval of the Japan Synchrotron Radiation Research Institute (JASRI) (proposal nos. 2018A2567, 2018B2567, 2019A2550, and 2019B2550). The crystals were cryoprotected by soaking in a 1:9 mixture of glycerol and reservoir. The diffraction data were processed using MOSFLM (195) and scaled using Aimless software (196). The initial phase was determined by MR with Phaser software (197) using a previously-reported CcMreB structure (PDB ID: 4CZL). An atomic model of Nf-SpeMreB3 (P17–L344) was constructed using Coot (198) and refined using Phenix (197). The refined Nf-SpeMreB3 structure was used for MR of the SpeMreB3-AMPPNP complex. An atomic model of the SpeMreB3-AMPPNP complex (Mol-A: P17–N348; Mol-B: P18–E347) was built using Coot (198) and was refined using Phenix (197). The data collection and refinement statistics are summarized in Table II-1.

Analyses of domain angles

The SpeMreB3 structures were divided into four subdomains according to the definition of MreBs in walled-bacteria. The first 17 residues (M1–P17) and the last 8 residues (I345–K352) were excluded from subdomain IA because the corresponding regions were not modeled in SpeMreB3-AMPPNP Mol-B and Nf-SpeMreB3, respectively. The centroid of each subdomain was calculated from the backbone atoms without mass-weighting on each atom using UCSF Chimera ver. 1.13.1 (168). The centroids were used for calculations of the domain opening and dihedral angles using UCSF Chimera ver. 1.13.1 (Fig. II-7B) (168).

P$_i$ release assays

P$_i$ release was measured using EnzChek kits (Thermo Fisher Scientific), in which the P$_i$ concentration was traced by the absorbance of the reaction product between P$_i$ and MESG, a molecular probe for P$_i$, at 360 nm (A$_{360}$) (181-185). Reactions were initiated by adding a mixture of MgCl$_2$, ATP, and MESG to SpeMreBs in standard buffer without Mg-ATP. The A$_{360}$ values of SpeMreBs without MESG and control buffer containing MESG were subtracted from those measured for SpeMreBs with MESG. Data were collected using a Varioskan Flash spectrophotometer (Thermo Scientific), which had an initial measurement delay of approximately 1 min.

Sedimentation assays

SpeMreBs with a volume of 200 μL were polymerized for 1–6 h and were centrifuged (100,000 rpm at 23°C for 120 min) in a TLA-100 rotor (Beckman Coulter). The pellet was resuspended in 200 μL water. The supernatant and pellet fractions were subjected to electrophoresis on a 12.5% Laemmli gel and stained with Coomassie Brilliant Blue R-250 to determine the concentration of each fraction. The SpeMreB band intensities were quantified using the ImageJ software. The concentrations of the supernatant and pellet fractions were estimated as the products of the total SpeMreB concentration and the ratio of each fraction to the sum of the supernatant and pellet fractions. The critical concentration was determined as the x-intercept of a linear fit with the precipitate amounts at the polymerization steady state over the total SpeMreB concentration.

Chapter 3: Assembly properties of SpeMreB5

ABSTRACT

Bacterial actin MreB forms filaments in which the unit of the structure is an antiparallel double strand. The wall-less helical bacterium *Spiroplasma* has five MreB homologs (SMreB1–5) a part of which is composed of an intra-cellular ribbon for driving its swimming motility. The interactions of each ribbon component are unclear, although these are clues for understanding *Spiroplasma* swimming. Here, I investigated the assembly properties of *Spiroplasma eriocheiris* MreB5 (SpeMreB5), which forms sheets and is a component protein essential for the *Spiroplasma* swimming. My EM observations revealed that sheet formation was inhibited under acidic conditions and paracrystal structures were formed under acidic and neutral conditions with low ionic strength. Solution assays found four properties of paracrystals as follows: (I) their formation followed sheet formation, (II) electrostatic interactions were required for their formation, (III) the positively charged and unstructured C-terminal region contributed to the nucleation of their formation, and (IV) their formation required Mg^{2+} at neutral pH but was inhibited by divalent cations under acidic conditions. During these studies, I found two aggregation modes of SpeMreB5 with distinct responses to ATP. These properties will shed light on SpeMreB5 functions at the molecular level.

INTRODUCTION

In chapter 2, I described the sheet formation of SpeMreB5 (Figs. II-2E, II-4A). Sheet formation was found for MreBs of various species (75, 177, 186, 193, 194, 199). In contrast, many proteins in the actin superfamily form bundles under several *in vitro* conditions (63). Actin forms bundles in the presence of 10–50 mM divalent cations. The

bundle formation depends on the negatively charged nature of the actin filament surfaces (63, 125, 200, 201). Several walled-bacterial MreBs have been reported to form bundles, the formation efficiencies of which depend on pH, ionic strength, and divalent cations (177, 186, 193, 194, 199). Analyses of the sheet and bundle formation processes of cytoskeletal proteins are important for understanding their behaviors at the molecular level. However, the limited experimental conditions for MreB hamper the full understanding of its sheet- and bundle-formation processes. Moreover, bundle formation of SMreBs is poorly characterized.

In this chapter, I analyzed assembly properties of SpeMreB5. My EM observations under various conditions revealed paracrystal formation of SpeMreB5. Light scattering and sedimentation assays revealed the molecular properties of paracrystals. These findings provide clues to understand the properties of SpeMreB5. During these studies, I found two aggregation modes of SpeMreB5 that showed distinct responses to ATP.


RESULTS

SpeMreB5 forms double-stranded filaments and paracrystals other than sheets

I first polymerized 10 μM SpeMreB5 by adding 2 mM Mg-ATP under three different pH conditions (50 mM CH_3COOH-KOH pH 4.9, HEPES-KOH pH 7.0, and CHES-KOH pH 9.4 as representatives of acidic, neutral, and basic conditions, respectively) over a range of KCl concentrations (50, 200, and 400 mM) and observed using negative-staining EM. At pH 7 and 200 mM KCl, SpeMreB5 formed sheet structures as observed in chapter 2 (Figs. II-2B, III-1C). Sheets were also formed at pH 7 with 400 mM KCl and at pH 9 (Fig. III-1B and C). Among the nine tested conditions, sheets were the dominant structures for polymerized SpeMreB5 (squares in Fig. III-1C). Interestingly, I found

filamentous structures other than sheets under several conditions. At pH 5 and 7 with 50 mM KCl, SpeMreB5 formed paracrystal structures, in which protofilaments were packed in an identical orientation (Fig. III-1A and C). The paracrystal lengths reached several micrometers. These structures have also been reported in TmMreB and EcMreB as bundles (177, 194). In contrast, at pH 5 with 200 and 400 mM KCl, SpeMreB5 formed double-stranded filaments, which has also been reported in SpeMreB3 and CcMreB (Figs. II-2A, III-1C) (75). I also performed the same experiments on SpeMreB3. At pH 7, SpeMreB3 formed double-stranded filaments regardless of the KCl concentration, as reported in chapter 2 (Fig. III-1D). However, filamentous structures were not observed under the other pH conditions, which did not allow me to validate the bundle formation of SpeMreB3.

I also performed negative-staining EM in the absence of Mg-ATP, as a control. SpeMreB5 at pH 5 and 9, and SpeMreB3 did not form filamentous structures. Interestingly, SpeMreB5 at pH 7 polymerized even in the absence of Mg-ATP (Figs. III-1E and F). The experimental conditions of this chapter differ from those of chapter 2 in protein concentrations (5 μM in this chapter and 10 μM in chapter 2) and buffers (20 mM Tris-HCl pH 7.5 in this chapter and 50 mM HEPES-KOH pH 7.0 in chapter 2). In the HEPES buffer, 5 μM SpeMreB5 formed filamentous structures in the presence of Mg-ATP (Fig. III-1G) but not in the absence of Mg-ATP (Fig. III-1H). These results indicate that ATP promotes the SpeMreB5 polymerization. In contrast, 10 μM SpeMreB5 polymerized in the absence of Mg-ATP in the Tris buffer used in chapter 2 (Fig. III-1I). These results indicate that SpeMreB5 with a concentration of approximately 10 μM or more polymerizes even without nucleotides at neutral pH.
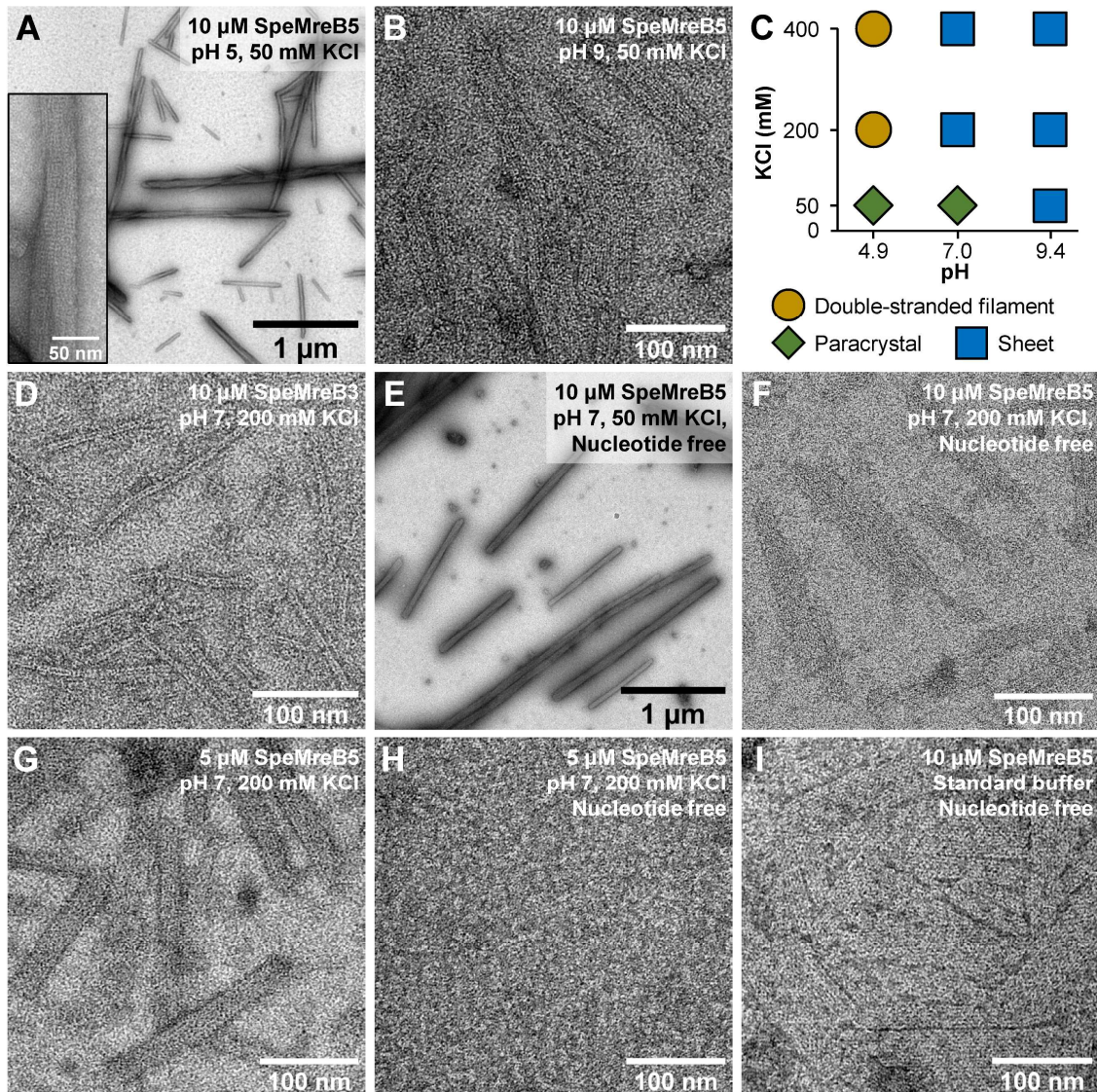
Figure III-1. pH and ionic strength dependence of assembled SpeMreB5 structure. (**A-B**) Negative-staining EM images of 10 μM SpeMreB5 polymerized in the presence of 2 mM Mg-ATP with 50 mM KCl at pH (**A**) 5 and (**B**) 9. A magnified image of the paracrystal is shown in the inset of panel A. (**C**) A phase diagram of SpeMreB5 filament structures at 10 μM protein concentration over a range of pH and KCl concentration. Filament structures in each condition are indicated by shapes with different colors as follows; double-stranded filament (ocher circle), sheet (blue square), and paracrystal (green diamond). (**D**) Negative-staining EM images of 10 μM SpeMreB3 polymerized with 2 mM Mg-ATP at pH 7 with 200 mM KCl. (**E-H**) Negative-staining EM image of (**E-F**) 10 and (**G-H**) 5 μM SpeMreB5 polymerized in the (**E-F** and **H**) absence or (**G**) presence of nucleotides at pH 7 with (**E**) 50 and (**F-H**) 200 mM KCl. (**I**) Negative-staining EM image of 10 μM SpeMreB5 polymerized in the absence of Mg-ATP in standard buffer used in chapter 2 (composed of 20 mM Tris-HCl pH 7.5 and 100 mM KCl).

Surface potential maps of SpeMreB5 over the range of pH

To discuss the atomic basis of sheet and paracrystal formation, I calculated the surface potential maps of a crystal structure of the SMreB5 protofilament reported previously (SciMreB5 (PDB ID: 7BVY) (85), which is 87.5% identical to SpeMreB5), at pH 5, 7, and 9 (Fig. III-2A-C). In the following sentences, I call the inter-protofilament interaction surface for the antiparallel filament formation "back" and the opposite side "front." I also fitted these structures to the antiparallel double-stranded filament of CcMreB (PDB ID: 4CZJ), in which the crystal structure was reported (75), to validate potential maps of filament sides (Fig. III-2D-I). I call the side for subdomains IA and IB "membrane side" and the opposite side "cytosolic side" as MreBs bind with the membrane via either two consecutive hydrophobic residues, an N-terminal amphipathic helix, and/or a positively charged C-terminal tail all at subdomain IA (122, 131). For comparison, I calculated the surface potential maps of SpeMreB3 (Fig. II-6A), TmMreB (PDB ID: 1JCG), and EcMreB (modeled by AlphaFold2 (156)) at pH 7, where EM studies have been conducted (Fig. III-2J-L) (63, 177, 186). Of note, I excluded the membrane sides from the following discussion, as the terminal regions of SciMreB5 and SpeMreB3 with around 20 residues that should occupy the membrane sides were not visualized (Fig. III-2G-J).
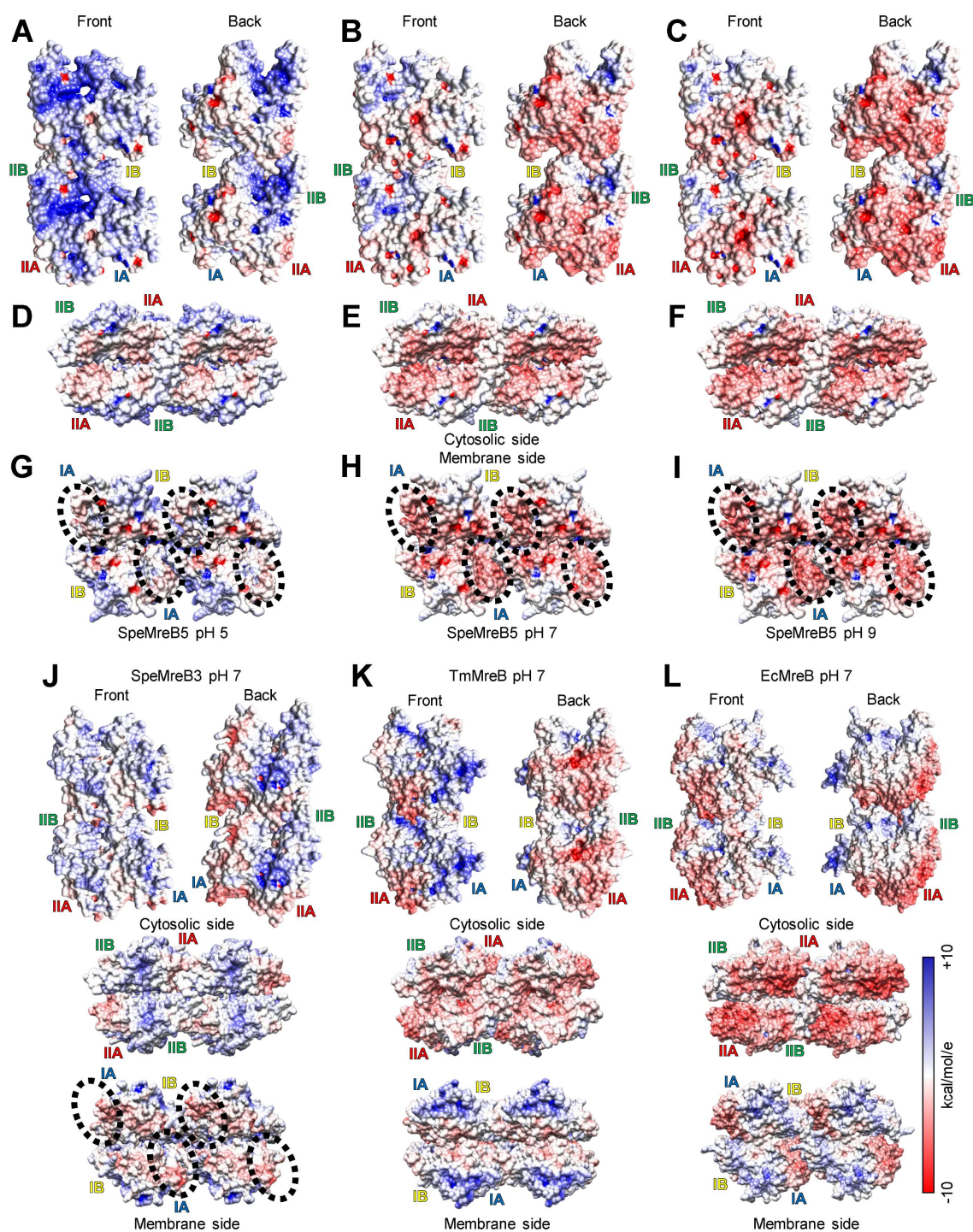
Figure III-2. Surface potential maps of MreB (proto)filaments. The coulombic electrostatic potential is indicated by a color gradient from blue (10 kcal/mol/e) to red (−10 kcal/mol/e); namely blue, white, and red regions indicate positively charged, uncharged, and negatively charged regions, respectively. The structural models of double-stranded filaments were created by fitting four MreB molecules to each subunit of a double-stranded filament structure of CcMreB (PDB ID: 4CZJ). The positions of facing subdomains are labeled for the left side subunits.

Figure III-2 (continued) (**A-C**) Potential maps of the protofilaments with two subunits of SciMreB5-AMPPNP complex (PDB ID: 7BVY) at pH (**A**) 5, (**B**) 7, and (**C**) 9. The four subdomains are labeled for the lower subunits in the protofilament. (**D-F**) Potential maps on the cytosolic side of the double-stranded filament model of SciMreB5-AMPPNP at pH (**D**) 5, (**E**) 7, and (**F**) 9. (**G-I**) Surface potential maps on the membrane side of double-stranded filament model of SciMreB5-AMPPNP at pH (**G**) 5, (**H**) 7, and (**I**) 9. A circle with dashed line indicates the region where is possibly occupied by the positively charged C-terminus, which is not visualized in the reference structure. (**J-L**) Surface potential maps of protofilaments and double-stranded filament models of (**J**) SpeMreB3 (Fig. II-6A), (**K**) TmMreB (PDB ID: 1JCG), and (**L**) EcMreB (the monomer was modeled by AlphaFold2 (156)) at pH 7. The protofilament model of EcMreB (front and back side views) were created by fitting two EcMreB molecules to each subunit of a protofilament of a CcMreB double-stranded filament. A circle with dashed line on the membrane side of SpeMreB3 double-stranded filament model indicates the region where is possibly occupied by the amphipathic N-terminal helix, which is not visualized in the reference structure. Lysine residues of SpeMreB3 are di-methylated (Figs. II-5A and B), weakening the positive charge of lysine residues. Therefore, the di-methylated lysine residues were replaced with the most probable rotamers of lysine in Dunbrank's rotamer library (202).

The SciMreB5 protofilament at pH 5 was mostly positively charged on the back and front sides, whereas its cytosolic region was surrounded by weakly negatively charged regions (Fig. III-2A and D). The potential map of the SciMreB5 protofilament at pH 7 differed strikingly from that at pH 5 (Fig. III-2A, B, D, and E). The back side of the protofilament was mostly surrounded by negatively charged regions. The charge on the front side remained weakly positive, whereas that of the subdomain IIA moiety became weakly negative (Fig. III-2B). The negative charges on the cytosolic regions at pH 7 were stronger than those at pH 5 (Fig. III-2D and E). These features are common to the potential maps of TmMreB and EcMreB protofilaments (Fig. III-2K and L) and different from that of the SpeMreB3 protofilament, in which the front and back sides and the cytosolic region are positively charged (Fig. III-2J). The overall surface charge distribution of the SciMreB5 protofilament at pH 9 was slightly different from that at pH 7 (Fig. III-2B, C, E, and F). A difference in the distributions is found at the subdomain IIA moiety of the

front side, in which the negatively charged region becomes wider at pH 9 than at pH 7. Moreover, the negative charge on the overall structure became slightly stronger. These differences in the surface potential probably caused the various sheet and paracrystal formation modes of SpeMreB5 under various solution conditions (Fig. III-1C).
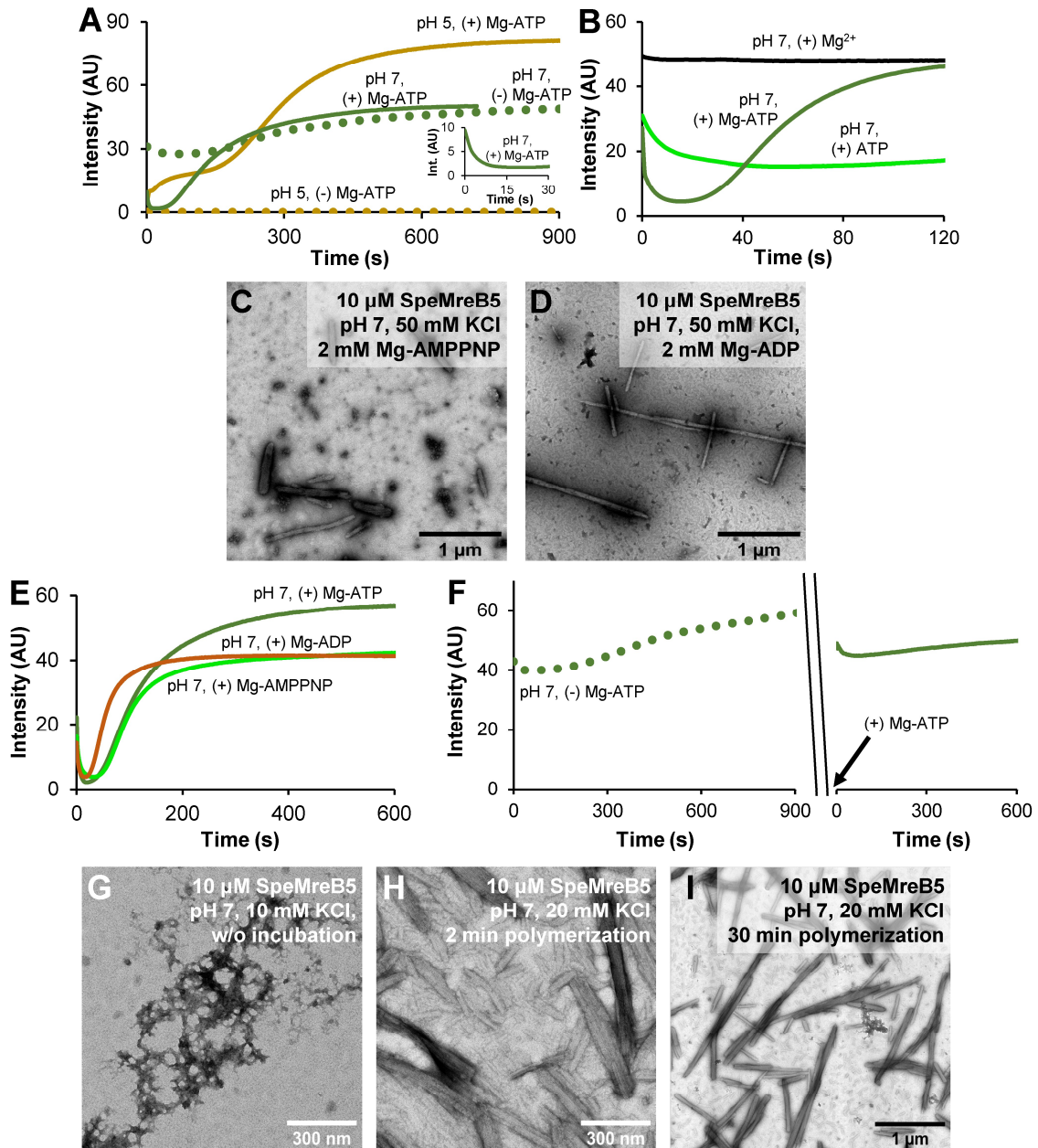
The paracrystal formation of SpeMreB5 at a neutral pH follows by disaggregation and sheet formation

To clarify the assembly dynamics of the SpeMreB5 higher-order structures observed under EM (diamonds and squares in Fig. III-1C), I performed static light scattering assays. The samples were kept on ice at 5X concentrations prior to the experiments and were measured for the scattering of 650 nm light toward 90° at 25°C. In time-course measurements, I set the KCl concentration to 10 mM to promote assembly dynamics (Fig. III-3A and B). At pH 7, the scattering pattern sequentially transitioned through three states over time after the addition of 2 mM Mg-ATP as follows: (I) the scattering intensity dropped to the background level in the first ~10 s, (II) the low scattering intensity continued for ~30 s as the "lag phase," and (III) the scattering intensity dramatically increased and reached the plateau in approximately 10 min (Fig. III-3A green solid line). The scattering profile at pH 5 did not have a lag phase and did not show an initial drop in intensity, unlike that at pH 7. Instead, the scattering profile showed two phases, in which the first phase reached a plateau in approximately 2 min and the second phase reached it in approximately 15 min (Fig. III-3A yellow solid line). The plateau intensity of the second phase at pH 5 was 1.6 times higher than that at pH 7, probably reflecting the difference in the heterogeneity of higher-order structures including sheets and paracrystals (also described in Figs. III-7 and III-8). The scattering intensity at pH 5 did

not increase in the absence of Mg-ATP (Fig. III-3A yellow dotted line), indicating that Mg-ATP was a factor that increased the intensity. The initial scattering intensity at pH 7 is high in the absence of Mg-ATP. The intensity was stable for approximately 3 min and gradually increased to the plateau level in the presence of Mg-ATP in approximately 15 min (Fig. III-3A green dotted line).

To clarify the mechanism of the initial intensity drop by adding Mg-ATP at pH 7, I separately added 2 mM Mg^{2+} or 2 mM ATP to SpeMreB5 at pH 7 and observed the initial dynamics. The scattering intensity remained high after the addition of Mg^{2+} (Fig. III-3B black line). The addition of ATP decreased the initial scattering intensity, although it did not reach the background level (Fig. III-3B light green line) unlike the addition of Mg-ATP (Fig. III-3B dark green line). These results indicate that both Mg^{2+} and ATP were related to the initial intensity drop of SpeMreB5 at pH 7. In a later paragraph, I will show that the initial intensity drop was also induced by Ca^{2+} and ATP (Fig. III-8D). To further characterize the decrease in the initial intensity, I performed the following two experiments. First, I measured the assembly dynamics of SpeMreB5 at pH 7 in the presence of 2 mM Mg-AMPPNP or Mg-ADP, instead of Mg-ATP. SpeMreB5 formed paracrystals at pH 7 in the presence of the ATP analogs (Fig. III-3C and D). The plateau intensities with Mg-AMPPNP or Mg-ADP were approximately 70% compared with those with Mg-ATP, suggesting that paracrystal formation was promoted by ATP hydrolysis. Despite this difference, the scattering profiles composed of three sequential states were common among the three different nucleotide conditions (Fig. III-3E). Second, I added 2 mM Mg-ATP to the sample that had already reached a plateau in the absence of nucleotides, that is, Mg-ATP addition after SpeMreB5 paracrystal formation in the absence of nucleotides (Fig. III-1E). The scattering intensity remained unchanged, even

after the addition of Mg-ATP (Fig. III-3F), indicating that the decrease in the initial intensity of SpeMreB5 at pH 7 was caused by disruption of higher-order structures other than paracrystals by interactions with nucleotides rather than hydrolysis.

Figure III-3. Dynamics of paracrystal formation and aggregation disassembly. For time-course light scattering, representative traces from three repeated assays for each condition are shown. (**A**) Assembly dynamics of 10 μM SpeMreB5 at pH 5 (ocher) and 7 (green) with 10 mM KCl measured by light scattering. The measurement in the presence of 2 mM Mg-ATP and in the absence of nucleotides are plotted as solid and dotted lines, respectively. The spectrum of the first 30 s at pH 7

Figure III-3 (continued) with Mg-ATP is highlighted in the inset. (**B**) Assembly dynamics of 10 μM SpeMreB5 in the presence of 2 mM MgCl$_2$ (black), 2 mM ATP (light green), and 2 mM Mg-ATP (green) at pH 7 with 10 mM KCl measured by light scattering. (**C-D**) Negative-staining EM images of 10 μM SpeMreB5 polymerized with 2 mM (**C**) Mg-AMPPNP and (**D**) Mg-ADP at pH 7 with 50 mM KCl. (**E**) Assembly dynamics of 10 μM SpeMreB5 in the presence of 2 mM Mg-ATP (dark green), Mg-AMPPNP (light green), and Mg-ADP (orange) at pH 7 with 10 mM KCl. (**F**) Dynamics of SpeMreB5 paracrystal formed in the absence of nucleotides. SpeMreB5 with 10 μM concentration was pre-assembled in the absence of nucleotides at pH 7 with 10 mM KCl (dotted line on the left graph). After a several min, 2 mM Mg-ATP was added, and time-course light scattering was measured (solid line in the right graph). (**G-I**) Negative-staining EM image of 10 μM SpeMreB5 (**G**) without incubation and (**H-I**) polymerized for (**H**) 2 and (**I**) 30 min at pH 7 in the presence of 2 mM Mg-ATP. KCl concentration in panel G was same as that in panels A and B (10 mM), while that in panels H and I was 20 mM to obtain the assembly dynamics with a longer lag phase than that with 10 mM KCl.

To clarify the structural basis of the assembly dynamics, I observed SpeMreB5 in each state of the assembly dynamics. Prior to polymerization at pH 7, aggregating structures of sub-micrometer sizes were observed instead of filamentous structures (Fig. III-3G). To visualize the lag phase in the presence of Mg-ATP at pH 7, I increased the KCl concentration to 20 mM, in which the lag phase was approximately 2 min longer than that at 10 mM KCl for ease of handling. SpeMreB5 in the lag phase formed sheet structures together with thin and small paracrystals of sub-micrometer lengths (Fig. III-3H). Paracrystal structures were formed at the plateau, as was the first EM observation in this chapter (Figs. III-1C, III-3I). These results indicate that SpeMreB5 under neutral pH changes the assembly state in the order of aggregates, sheets, and paracrystals.

I also observed the first plateau at pH 5 in the presence of Mg-ATP using EM. However, sheet structures were not observed, unlike at pH 7. This result is consistent with the first EM observations in this chapter, where sheets were not observed at pH 5 (Fig. III-1C).

SpeMreB5 paracrystal formation require electrostatic interactions

My light scattering assays were able to measure SpeMreB5 paracrystal formation (Fig. III-3A). Using these assays, I studied the formation mechanism of SpeMreB5 paracrystals. I first measured the steady-state intensities of SpeMreB5 paracrystals over a range of ionic strengths (Fig. III-4A). At both pH 5 and pH 7, the scattering intensities were mostly constant at 10–30 mM KCl, decreased as the KCl concentration increased at 40–70 mM KCl, and became less than the detection limit at 80 mM KCl or higher. Next, I performed disassembly assays in which pre-formed paracrystals were disrupted by changes in the solution conditions (Fig. III-4B and C). The scattering intensity at both pH 5 and 7 decreased as the KCl concentration increased (Fig. III-4B), indicating that the paracrystals were disrupted by increasing ionic strength. I also performed disassembly assays by changing the pH. The scattering intensities remained unchanged after the pH was shifted to 6 or 7. However, when the pH was shifted to 8 or 9, the scattering intensities decreased to the background level within 2 min (Fig. III-4C). These results indicate that SpeMreB5 paracrystal formation requires electrostatic interactions.
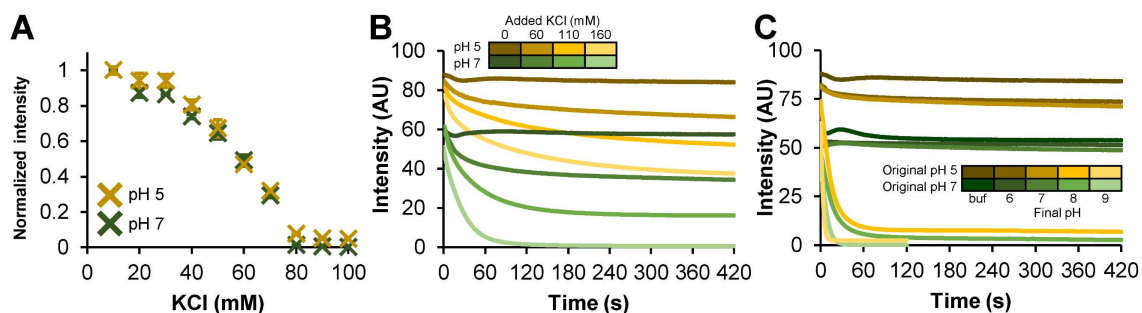
Figure III-4. Electrostatic interaction dependence of SpeMreB5 paracrystal. For time-course light scattering, representative traces from three repeated assays for each condition are shown. (**A**) Normalized steady-state light scattering of 10 μM SpeMreB5 polymerized in the presence of 2 mM Mg-ATP over the range of KCl concentration at pH 5 (ocher) and 7 (green). Bars indicate S.D. from three independent measurements. (**B-C**) Disassembly dynamics of SpeMreB5 paracrystals measured using light scattering. The paracrystal solutions were prepared by polymerizing 10 μM SpeMreB5 with 2 mM Mg-ATP in buffers of 10 mM CH₃COOH-KOH pH 4.9 (ocher scaled colors) and 10 mM

Figure III-4 (continued) HEPES-KOH pH 7.0 (green scaled colors) with 40 mM KCl. The measurements in which the buffer composition was unchanged are indicated with the thickest colored lines. (**B**) Disassembly was induced by increasing KCl concentration into 100 (second thickest colored line in each color scale), 150 (second thinnest colored), and 200 mM (thinnest colored). (**C**) Disassembly was induced by changing the buffer pH into 6 (second thickest colored line in each color scale), 7 (medium colored), 8 (second thinnest colored), and 9 (thinnest colored) by adding 50 mM MES-KOH pH 6.0, HEPES-KOH pH 7.0, HEPES-KOH pH 8.1, and CHES-KOH pH 9.4, respectively.

The positively charged C-terminal region of SpeMreB5 is contributed to the nucleation of paracrystals and the aggregation at a neutral pH

Each SMreB5 possesses a C-terminal unstructured region with a positive net charge (Fig. I-3) (85, 131). To investigate the effects of this region on paracrystal formation, I prepared two SpeMreB5 variants with truncations of 9 and 26 residues at the C-terminus (ΔC9 and ΔC26, respectively) (Fig. III-5A). SpeMreB5 ΔC9 is comparable to SciMreB5 ΔC10 used in a previous study (131), and SpeMreB5 ΔC26 is a variant in which all C-terminal residues outside the MreB folding domain are removed. ΔC9 was successfully purified. In contrast, ΔC26 did not bind to the Ni^{2+}-NTA affinity column, possibly due to non-specific binding between the 6×His-tag and the ΔC26 surface. Moreover, the solubility of ΔC9 at pH 5 was not high enough for polymerization experiments, although the solubility at pH 7 was sufficient. Therefore, I analyzed the paracrystal formation of the C-terminal-truncated variant of SpeMerB5 using ΔC9 at pH 7 by light scattering. The initial intensity of ΔC9 was the background level unlike WT (Figs. III-3A, III-5B), indicating that the initial aggregation of SpeMreB5 (Fig. III-3G), which caused the high initial intensity, was formed via the C-terminal region. ΔC9 in the presence of Mg-ATP assembled slower than that of WT and did not reach a plateau after 20 min (Fig. III-5B). However, the steady-state intensities of ΔC9 were slightly lower than those of WT over

the KCl concentrations (Fig. III-5C). To evaluate whether the slow assembly of ΔC9 was caused by the sheet assembly phase, I measured the critical concentration of ΔC9 by sedimentation assays. It was not significantly different from that of WT (Fig. III-6A, B, and E, Table III-1), suggesting that the truncation of C-terminal 9 residues did not affect the dynamics of polymerization and sheet formation. These results indicate that the C-terminal region of SpeMreB5 is involved in the nucleation step of paracrystal formation.

In the absence of Mg-ATP, the scattering intensity of ΔC9 increased immediately after initiating the measurement and plateaued at the same time scale as the WT in the absence of Mg-ATP. However, the plateau intensity of ΔC9 in the absence of Mg-ATP was half that of WT in the absence of Mg-ATP (Fig. III-5B). These results suggest three possibilities: (I) the reaction path of WT and ΔC9 in the absence of Mg-ATP is identical, (II) SpeMreB5 undergoes different reaction paths with and without nucleotides, and (III) paracrystal formation in the absence of Mg-ATP is promoted by the formation of the aggregation.
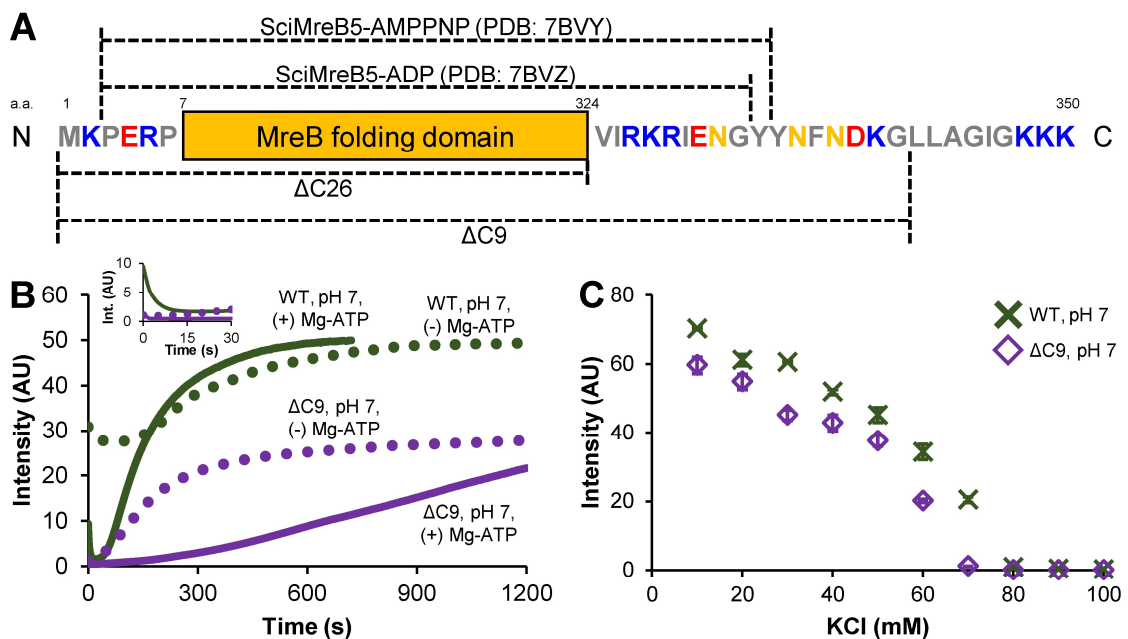
Figure III-5. Assembly dynamics of paracrystals by the C-terminus truncated variant of SpeMreB5. (**A**) Schematics of the SpeMreB5 sequence. The MreB folding domain is defined as the visible region in all the MreB crystal structures reported previously (Fig. II-6A) (37, 75, 85, 131) and invisible-flexible loops within them. The residues exterior of the MreB folding domain are shown with gray, orange, red, and blue colors for hydrophobic, non-polar-hydrophilic, acidic, and basic ones, respectively. The regions that are visible in the previously reported crystal structures of SciMreB5 (85, 131) and for SpeMreB5 ΔC9 and ΔC26 variants are indicated above and underneath the schematics, respectively. (**B**) Assembly dynamics of 10 μM SpeMreB5 WT (green, the same traces as those in Fig. III-3A) and ΔC9 variant (purple) at pH 7 with 10 mM KCl measured using light scattering. The measurement in the presence of 2 mM Mg-ATP and in the absence of nucleotides are plotted as solid and dotted lines, respectively. Representative traces from three repeated assays for each condition are shown in the graph. The spectra of the first 30 s are highlighted in the inset. (**C**) Steady-state light scattering of 10 μM SpeMreB5 WT (green) and ΔC9 (purple) polymerized in the presence of 2 mM Mg-ATP over the range of KCl concentration at pH 7. Bars indicate S.D. from three independent measurements.
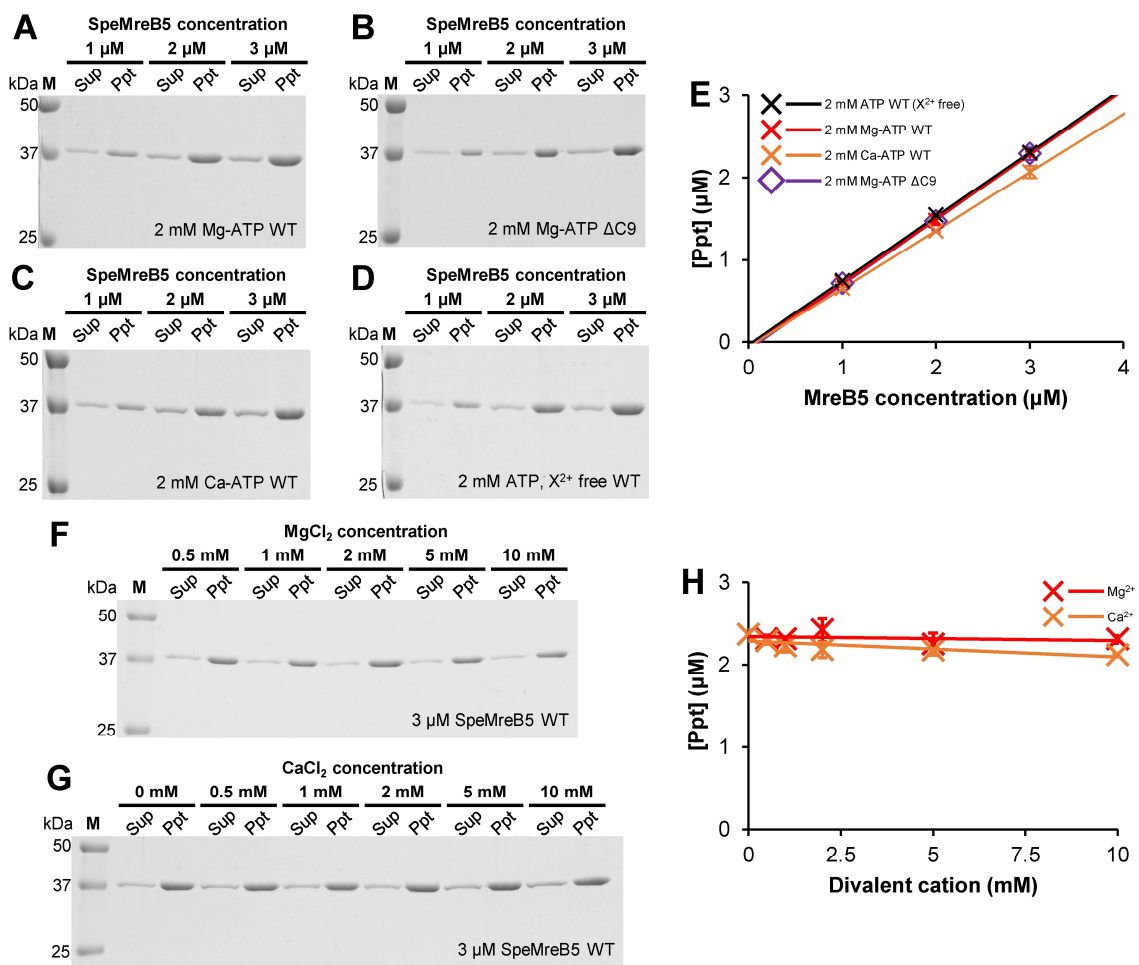
Figure III-6. Sedimentation assays of SpeMreB5. Each sample was incubated in the buffer S, centrifuged, and analyzed using SDS-PAGE, as described in chapter 2. All reactions were conducted in the presence of 2 mM ATP. For divalent cation-free conditions, 1 mM EDTA-NaOH pH 8.0 was added to avoid effects from contaminating amounts of multivalent cations. **(A-D)** Sedimentation assays of SpeMreB5 (**A** and **C-D**) WT and (**B**) ΔC9 polymerized with 2 mM (**A-B**) Mg-ATP, (**C**) Ca-ATP, and (**D**) ATP (divalent cations free) over the range of SpeMreB5 concentration. (**E**) Quantified precipitation amounts of sedimented SpeMreB5. Precipitated SpeMreB5 was resuspended in water equivalent amount to the sample, and the resulting concentrations were plotted over the total SpeMreB5 concentrations with linear fitting. Error bars indicate S.D. from three repeated measurements. Critical concentrations were estimated as the x-intercept of each linear fit and summarized in Table III-1. (**F-G**) Sedimentation assay of 3 μM SpeMreB5 over the range of (**F**) $MgCl_2$ and (**G**) $CaCl_2$ concentrations. (**H**) Quantified precipitation amounts of sedimented SpeMreB5. Precipitated SpeMreB5 was resuspended in water equivalent amount to the sample, and the resulting concentrations were plotted over the divalent cation concentrations with linear fitting. Error bars indicate S.D. from three repeated measurements.

Table III-1. Bulk critical concentrations of SpeMreB5 WT with varying divalent cation conditions and ΔC9 variant measured using sedimentation assays. The values are indicated as mean ± S.D. from three repeated measurements. The row below the critical concentrations indicates p-value with the critical concentration with 2 mM Mg-ATP supported by Student's t-test, showing that significances of critical concentration differences are not supported for all tested pairs.

	2 mM Mg-ATP WT	2 mM Mg-ATP ΔC9	2 mM Ca-ATP WT	2 mM ATP (X^{2+} free) WT
Cc of SpeMreB5 (μM)	0.09 ± 0.01	0.11 ± 0.04	0.09 ± 0.08	0.05 ± 0.03
p-value v.s. 2 mM Mg-ATP WT	—	0.45	0.95	0.07

Paracrystal formation of SpeMreB5 require Mg^{2+} at a neutral pH but are inhibited by divalent cations at an acidic pH

Previous studies have revealed that bundle formation of actin superfamily proteins requires divalent cations (63, 193, 199, 200). I then examined the requirement of divalent cations for SpeMreB5 polymerization and the formation of the higher-order structures. First, I performed sedimentation assays on SpeMreB5 under various divalent cation

conditions (Fig. III-6). The pellet amounts of SpeMreB5 were mostly constant over Mg^{2+} and Ca^{2+} concentrations (Fig. III-6F-H). The critical concentrations of SpeMreB5 were not significantly different among conditions in the presence of 2 mM ATP (divalent cation-free), Mg-ATP, and Ca-ATP (Fig. III-6A and C-E, Table III-1). These results indicate that SpeMreB5 does not require divalent cations for polymerization and sheet formation.

I also examined the effect of divalent cations on SpeMreB5 paracrystal formation. At pH 7 in the presence of 2 mM Ca-ATP, SpeMreB5 formed sheets, while the corresponding condition in the presence of Mg-ATP formed paracrystals (Figs. III-1C, III-7A). In contrast, paracrystals were formed at pH 5 in the presence of 2 mM Ca-ATP (Fig. III-7B) as well as in the presence of Mg-ATP (Fig. III-1A and C). In the divalent cation-free condition at pH 7, most of SpeMreB5 formed sheets (Fig. III-7C) and a few fractions formed paracrystals (Fig. III-7D). Surprisingly, under divalent cation-free conditions at pH 5, amorphous aggregates were observed instead of filamentous structures (Fig. III-7E).
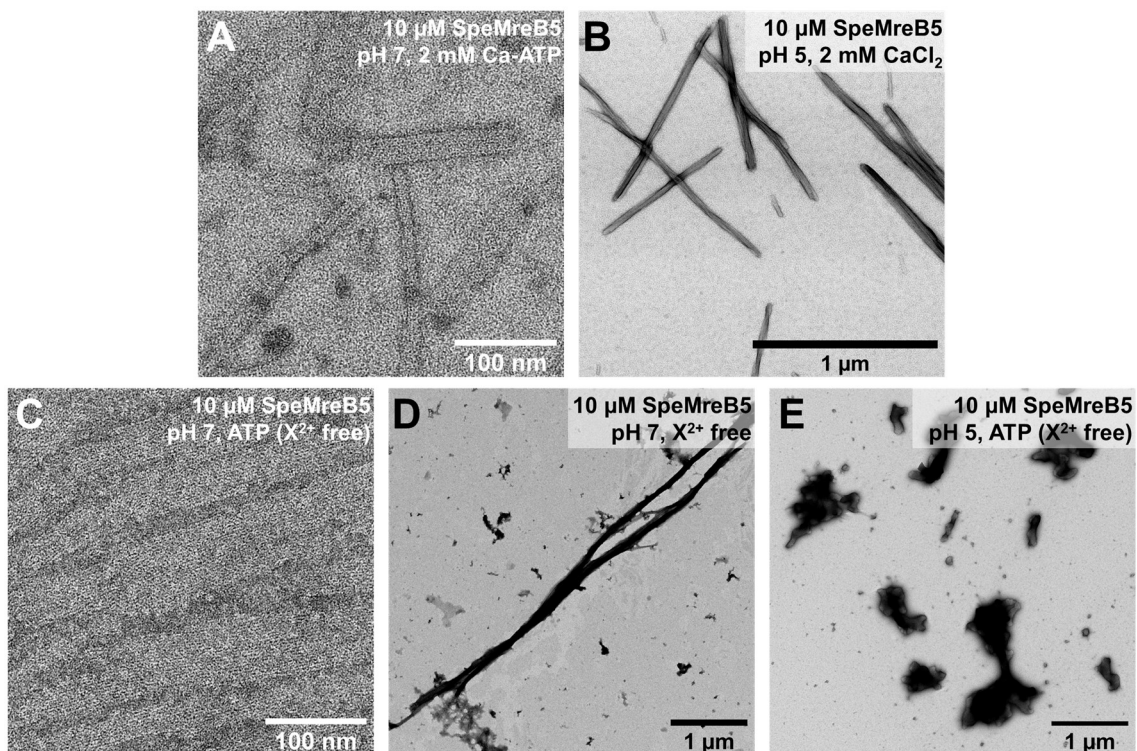
Figure III-7. Divalent cation dependence of SpeMreB5 higher-order structures. For divalent cation-free conditions, 1 mM EDTA-NaOH pH 8.0 was added to avoid effects from contaminating amounts of multivalent cations. (**A-E**) Negative-staining EM images of 10 μM SpeMreB5 incubated at pH (**A** and **C-D**) 7 and (**B** and **E**) 5 in the presence of (**A-B**) 2 mM Ca-ATP and (**C-E**) 2 mM ATP (divalent cation-free).

To clarify the effects of divalent cations on the assembly dynamics of paracrystals, I performed time-course measurements of SpeMreB5 paracrystal assembly (Fig. III-8A-D). In the divalent cation-free condition at pH 5, the scattering profile was single-phase and plateaued at the same time scale as the first phase in the presence of Mg^{2+}, indicating that the first phase of assembly dynamics at pH 5 reflects the aggregation of SpeMreB5 (Figs. III-7E, III-8A). The plateau intensities of both the first and second phases in the presence of Mg^{2+} at pH 5 decreased as Mg^{2+} concentration increased. In particular, the first phase was indistinguishable in the presence of 3 mM Mg^{2+} or higher. Moreover, the assembly rate of the second phase decreased in an Mg^{2+}-dependent manner (Fig. III-8A). Ca^{2+} showed similar effects to Mg^{2+} on SpeMreB5 paracrystal formation at pH 5, while its

inhibition efficiencies were less than that of Mg^{2+} (Fig. III-8B). These results indicate that SpeMreB5 paracrystal formation at pH 5 is inhibited by divalent cations.
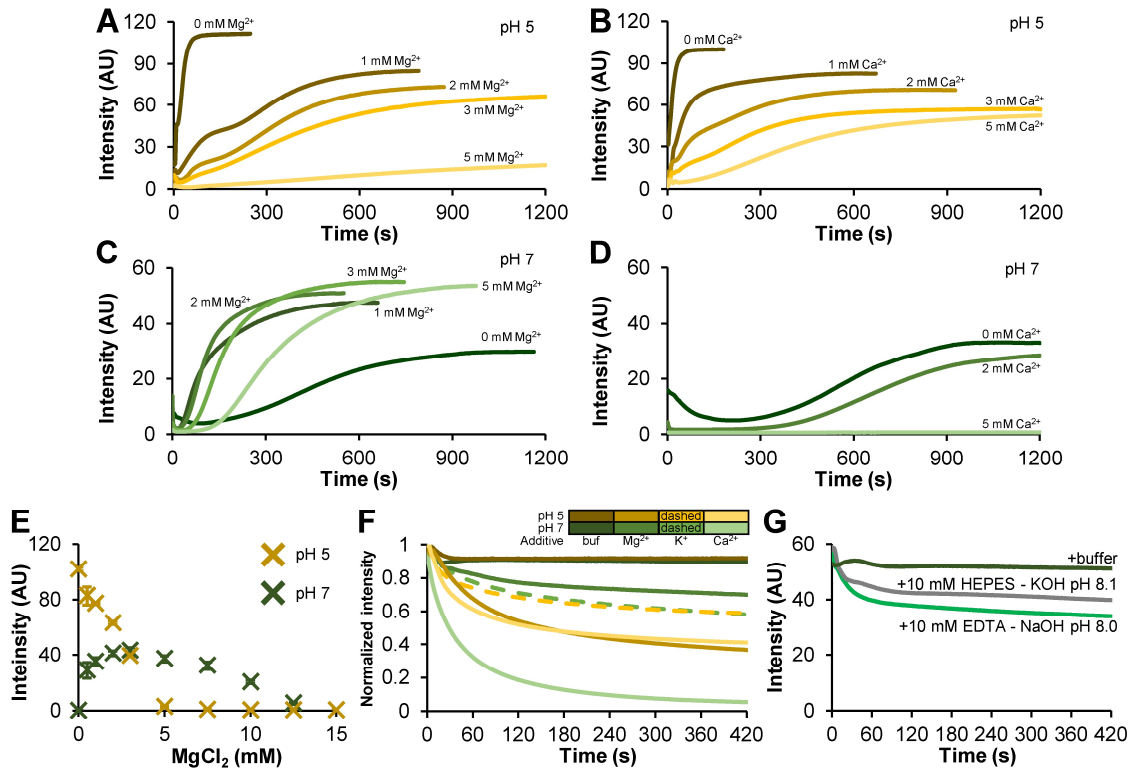
Figure III-8. Divalent cation dependence of SpeMreB5 polymerizations and higher-order structure formation. For time-course light scattering, representative traces from three repeated assays for each condition are shown. For divalent cation-free conditions, 1 mM EDTA-NaOH, pH 8.0 was added to avoid effects from contaminating amounts of multivalent cations. (**A-D**) Assembly dynamics of 10 μM SpeMreB5 dependent on (**A** and **C**) Mg^{2+} and (**B** and **D**) Ca^{2+} at pH (**A-B**) 5 and (**C-D**) 7 with 10 mM KCl measured using light scattering. The polymerization was initiated by adding 2 mM ATP with varying (**A** and **C**) $MgCl_2$ and (**B** and **D**) $CaCl_2$ concentrations as indicated in the color scales in the panels. (**E**) Steady-state light scattering of 10 μM SpeMreB5 polymerized with 2 mM ATP at pH 5 (ocher) and 7 (green) over the range of $MgCl_2$ concentration. KCl concentration was 50 mM constant. Bars indicate S.D. from three independent measurements. (**F**) Normalized light scattering traces of disassembly dynamics of SpeMreB5 paracrystals induced with divalent cations. The paracrystal solutions were prepared by polymerizing 10 μM SpeMreB5 in the presence of 2 mM Mg-ATP at pH 5 (ocher scaled colors) and 7 (green scaled colors) with 50 mM KCl. Disassembly was induced by adding 15 mM $MgCl_2$ (second thickest colored solid line), 15 mM $CaCl_2$ (thinnest colored solid line), and 60 mM KCl (second thinnest colored dashed line). Of note, the ionic strengths of these salts are identical assuming the same degree of dissociation (see Materials and Methods).

Figure III-8 (continued) The measurements in which the buffer condition was unchanged are indicated with the thickest colored solid lines. (**G**) Time-course light scattering measurements of SpeMreB5 paracrystals disassembly induced by 10 mM HEPES-KOH pH 8.1 (green) and EDTA-NaOH pH 8.0 (purple). The initial paracrystal solutions were prepared by polymerizing 10 μM SpeMreB5 in the presence of 2 mM Mg-ATP in 10 mM HEPES-KOH pH 7.0 with 40 mM KCl. The measurement in which the buffer composition was unchanged are indicated with the dark green line.

In contrast, the assembly dynamics of paracrystals at pH 7 showed puzzling Mg^{2+} dependence (Fig. III-8C). Under divalent cation-free conditions, the lag phase continued for approximately 3 min, and the intensity reached a plateau in approximately 20 min. Notably, as I performed the time-course measurements under a KCl concentration of 10 mM, which is lower than the EM observations, the scattering intensity was high even though there were few paracrystal structures under the EM observation (Fig. III-7C and D). In the presence of 1–3 mM Mg^{2+}, the times for the lag phase and reaching the plateau were five and two times shorter, respectively, and the plateau intensities were two times higher than those in the divalent cation-free condition. The plateau intensity in the presence of 5 mM Mg^{2+} was not different from those in the presence of 1–3 mM Mg^{2+}, whereas the lag phase became slightly longer (Fig. III-8C). I also examined the effects of Ca^{2+} on paracrystal assembly at pH 7. The initial intensity rapidly decreased with the addition of 2 mM Ca-ATP, indicating that the initial aggregation (Fig. III-3G) was also dissociated by Ca-ATP. Paracrystal assembly was suppressed in the presence of Ca^{2+}. In particular, the intensity did not substantially increase significantly within 20 min in the presence of 5 mM Ca^{2+} (Fig. III-8D). These results indicate that SpeMreB5 paracrystal formation at pH 7 requires Mg^{2+}.

Next, I measured steady-state intensities over a range of Mg^{2+} concentrations (Fig. III-8E). I set the KCl concentration to 50 mM for consistency with EM observations. At pH 5, the scattering intensities decreased in a Mg^{2+}-dependent manner and reached the

detection limit at Mg^{2+} concentrations of 5 mM or higher (Fig. III-8E yellow). Of note, this result may overrate the Mg^{2+} effects on paracrystals, as the scattering intensities are likely derived from both paracrystals (Fig. III-1A) and aggregations (Fig. III-7E). However, it is plausible that both aggregate and paracrystal formation were inhibited by Mg^{2+} at pH 5. At pH 7, the scattering intensities peaked in the presence of 3 mM Mg^{2+} and were nearly the background level at 0 and 15 mM Mg^{2+} (Fig. III-8E green), suggesting that the paracrystal formation efficiency at pH 7 is determined by the balance of the Mg^{2+} requirement for paracrystal formation and ionic strength effects. I also evaluated the paracrystal disassembly by increasing the concentration of divalent cations (Fig. III-8F). At pH 5, the decrease in the scattering intensity upon the addition of $MgCl_2$ and $CaCl_2$ was greater than that by KCl with the same ionic strength (when the degree of dissociation is assumed to be 1 for all salts) (yellow lines in Fig. III-8F). This phenomenon was common for $CaCl_2$ addition at pH 7. In contrast, the decrease in the scattering intensity by $MgCl_2$ at pH 7 was less than that by KCl (green lines in Fig. III-8F), consistent with the Mg^{2+} requirement of paracrystal formation at pH 7 (Fig. III-8E). Disassembly assays were also performed by adding EDTA (a chelating agent for multivalent cations) at pH 7. However, the decrease in the scattering intensity by EDTA was only slightly different from that of a buffer with a pH identical to that of the EDTA solution (Fig. III-8G), suggesting that Mg^{2+} was occluded in the paracrystals and was not accessed by the EDTA. Altogether, my results demonstrated that SpeMreB5 paracrystal formation at pH 5 is inhibited by divalent cations but that at pH 7 requires Mg^{2+}.

DISCUSSION

In this study, I investigated sheet and paracrystal formation of SpeMreB5 using EM

and bulk biochemical assays. The transitions of six states were observed in this study (Fig. III-9). I discuss the properties of each state and their possible roles in *Spiroplasma* swimming in some states.
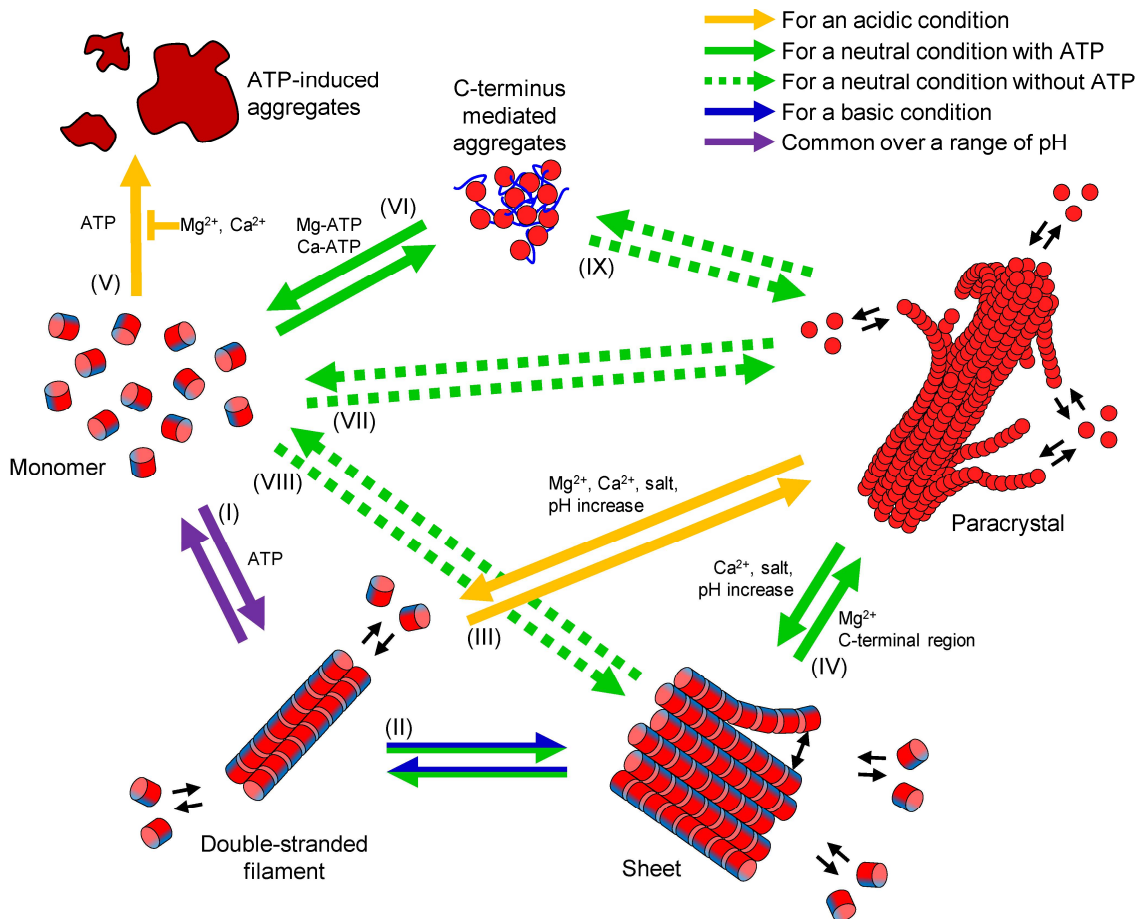
Figure III-9. Summary for SpeMreB5 polymerization. The relationship among the six states found in this study (monomer, double-stranded filament, sheet, paracrystal, C-terminus mediated aggregates disassembled by ATP, and aggregates induced by ATP) is suggested. An SpeMreB5 subunit is indicated by a red circle or a cylinder colored with red and blue. The positively charged-unstructured C-terminus is shown as a blue line for the state of the C-terminus mediated aggregate. Reactions specific for pH 5, 7, and 9 conditions in the presence of nucleotides are shown in solid lined arrows colored with orange, green, and blue, respectively. Reactions common over a range of pH is indicated using purple solid lined arrows. Reactions specific for conditions in the absence of nucleotides is shown in green dotted lined arrows. Factors that promote a reaction step are shown alongside each arrow. An inhibition factor against a reaction step is indicated by an arrow with a blunted end.

Polymerization and sheet formation

ATP was required for polymerization at a low SpeMreB5 concentration and at acidic and basic pH, although SpeMreB5 at pH 7 formed filamentous structures under nucleotide-free conditions (Fig. III-1E-I). These results indicate that ATP promotes SpeMreB5 polymerization (Fig. III-9-(I)), confirming my finding in chapter 2 that nucleotide binding induces polymerization of SpeMreB3 and SpeMreB5 (Fig. II-12). SpeMreB5 formed double-stranded filaments at acidic pH, and sheets at neutral and basic pH (Fig. III-1C). My study in chapter 2 revealed that SpeMreB5 sheets are composed of an antiparallel double-stranded filament at one edge and a parallel alignment of protofilaments (Figs. II-2E, II-4A). The minimum unit of SpeMreB5 filamentous structures was the double strand as well as the finding of a previous study (Fig. III-1C) (131), suggesting that sheet formation likely initiates from the double-stranded filaments (Fig. III-9-(II)). The SciMreB5 protofilament is mostly surrounded by positively charged regions on both the front and back sides at pH 5, while the back side is negatively charged at pH 7 and 9 (Fig. III-2A-C), suggesting that sheet formation at an acidic pH is inhibited by electrostatic repulsion between the front and back sides. This is consistent with the results, in which SpeMreB3 at pH 7 did not form sheets (Figs. II-2A, III-1D), and is surrounded by positively charged regions on both the front and back sides (Fig. III-2J). Considering the protofilament orientations within the sheets, the same protofilament side (Fig. III-2D-F) faces the cytosolic region. This alignment indicates that SpeMreB5 sheets face wide negatively charged surfaces in the cytoplasm when they bind to the membrane.

Paracrystal formation

SpeMreB5 formed paracrystals under low ionic strength conditions at acidic and

neutral pH (diamonds in Fig. III-1C). While this structure has not been observed in *Spiroplasma* cells (113, 114), it possibly reflects the properties of SpeMreB5 because there are clear differences in the tendency of paracrystal formation for SpeMreB3 and SpeMreB5 (Fig. III-1). The paracrystal formation mechanisms at acidic and neutral pH are likely different as the paracrystals showed distinct divalent cation dependences at these two pH conditions (Figs. III-7, III-8). Under acidic conditions, in which sheet formation was inhibited (Fig. III-1C), paracrystals likely grew from double-stranded filaments as nuclei (Fig. III-9-(III)). The surface potential map of the SciMreB5 protofilament at pH 5 showed that the cytosolic side was negatively charged, and the front side, which is exposed to the solvent when the double-stranded filaments are formed, was positively charged (Fig. III-2A and D), suggesting that these sides interact with each other to form paracrystals.

In contrast, SpeMreB5 formed sheets at a neutral pH prior to paracrystal formation in the presence of Mg-ATP (Fig. III-3H), suggesting that sheets work as nuclei of paracrystals (Fig. III-9-(IV)). As the steady-state intensities of ΔC9 were only slightly different from those of the WT (Fig. III-5C), the C-terminal region was probably not involved, and the negatively charged cytosolic region (Fig. III-2E) was likely involved in the interactions for paracrystal formation. The positively charged front side was the sole candidate interaction partner for the negatively charged cytosolic region (Fig. III-2B). The dependence of the front side on paracrystal formation is also supported by the inability of paracrystal formation at pH 9. The negatively charged region of the subdomain IIA moiety at pH 9 became wider than that at pH 7 (Fig. III-2B and C), possibly leading to electrostatic repulsion for the inhibition of paracrystal formation. Although the front side is exposed to the solvent when SpeMreB5 forms sheets, it is

unreasonable that the paracrystals are formed by sheet stacking, considering the tight packing of protofilaments within the paracrystals (Fig. III-1A). Instead, it is most plausible that single protofilaments elongate on negatively charged surfaces, such as the cytosolic side of the sheets, facing the front side to grow into paracrystals. This model is consistent with previous findings in which SpeMreB5 and SciMreB5 not only form inter-protofilament interactions for antiparallel double-stranded filaments (85, 131). Although the C-terminal unstructured region is expected not to be involved in interactions for paracrystal formation (Fig. III-5C), this region was involved in paracrystal nucleations (Fig. III-5B), suggesting that non-specific interactions via the C-terminal region increase the local concentration of SpeMreB5 around sheets and paracrystals to promote their assemblies. This idea is consistent with a previous study in which engineered proteins with flexible tubulin-binding regions on the outside of microtubules induced supra-structural formation such as microtubule doublets and branched microtubules (203). As the C-terminal region of SciMreB5 is involved in binding to the negatively charged *Spiroplasma* membrane (131), the paracrystal nucleation property may induce SMreB5 nucleation on the membrane. Paracrystal formation at a neutral pH required Mg^{2+} and was inhibited by Ca^{2+} (Figs. III-7A, III-8C-F), suggesting that SpeMreB5 has binding sites specific for Mg^{2+}. These regions probably localize on the surface of the SpeMreB5 protofilaments as those for the bundle formation of actin filaments are on its surface (200). Inhibition of bundle formation by Ca^{2+} has also been reported for EcMreB (177), suggesting that Mg^{2+} binding sites for paracrystal formation are negatively charged regions common between SpeMreB5 and EcMreB, such as the moieties of subdomains IIA and IIB on the back side of the protofilament. Paracrystal formation was inhibited by divalent cations at acidic pH (Fig. III-8A, B, E, and F), suggesting that the putative Mg^{2+}

binding regions at neutral pH turn their charges by pH shifts between 5 and 7.

Bundle formation dependent on divalent cations has also been reported for actin filaments. However, the optimal concentration of divalent cations for actin bundle formation is 10–50 mM which is approximately 10 times higher than the optimal concentration for SpeMreB5 paracrystal formation (1–5 mM) (Fig. III-8E) (200). Actin bundles are formed by bridging divalent cations with nine acidic residues (200), suggesting that electrostatic interactions are less involved in actin bundle formation than in SpeMreB5 paracrystal formation. This likely explains why actin bundles are resistant to the presence of high concentrations of divalent cations, which are high enough to disrupt SpeMreB5 paracrystals (Fig. III-8E). Moreover, actin filaments adopt a right-handed helix, which can restrict inter-filament interactions to form bundles. In contrast, the SpeMreB5 sheets are not helical (Fig. II-2B and E), suggesting that small amounts of Mg^{2+} will affect paracrystal formation as inter-protofilament interactions for paracrystal formation are unlikely to be restricted.

Aggregations induced and disassembled by ATP

I also found two SpeMreB5 aggregates that showed distinct responses to ATP (Figs. III-3G, III-7E). One was formed in the presence of ATP at acidic pH (Figs. III-7E, III-8A&B, III-9-(V)). This aggregation is surprising because, to the best of my knowledge, aggregations dependent on ATP have not been reported for the actin superfamily proteins. The other was formed at a neutral pH via the C-terminal region (Figs. III-3G, III-5B). This aggregation was disassembled by ATP, and the disassembly efficiency increased in the presence of divalent cations (Figs. III-3A and B, III-8D, III-9-(VI)). I cannot rule out the possibility that this aggregation was affected by the initial conditions of my

experiments (5X concentration prior to the assays, also described in Fig. III-3). However, disassembly of aggregates by ATP is intriguing because, to the best of my knowledge, a comparable phenomenon has not been reported for actin. Although only the nucleotide-binding pocket has been reported for the ATP-binding site of MreBs (Fig. II-6A) (37, 75, 85, 131), this site is unlikely to dominate the disaggregation phenomenon. ATP is not only known as a molecular unit of currency in life but is also reported as a hydrotrope of proteins (204). ATP as the hydrotrope binds non-specifically to the termini and loops of proteins (205). This is likely the case for SpeMreB5. The increased efficiency of SpeMreB5 disaggregation in the presence of divalent cations (Figs. III-3A and B, III-8D) suggests that ATP binding for disaggregation is promoted by the coordination of a divalent cation to the tri-phosphate group of ATP. In addition, the disaggregation by ATP of SpeMreB5 is likely distinct from that of the FUS protein, which does not rely on divalent cations (204).

SpeMreB5 polymerization in the absence of nucleotides

I found that SpeMreB5 polymerized in the absence of nucleotides at a neutral pH when the protein concentration was sufficiently high (Fig. III-1E-I). This finding is intriguing because the polymerization of SpeMreB5 and SciMreB5 is thought to require ATP (Fig. II-12) (85, 131). The lag phase of ΔC9 in the nucleotide-free condition was indistinguishable, unlike that in the presence of Mg-ATP (Fig. III-5B), suggesting that SpeMreB5 under nucleotide-free conditions undergoes reaction paths to directly shift the states from monomer to a structural state in the steady state (Fig. III-9-(VII) and (VIII)). SpeMreB5 WT, which forms aggregates disassembled by ATP (Fig. III-3G), in the absence of nucleotides reached a plateau intensity higher than that at ΔC9 without any

intensity drops (Fig. III-5B), suggesting the following two possibilities: there is a reaction path from the aggregates to paracrystals (Fig. III-9-(IX)) and the local concentration increase by the aggregation facilitates paracrystal formation in the absence of nucleotides.

CONCLUSIONS

In this chapter, I clarified the interactions in SpeMreB5 sheets and the formation mechanisms of paracrystals followed by sheet formation (Fig. III-9) by focusing on ionic strength and pH dependence (Fig. III-4), nucleation by the C-terminal region (Fig. III-5), and distinct divalent cation dependences (Figs. III-7, III-8). These findings will aid in the understanding of the molecular properties of SpeMreB5. In this study, I found two aggregation modes of SpeMreB5 with distinct responses to ATP (Figs. III-3G, III-7E). This finding also sheds light on the protein aggregation phenomena.

MATERIALS AND METHODS

SpeMreBs expression and purification

SpeMreB3 and SpeMreB5 and its ΔC variants were expressed and purified as described in chapter 2.

SpeMreB polymerization

The polymerization experiments were conducted as described in chapter 2. The detailed solution conditions are described in each figure legend. The conditions of pH 5, 7, and 9 were mediated by 50 mM CH_3COOH-KOH pH 4.9, HEPES-KOH pH 7.0, and CHES-KOH pH 9.4, respectively, unless otherwise stated.

EM observations and sedimentation assays

EM and sedimentation assays were conducted as described in chapter 2.

Estimation of surface potential map

The surface potential maps were calculated with the PDB2PQR (206, 207) server using the PARSE forcefield (208, 209) in conjunction with PROPKA (210-212) to assign the protonation state at the provided pH conditions (213). Calculations were performed for each subunit, excluding the bound ligands. For the calculation on SpeMreB3 (Fig. II-6A), in which lysine residues were di-methylated prior to crystallization (Fig. II-5A and B), the di-methylated lysine residues were replaced with the most probable rotamers of lysine in Dunbrank's rotamer library (202), because the positive charge of a di-methylated lysine residue is weaker than that of un-methylated lysine. The surface potentials were visualized using Chimera ver 1.13.1 (168) with a color gradient from −10 kcal/mol/e (red) to +10 kcal/mol/e (blue).

Static light scattering

Ninety-degree perpendicular light scattering experiments were carried out using FP-6200 (JASCO, Tokyo, Japan) in a single cuvette containing 60 μL sample solution at 25°C under the control of a temperature stabilizer. Both the excitation and emission wavelengths were set to 650 nm. For the time-course measurements, a sample with protein and buffer concentrations five times higher than the desired was kept on ice prior to the assay, diluted in a solution at room temperature to mediate the composition, and immediately applied to the measurements with a lag time of approximately 5 s due to manual mixing. For steady-state light scattering measurements, SpeMreB5 was

polymerized at room temperature for more than 2 h, which was sufficiently long to obtain

a steady-state. The baseline was set as the scattering intensity of water. Ionic strength (IS)

was estimated using the following equation:

$$IS = \frac{1}{2}\sum_i c_i z_i^2 \quad \cdots \quad (1)$$

where c_i and z_i are the concentration of the ion species and the charge of the ion,

respectively.

General Discussion

Properties of each SMreB class

In this doctoral thesis, I analyzed five classes of SMreBs by *in silico* and *in vitro* methods. All SMreBs are classified into a distinct clade from the radiation of conventional MreBs (Fig. I-2), indicating that every class of SMreB is as far distant as conventional MreBs. In contrast, the five classes of SMreBs are divided into three groups based on sequence identities (SMreB1 and 4, SMreB2 and 5, and SMreB3) (116). My *in vitro* experiments also revealed the distinct properties of SpeMreB3 and SpeMreB5 (see chapters 2 and 3). In this section, I summarize the properties of each SMreB group based on currently available data.

SMreB3

SMreB3 possesses many intriguing properties in the actin superfamily. SMreB3 lacks amino acid residues required for ATP hydrolysis, and the low ATPase activity was confirmed for SpeMreB3 (Figs. I-3, II-9A-C&G). SpeMreB3 also possessed around 10 times higher critical concentration than those of other actin superfamily proteins (Fig. II-11E and G, Table II-3) (12, 182, 190, 191). As depolymerization requires the completion of the ATPase reaction, the high critical concentration of SpeMreB3 is likely derived from a slow polymerization rather than a fast depolymerization. Cytoskeletal proteins including actin generally possess acidic isoelectric points and form negatively charged filaments (63, 125, 201, 214). In contrast, the SpeMreB3 filament was widely surrounded by positively charged regions even at a neutral pH (Fig. III-2J). All the above features, to the best of my knowledge, have not been reported in the actin superfamily. While a previous study found that SMreB3 is not essential for *Spiroplasma* swimming (84), the distribution of SMreB3 over the *Spiroplasma* genus (Fig. I-2) (132) suggests its

importance for the viability of *Spiroplasma*. Another characteristic of SMreB3 is the presence of two membrane binding sequences; two consecutive hydrophobic residues at the hydrophobic loop in subdomain IA for both Apis and Citri subgroups and an amphipathic helix at the N-terminus for the Citri group (Fig. I-1E and G). This feature is common to that of walled-bacterial MreBs (122). A previous study reported that the N-terminal amphipathic helix is conserved for some MreBs of Gram-negative bacteria but not conserved for those of Gram-positive bacteria (122). SMreB3 probably acquired the N-terminal amphipathic helix independently to MreBs of Gram-negative bacteria as *Spiroplasma* has evolved from the phylum Firmicutes, a group of Gram-positive bacteria (77, 78).

SMreB2 and 5

SMreB2 and 5 showed several properties that have been reported for walled-bacterial MreBs. The P_i release rate and the critical concentration of SpeMreB5 were similar to those of other MreBs (Figs. II-9A-C, II-11E and F, III-6A and E, Tables II-3, III-1) (131, 177, 182, 186, 191, 194). Moreover, SpeMreB5 formed paracrystal structures that are also reported for TmMreB and EcMreB (Figs. III-1A and E, III-3C, D, H, and I, III-7B and D) (177, 186, 194).

In contrast, there were several SpeMreB5 characteristics that have not been reported in the actin superfamily. The P_i release rate of SpeMreB5 was constant over time (Fig. II-9A), while those of actin and TmMreB were gradually reaching the plateaus after the initiation of the reaction (130, 182, 194). The plateau of P_i release was also confirmed in SpeMreB3 K174T/S176D (Fig. II-9A). The P_i release rate of actin is limited at the nucleotide exchange step from ADP to ATP because that step does not occur in actin filaments while most actin molecules are associated with the filaments at the solution

condition for the polymerization (130, 215). The nucleotide-binding pocket of SMreB5 was common to those of BMreB at both amino acid sequence and structural levels (Figs. I-1B, I-3) (131), suggesting that SMreB5 does not exchange the nucleotide in the filaments as well as actin. These facts suggest that polymerized SpeMreB5, especially SpeMreB5 sheets which were the majority at the condition for P_i release measurements (Fig. II-2B), quickly exchange the subunits. Considering SpeMreB3 K174T/S176D only formed double-stranded filaments, and its P_i release profile was plateaued (Fig. II-9A), the putative fast subunit exchange of SpeMreB5 sheets likely occur at the parallelly aligning protofilaments (Figs. II-2E, II-4A). Although a fast subunit exchange leads to a high depolymerization rate resulting in a high critical concentration, the critical concentration of SpeMreB5 was similar to those of other MreBs (Figs. II-11E and F, III-6A and E, Tables II-3, III-1) (12, 182, 190, 191), suggesting that SpeMreB5 sheets dissociate the subunits with oligomer units.

Another unique feature of SMreB5 is the positively charged C-terminal region (Figs. I-1F and G, I-3, III-5A). A previous study revealed that the C-terminal region of SciMreB5, rather than hydrophobic residues at the hydrophobic loop, interacts with the negatively charged membrane with the identical lipid composition to the *Spiroplasma* membrane (131). This membrane binding format likely makes the regulation of the membrane association easier than binding by hydrophobic residues. In fact, the membrane binding of SciMreB5 is reported to be regulated by the reaction cycle of its ATPase (131). My study found that the C-terminal region was involved in the formation of aggregates which were disassembled by ATP (Figs. III-3G, III-5B, III-9). This phenomenon may be useful to store SMreB5 molecules in the cells. A similar phenomenon and discussion were reported on FtsZ whose C-terminal tail region interacts

with the DNA-SlmA complex to undergo liquid-liquid phase separation (216). My EM study revealed that SpeMreB5 forms asymmetric sheets (Figs. II-2E, II-4A). It is unclear whether this structure is specific for SMreB5 as the resolution of sheet structures of walled-bacterial MreB did not reach to the subunit order (37, 177, 194). However, I believe that the asymmetric sheet structures are unique to SMreB5 referring to the discussion on the linear P_i release rate of SpeMreB5 (see the last paragraph).

A previous study assumed that SMreB2 possess similar properties to SMreB5 (116). However, this assumption is still debatable. Although these SMreBs show 60% sequence identity which is the second highest in all SMreB combinations (85, 116), SMreB2 was not able to complement SMreB5 in *Spiroplasma* swimming (84, 85). Moreover, SMreB2 does not possess a positively charged C-terminal region which is one of the unique characteristics of SMreB5 (Fig. I-3) (131). Biochemical analyses using actin revealed that reaction rates related to polymerization dynamics of *Leishmania* and animal actins are distinct from each other although they show around 70% sequence identity each other (217). Differences in the reaction rates from animal actin were even found in fission yeast actin which is around 90% identical to animal actin (218). Thus, the cellular functions and properties of SMreB2 should be studied in the future.

SMreB1 and 4

In this study, I was not able to describe detailed insights on the functions and features of SMreB1 and SMreB4 at the levels of the other SMreBs due to the inability of their purifications and *in vitro* analyses. However, their properties can be expected based on my *in silico* analyses and the data of *in vitro* analyses of SpeMreB3 and SpeMreB5. Both SMreB1 and SMreB4 conserve the sequences of the nucleotide-binding pocket and for ATP hydrolysis (Figs. I-1B, I-3, II-9G), suggesting that they show identical P_i release

rates to those of SMreB5 and walled-bacterial MreBs (Table II-2) (131, 177, 186). To predict the filamentous structures of SMreB1 and SMreB4, I predicted the structure of SciMreB4 by AlphaFold2 and constructed the protofilament and double-stranded filament models with the surface potential maps at pH 7 (Fig. IV-1A). Of note, as the structure was predicted by the full-length sequence, the surface potential of the membrane side is probably predicted correctly. The front side of the protofilament and the moieties of subdomain IA and IIA on the back side are charged positively and negatively, respectively (Fig. IV-1A), suggesting that SMreB1 and SMreB4 form sheet structures as observed in SpeMreB5 (Figs. II-2E, II-4A). The cytosolic region of the SciMreB4 filament model is surrounded by a negatively charged region, suggesting that SMreB1 and SMreB4 also form paracrystals as well as SpeMreB5 (Figs. III-1A and E, III-3C, D, H, and I, III-7B and D). The membrane side is surrounded by a positively charged region, suggesting that this side forms electrostatic interactions with the negatively charged *Spiroplasma* membrane like SciMreB5 (131). Although SMreB1 and SMreB4 of Citri group species do not have hydrophobic residues at the hydrophobic loop for the membrane binding (Fig. I-3) (122), this region may not be related to the membrane binding of these SMreBs as reported in SciMreB5 (131). Altogether, SMreB1 and SMreB4 are expected to possess similar properties to SpeMreB5 in their ATPase activity and assembly properties.

Working model of *Spiroplasma* swimming

The core force generation unit of *Spiroplasma* swimming is composed of the combination of SMreB5 and either SMreB1 or SMreB4 (84). A previous prospect proposed the bimetallic strip model as a working model of the swimming mechanism (Fig.

IV-1B) (219). In this model, the helicity switching for *Spiroplasma* swimming is derived from the cooperative extensions and contractions of the edge protofilaments in the internal ribbon structure. The extensions and contractions are supposed to be generated by the cooperative switching of association and dissociation of laterally aligned filaments of two SMreB isoforms between two fibril bundles. The depolymerized SMreB molecules are explained to be kept associating in the ribbon by the lateral interactions with adjacent SMreB and fibril filaments. However, this model contains at least seven contradictions as follows. (I) Although this model hypothesizes that SMreB filaments are sandwiched between two fibril bundles along the entire cell axis, this assumption may not fully reflect previous findings. While Kürner *et al.* observed the corresponding structure (114), Trachtenberg *et al.* observed an alternative structure in which SMreB filaments are localized between fibril filaments and the membrane (113). As Trachtenberg *et al.* discussed that these structural differences did not come from the artifact during the sample preparation procedure (113), the architecture of the internal ribbon is still controversial. Moreover, it has not confirmed yet whether the structure observed by Kürner *et al.* is elongating along the entire cell axis (114). (II) The model assumes that SMreB molecules remain in the ribbon by lateral interactions with adjacent SMreB and fibril filaments even after the depolymerization. However, lateral interactions are generally weaker than longitudinal interactions (70, 71), and are probably not strong enough to hold the depolymerized subunits in place. In fact, previous studies showed that filaments with consistent dimensions to SMreB filaments were not found in the isolated ribbon, and the stoichiometry of SMreBs in the fraction of the isolated ribbon was much lower than fibril (111, 146). (III) Although the bimetallic strip model is constructed based on two laterally aligned SMreB filaments, Kürner *et al.* observed nine probable SMreB protofilaments

between two fibril bundles (114). Attempting to match with the bimetallic strip model, central SMreB protofilaments are not eligible for force generation as the subunits within central protofilaments are separated by the polymerized protofilament at one edge for every force generation cycle. (IV) When subunits in a protofilament are separated, the signal from a line plot analysis becomes unclear. However, the signals of most protofilaments were enough clear in line plot analyses in previous studies, suggesting that SMreB protofilaments are not separated (111, 114). (V) Based on the bimetallic strip model, all energy for the kink propagation should be generated at the cell tip. However, this assumption cannot explain the switching of the swimming direction before the completion of the kink propagation (111). (VI) In the bimetallic strip model, SMreB filaments are supported by fibril filaments. However, fibril is not essential for *Spiroplasma* swimming (83, 84). Based on the bimetallic strip model, the cells just continue the extensions and contractions when fibril filaments are absent as SMreB filaments lose the lateral supports, suggesting that fibril functions for some other roles than supporting SMreB filaments. (VII) No experimental data have been reported for supporting the bimetallic strip model.

A previous study suggested that SMreB1 and/or SMreB4 form a static backbone along the cells and SMreB5 works as a motor for force generation (116). Here, I develop another working model for *Spiroplasma* swimming by integrating my studies and previous findings (Fig. IV-1C). My working model is composed of three steps. (I) When *Spiroplasma* cells are resting, an SMreB1 and/or SMreB4 sheet localize between fibril filaments and the membrane as observed in Trachtenberg *et al*. (113). (II) SMreB5 polymerizes into a sheet on the membrane from the cell tip toward the end and relocates the SMreB1 and/or SMreB4 sheet within fibril filaments as observed in Kürner *et al*.

(114). In this step, the local conformation of the SMreB1 and/or SMreB4 sheet is changed to switch the ribbon helicity. (III) The SMreB5 sheet depolymerizes from the cell tip, and the localization of the SMreB1 and/or SMreB4 sheet and the ribbon helicity return to those of the resting state. To meet this model, the polymerization and depolymerization rates of SMreB5 sheets should reach the kink propagation velocity (10 μm/s) (110). Assuming that the polymerization rate of SMreB5 protofilament in the sheets is identical to that of ATP-bound actin at the barbed end (11.6 /μM/s) (12) and suppose that the subunit length is ~5 nm (Fig. II-6A), the cellular concentration of SMreB5 should be ~200 μM. As this concentration matches well with the cellular concentration of actin (24, 25), this assumption is realistic. This presumable high cellular concentration of SMreB5 is also supported by previous findings where SMreB5 is one of the most highly expressed proteins in *Spiroplasma* cells (116). If the depolymerization rate of SMreB5 sheets is assumed to be identical to actin filaments (12), it is too slow to support the kink propagation velocity of *Spiroplasma* cells (110). However, the depolymerization rate of SMreB5 sheets is likely faster than that of actin filaments based on the discussion of the linear P_i release profile over time (see the last section). This model assumes the interaction between the membrane side of the SMreB1 and/or SMreB4 sheet and the cytosolic side of the SMreB5 sheet. The formation of this interaction is reasonable considering the surface potential maps of SciMreB4 and SciMreB5 filaments (Figs. III-2E, IV-1A). This model also assumes that the SMreB1 and/or SMreB4 sheet is stable. The unique amino acid residues on the intra- and inter-protofilament interaction regions of SMreB1 and SMreB4 may be related to the putative stability of the sheet (Figs. I-1C and D, I-3).

To support this model, the following questions must be solved. How are the polymerization dynamics of SMreB1 and SMreB4? What filamentous structures do

SMreB1 and SMreB4 form? How many are the polymerization and depolymerization rates of SMreB1, SMreB4, and SMreB5? How does SMreB5 influence the polymerization dynamics and filamentous structures of SMreB1 and SMreB4 and *vice versa*? A previous study suggested that SMreB3 is involved in *Spiroplasma* swimming as a membrane anchor of the SMreB1 and/or SMreB4 (116). How are SMreB3 filaments related to this model? How are the conformations of the internal ribbon and the cell morphology linked? I hope that these questions are solved and my working model is supported and/or renovated in the future.
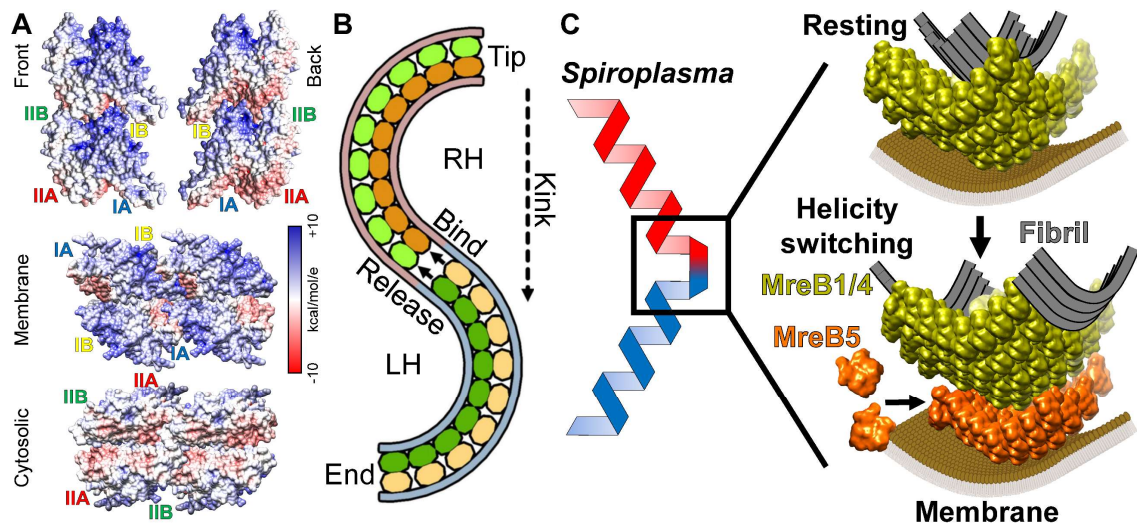
Figure IV-1. A working model for *Spiroplasma* swimming. (**A**) Surface potential map of SciMreB4 in which the monomer structure was predicted by AlphaFold2 (156). The protofilament and double-stranded filament models are created in the same way as the models of EcMreB (Fig. III-2L). The coulombic electrostatic potential is indicated by a color gradient from blue (10 kcal/mol/e) to red (−10 kcal/mol/e); namely blue, white, and red regions indicate positively charged, uncharged, and negatively charged regions, respectively. (**B**) Schematics of the bimetallic strip model used in a previous prospect (219). In this model, the kink propagation is supposed to be generated by continuous associations and dissociations of longitudinally aligned two groups of SMreBs (indicated as ellipses with green and yellow scaled colors). Two fibril bundles beside the SMreB filaments are indicated by S-shaped lines colored magenta (for the right-handed (RH) region) and blue (for the left-handed (LH) region). (**C**) A working model of *Spiroplasma* swimming. Putative conformations of the intracellular ribbon structure at resting and helicity switching states are shown.

**Conservation of core properties of actin superfamily proteins**

In this thesis, I reported polymerization dynamics linked to the reaction cycle of ATPase, the conformational change of a subunit within a protofilament, and a putative ATP hydrolysis mechanism of MreB through the analyses of SpeMreB3 and SpeMreB5 (see chapter 2). In this section, I compare them to those of other actin superfamily proteins. MreB is suggested to polymerize by ATP binding and depolymerize after the release of P_i (Fig. II-12). This feature is common to those of other actin superfamily proteins and, moreover, tubulin superfamily proteins (12, 13, 220). Although MreB filaments have been thought to be stable based on the antiparallel polarity (120), my results suggested a dynamic property of MreB filaments (Fig. II-12). Stable filament formation using ATP are reported for SpoIVA which is a spore coat protein of *B. subtilis* (221). SpoIVA hydrolyzes ATP at the monomeric state and releases ADP and P_i upon polymerization. As a result of these reactions, SpoIVA forms nucleotide-free filaments which are stable owing to the absence of an energy source to generate dynamics (222, 223). Therefore, it is most plausible that MreB filaments, in which a subunit binds to a nucleotide (Figs. II-6A, II-9D-F) (37, 75, 85, 131), are dynamic based on the comparison with SpoIVA filaments as well as my analyses on SpeMreBs (Fig. II-12).

My crystal structural analyses of SpeMreB3 revealed the swing motion of subdomain IB upon nucleotide binding (Figs. II-6D, II-7C). This conformational change is akin to "flattening" widely found in actin superfamily proteins (59, 72, 75, 124). Flattening depends on polymerization rather than the reaction steps of ATPase (129, 224, 225). CcMreB can flatten the conformation in the absence of nucleotides upon the protofilament formation in a crystal (75). However, the flattening of SpeMreB3 is induced by nucleotide binding rather than polymerization (Figs. II-6D, II-7C), suggesting that the

- 113 -

nucleotide binding also promotes the flattening. The flattening mechanism of actin in the absence of nucleotides is not understood as nucleotide-free actin is unstable except for harsh conditions with a high sucrose concentration (226, 227). My finding on the SpeMreB3 flattening (Figs. II-6D, II-7C) will shed light on the structural dynamics of actin superfamily proteins.

In this thesis, I proposed an ATP hydrolysis mechanism of MreB including a proton elimination step (Fig. II-9H). The positions of hydroxy groups in MreB to facilitate ATP hydrolysis are common to those of actin (130). Based on these findings, I discuss the conservation of the ATP hydrolysis mechanism in actin superfamily proteins (Fig. IV-2). Of note, this is not the best comparison due to the lack of resolutions and pre-hydrolysis structures for some proteins. Moreover, I cannot rule out a possibility where the structures shown in Fig. IV-2 are outliers due to the lack of sequence analyses on each family except for MreB. However, it is noteworthy that these structures enable us to compare the positions of residues important for ATP hydrolysis among proteins used as models of each family (Fig. IV-2). Bacterial actins possess either glutamate, glutamine, or serine at the corresponding position of E140 in CcMreB. In contrast, the threonine-an acidic residue pair corresponding to T167-E169 in CcMreB, which is an essential residue pair for ATP hydrolysis (Fig. II-9A, B, and H), is conserved for bacterial actins (Fig. IV-2C-F). Another acidic residue corresponding to D154 in actin is also conserved for bacterial actins. While this residue is not examined in this thesis, previous studies using MreB and another bacterial actin Alp7A reported that this residue is involved in ATPase activity (41, 131). These findings suggest that the ATP hydrolysis mechanism proposed in this study (Fig. II-9H) is not only conserved for MreB but also for bacterial actins. In contrast, an archaeal actin, crenactin possesses a different active site structure from those of eukaryotic and

bacterial actins (Fig. IV-2A and B). Q137 in actin is found in crenactin as Q164 (Fig. IV-2A and B). The residue pair D162-T167-E169 in CcMreB is replaced in crenactin as E181-N186-Q188 (Fig. IV-2B and C). If the amino group of N186 interacts with the nucleophilic water, ATP hydrolysis in crenactin can be facilitated by a proton elimination of the nucleophilic water by N186. A high-resolution structure of crenactin filaments at the pre-hydrolysis state will be needed for the conclusion. The residue corresponding to T167 in CcMreB and N186 in crenactin is replaced with V159 in actin (Fig. IV-2A-C), indicating that this residue became not to be involved in ATP hydrolysis during the evolutionary way. These comparisons raise one fundamental question: why the active site structures are different among bacterial, archaeal, and eukaryotic actins despite the possibly common ATP hydrolysis mechanism? For eukaryotic actin, subtle structural changes in the reaction steps of ATPase influence the properties of actin filaments such as the longitudinal interactions of subunits and the bending stiffness of the filaments (126, 129, 224, 228). The structural differences in the active sites of actins among the three phylogenetic domains might reflect distinct linkages between ATPase reactions and the filament functions.
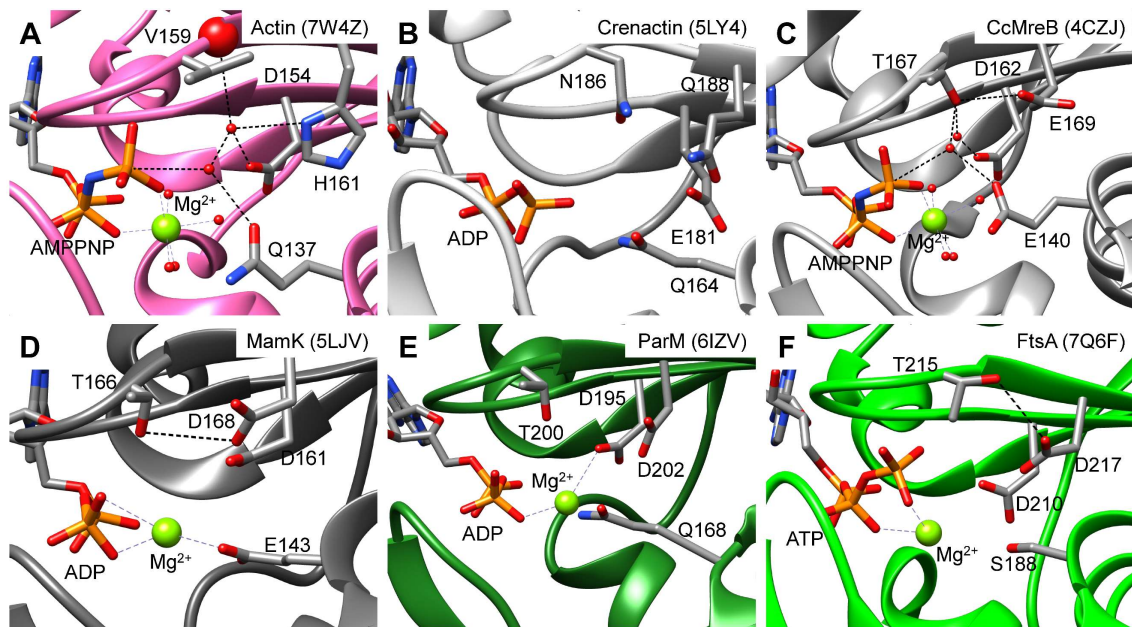
Figure IV-2. Active site structures of (A) actin (PDB ID: 7W4Z), (B) crenactin (PDB ID: 5LY4), (C) CcMreB (PDB ID: 4CZJ), (D) MamK (PDB ID: 5LJV), ParM (PDB ID: 6IZV), and (F) FtsA (PDB ID: 7Q6F) all at filamentous states. Mg^{2+} and water molecules are indicated as green and red spheres, respectively.

Conclusions

In this thesis, I evaluated the evolution of SMreBs and characterized them by *in silico* methods. These analyses propose the unique evolutionary way and properties of SMreBs. I also analyzed SpeMreB3 and SpeMreB5 through *in vitro* experiments for characterizing their structures, ATPase activities, polymerization dynamics, and bundle formation. These results revealed distinct properties of SpeMreB3 and SpeMreB5 possibly resulting in the differences in the cellular functions. These findings will shed light on molecular insights into SMreB functions for driving the unique motility system. During these studies, I proposed polymerization dynamics linked to the ATPase reaction and a putative ATP hydrolysis mechanism both of which are probably common to MreB family proteins and akin to those of actin. These findings will be a clue to discuss the diversity and universality of the actin superfamily which is one of the widest-spreading protein groups involved in various biological phenomena.

Acknowledgements

References

1. Alberts B*, et al.* (2015) *Molecular biology of the cell* (Garland Science, Taylor and Francis Group, New York, NY) Sixth edition. Chapter 16, The Cytoskeleton Ed.

2. Sallee MD & Feldman JL (2021) Microtubule organization across cell types and states. *Curr Biol* 31(10):R506-R511.

3. Bashirzadeh Y, Wubshet NH, & Liu AP (2020) Confinement geometry tunes fascin-actin bundle structures and consequently the shape of a lipid bilayer vesicle. *Front Mol Biosci* 7:610277.

4. Stricker J, Falzone T, & Gardel ML (2010) Mechanics of the F-actin cytoskeleton. *J Biomech* 43(1):9-14.

5. Fletcher DA & Mullins RD (2010) Cell mechanics and the cytoskeleton. *Nature* 463(7280):485-492.

6. Pollard TD & Cooper JA (2009) Actin, a central player in cell shape and movement. *Science* 326(5957):1208-1212.

7. Cleary JM & Hancock WO (2021) Molecular mechanisms underlying microtubule growth dynamics. *Curr Biol* 31(10):R560-R573.

8. Fujiwara I, Vavylonis D, & Pollard TD (2007) Polymerization kinetics of ADP- and ADP-P_i-actin determined by fluorescence microscopy. *Proc Natl Acad Sci U S A* 104(21):8827-8832.

9. Fujiwara I, Takahashi S, Tadakuma H, Funatsu T, & Ishiwata Si (2002) Microscopic analysis of polymerization dynamics with individual actin filaments. *Nat Cell Biol* 4(9):666-673.

10. Hyman AA, Salser S, Drechsel DN, Unwin N, & Mitchison TJ (1992) Role of GTP hydrolysis in microtubule dynamics: information from a slowly hydrolyzable analogue, GMPCPP. *Mol Biol Cell* 3(10):1155-1167.

11. Walker RA*, et al.* (1988) Dynamic instability of individual microtubules analyzed by video light microscopy: rate constants and transition frequencies. *J Cell Biol* 107(4):1437-1448.

12. Pollard TD (1986) Rate constants for the reactions of ATP- and ADP-actin with the ends of actin filaments. *J Cell Biol* 103(6):2747-2754.

13. Wegner A (1976) Head to tail polymerization of actin. *J Mol Biol* 108(1):139-150.

14. Risteski P, Jagrić M, Pavin N, & Tolić IM (2021) Biomechanics of chromosome alignment at the spindle midplane. *Curr Biol* 31(10):R574-R585.

15. Svitkina T (2018) The actin cytoskeleton and actin-based motility. *Cold Spring*

Harb Perspect Biol 10(1):a018267.

16. Bun P, Dmitrieff S, Belmonte JM, Nédélec FJ, & Lénárt P (2018) A disassembly-driven mechanism explains F-actin-mediated chromosome transport in starfish oocytes. *eLife* 7:e31469.

17. Oelz Dietmar B, Rubinstein Boris Y, & Mogilner A (2015) A combination of actin treadmilling and cross-linking drives contraction of random actomyosin arrays. *Biophys J* 109(9):1818-1829.

18. Mendes Pinto I, Rubinstein B, Kucharavy A, Unruh Jay R, & Li R (2012) Actin depolymerization drives actomyosin ring contraction during budding yeast cytokinesis. *Dev Cell* 22(6):1247-1260.

19. Pollard TD & Borisy GG (2003) Cellular motility driven by assembly and disassembly of actin filaments. *Cell* 112(4):453-465.

20. Kabsch W, Mannherz HG, Suck D, Pai EF, & Holmes KC (1990) Atomic structure of the actin: DNase I complex. *Nature* 347(6288):37-44.

21. Holmes KC, Popp D, Gebhard W, & Kabsch W (1990) Atomic model of the actin filament. *Nature* 347(6288):44-49.

22. Straub F (1943) Actin, ii. *Stud. Inst. Med. Chem. Univ. Szeged* 3:23-37.

23. Straub F (1942) Stud. Inst. med. *Chem. Szeged* 2:3.

24. Funk J, *et al.* (2019) Profilin and formin constitute a pacemaker system for robust actin filament growth. *eLife* 8:e50963.

25. Milo R & Philips R (2015) *Cell biology by the numbers* (Garland Science).

26. Mishra M, Huang J, & Balasubramanian MK (2014) The yeast actin cytoskeleton. *FEMS Microbiol Rev* 38(2):213-227.

27. Pollard TD, Blanchoin L, & Mullins RD (2000) Molecular mechanisms controlling actin filament dynamics in nonmuscle cells. *Annu Rev Biophys Biomol Struct* 29:545-576.

28. Wang X & Lutkenhaus J (1996) FtsZ ring: the eubacterial division apparatus conserved in archaebacteria. *Mol Microbiol* 21(2):313-320.

29. Mukherjee A, Dai K, & Lutkenhaus J (1993) *Escherichia coli* cell division protein FtsZ is a guanine nucleotide binding protein. *Proc Natl Acad Sci U S A* 90(3):1053-1057.

30. RayChaudhuri D & Park JT (1992) *Escherichia coli* cell-division gene *ftsZ* encodes a novel GTP-binding protein. *Nature* 359(6392):251-254.

31. de Boer P, Crossley R, & Rothfield L (1992) The essential bacterial cell-division protein FtsZ is a GTPase. *Nature* 359(6392):254-256.

32. Bi E & Lutkenhaus J (1991) FtsZ ring structure associated with division in

Escherichia coli. *Nature* 354(6349):161-164.

33.   Löwe J & Amos LA (1998) Crystal structure of the bacterial cell-division protein FtsZ. *Nature* 391(6663):203-206.

34.   Mukherjee A & Lutkenhaus J (1994) Guanine nucleotide-dependent assembly of FtsZ into filaments. *J Bacteriol* 176(9):2754-2758.

35.   Bramhill D & Thompson CM (1994) GTP-dependent polymerization of *Escherichia coli* FtsZ protein to form tubules. *Proc Natl Acad Sci U S A* 91(13):5813-5817.

36.   Bork P, Sander C, & Valencia A (1992) An ATPase domain common to prokaryotic cell cycle proteins, sugar kinases, actin, and hsp70 heat shock proteins. *Proc Natl Acad Sci U S A* 89(16):7290-7294.

37.   van den Ent F, Amos LA, & Löwe J (2001) Prokaryotic origin of the actin cytoskeleton. *Nature* 413(6851):39-44.

38.   Jones LJF, Carballido-López R, & Errington J (2001) Control of cell shape in bacteria: helical, actin-like filaments in *Bacillus subtilis*. *Cell* 104(6):913-922.

39.   Wagstaff J & Löwe J (2018) Prokaryotic cytoskeletons: protein filaments organizing small cells. *Nat Rev Microbiol* 16(4):187-201.

40.   Gunning PW, Ghoshdastider U, Whitaker S, Popp D, & Robinson RC (2015) The evolution of compositionally and functionally distinct actin filaments. *J Cell Sci* 128(11):2009-2019.

41.   Derman AI*, et al.* (2009) Phylogenetic analysis identifies many uncharacterized actin-like proteins (Alps) in bacteria: regulated polymerization, dynamic instability and treadmilling in Alp7A. *Mol Microbiol* 73(4):534-552.

42.   Du S & Lutkenhaus J (2017) Assembly and activation of the Escherichia coli divisome. *Mol Microbiol* 105(2):177-187.

43.   den Blaauwen T, Hamoen LW, & Levin PA (2017) The divisome at 25: the road ahead. *Curr Opin Microbiol* 36:85-94.

44.   Shi H, Bratton BP, Gitai Z, & Huang KC (2018) How to build a bacterial cell: MreB as the foreman of *E. coli* construction. *Cell* 172(6):1294-1305.

45.   Gayathri P & Harne S (2017) Structure and dynamics of actin-like cytomotive filaments in plasmid segregation. *Prokaryotic Cytoskeletons: Filamentous Protein Polymers Active in the Cytoplasm of Bacterial and Archaeal Cells*, eds Löwe J & Amos LA (Springer International Publishing, Cham), pp 299-321.

46.   Fink G & Aylett CHS (2017) Tubulin-like proteins in prokaryotic DNA positioning. *Prokaryotic Cytoskeletons: Filamentous Protein Polymers Active in the Cytoplasm of Bacterial and Archaeal Cells*, eds Löwe J & Amos LA (Springer

International Publishing, Cham), pp 323-356.

47. Fink G & Löwe J (2015) Reconstitution of a prokaryotic minus end-tracking system using TubRC centromeric complexes and tubulin-like protein TubZ filaments. *Proc Natl Acad Sci U S A* 112(15):E1845-E1850.

48. Salje J, Gayathri P, & Löwe J (2010) The ParMRC system: molecular mechanisms of plasmid segregation by actin-like filaments. *Nat Rev Microbiol* 8(10):683-692.

49. Larsen RA, *et al.* (2007) Treadmilling of a prokaryotic tubulin-like protein, TubZ, required for plasmid stability in *Bacillus thuringiensis*. *Genes Dev* 21(11):1340-1352.

50. Tinsley E & Khan SA (2006) A novel FtsZ-like protein is involved in replication of the anthrax toxin-encoding pXO1 plasmid in *Bacillus anthracis*. *J Bacteriol* 188(8):2829-2835.

51. Taoka A, *et al.* (2017) Tethered magnets are the key to magnetotaxis: Direct observations of *Magnetospirillum magneticum* AMB-1 show that MamK distributes magnetosome organelles equally to daughter cells. *mBio* 8(4):e00679-00617.

52. Komeili A, Li Z, Newman DK, & Jensen GJ (2006) Magnetosomes are cell membrane invaginations organized by the actin-like protein MamK. *Science* 311(5758):242-245.

53. Imachi H, *et al.* (2020) Isolation of an archaeon at the prokaryote–eukaryote interface. *Nature* 577(7791):519-525.

54. Ithurbide S, Gribaldo S, Albers S-V, & Pende N (2022) Spotlight on FtsZ-based cell division in Archaea. *Trends Microbiol* 30(7):665-678.

55. Pende N, *et al.* (2021) SepF is the FtsZ anchor in archaea, with features of an ancestral cell division system. *Nat Commun* 12(1):3214.

56. Liao Y, Ithurbide S, Evenhuis C, Löwe J, & Duggin IG (2021) Cell division in the archaeon *Haloferax volcanii* relies on two FtsZ proteins with distinct functions in division ring assembly and constriction. *Nat Microbiol* 6(5):594-605.

57. Rodrigues-Oliveira T, *et al.* (2023) Actin cytoskeleton and complex cell architecture in an Asgard archaeon. *Nature* 613(7943):332-339.

58. Akıl C, *et al.* (2022) Structure and dynamics of Odinarchaeota tubulin and the implications for eukaryotic microtubule evolution. *Sci Adv* 8(12):eabm2225.

59. Izoré T, Kureisaite-Ciziene D, McLaughlin SH, & Löwe J (2016) Crenactin forms actin-like double helical filaments regulated by arcadin-2. *eLife* 5:e21600.

60. Braun T, *et al.* (2015) Archaeal actin from a hyperthermophile forms a single-stranded filament. *Proc Natl Acad Sci U S A* 112(30):9340-9345.

61. Izoré T, Duman R, Kureisaite-Ciziene D, & Löwe J (2014) Crenactin from *Pyrobaculum calidifontis* is closely related to actin in structure and forms steep helical filaments. *FEBS Lett* 588(5):776-782.

62. Ettema TJG, Lindås A-C, & Bernander R (2011) An actin-based cytoskeleton in archaea. *Mol Microbiol* 80(4):1052-1061.

63. Popp D & Robinson RC (2011) Many ways to build an actin filament. *Mol Microbiol* 80(2):300-308.

64. Deng X, *et al.* (2017) Four-stranded mini microtubules formed by *Prosthecobacter* BtubAB show dynamic instability. *Proc Natl Acad Sci U S A* 114(29):E5950-E5958.

65. Zehr Elena A, *et al.* (2014) The structure and assembly mechanism of a novel three-stranded tubulin filament that centers phage DNA. *Structure* 22(4):539-548.

66. Montabana EA & Agard DA (2014) Bacterial tubulin TubZ-Bt transitions between a two-stranded intermediate and a four-stranded filament upon GTP hydrolysis. *Proc Natl Acad Sci U S A* 111(9):3407-3412.

67. Matsui T, *et al.* (2012) Structural reorganization of the bacterial cell-division protein FtsZ from *Staphylococcus aureus*. *Acta Crystallogr D Biol Crystallogr* 68(Pt 9):1175-1188.

68. Nierhaus T, *et al.* (2022) Bacterial divisome protein FtsA forms curved antiparallel double filaments when binding to FtsN. *Nat Microbiol* 7(10):1686-1701.

69. Koh F, *et al.* (2019) The structure of a 15-stranded actin-like filament from *Clostridium botulinum*. *Nat Commun* 10(1):2856.

70. Usluer GD, *et al.* (2018) Cryo-EM structure of the bacterial actin AlfA reveals unique assembly and ATP-binding interactions and the absence of a conserved subdomain. *Proc Natl Acad Sci U S A* 115(13):3356-3361.

71. Szewczak-Harris A & Löwe J (2018) Cryo-EM reconstruction of AlfA from *Bacillus subtilis* reveals the structure of a simplified actin-like filament at 3.4-Å resolution. *Proc Natl Acad Sci U S A* 115(13):3458-3463.

72. Löwe J, He S, Scheres SHW, & Savva CG (2016) X-ray and cryo-EM structures of monomeric and filamentous actin-like protein MamK reveal changes associated with polymerization. *Proc Natl Acad Sci U S A* 113(47):13396-13401.

73. Jiang S, *et al.* (2016) Novel actin filaments from *Bacillus thuringiensis* form nanotubules for plasmid DNA segregation. *Proc Nat Acad Sci U S A* 113(9):E1200-E1205.

74. Bharat TAM, Murshudov GN, Sachse C, & Löwe J (2015) Structures of actin-like

ParM filaments show architecture of plasmid-segregating spindles. *Nature* 523(7558):106-110.

75. van den Ent F, Izore T, Bharat TA, Johnson CM, & Löwe J (2014) Bacterial actin MreB forms antiparallel double filaments. *eLife* 3:e02634.

76. Gayathri P*, et al.* (2012) A bipolar spindle of antiparallel ParM filaments drives bacterial plasmid segregation. *Science* 338(6112):1334-1337.

77. Castelle CJ & Banfield JF (2018) Major new microbial groups expand diversity and alter our understanding of the tree of life. *Cell* 172(6):1181-1197.

78. Hug LA*, et al.* (2016) A new view of the tree of life. *Nat Microbiol* 1(5):16048.

79. Ceron RH*, et al.* (2022) A solution to the long-standing problem of actin expression and purification. *Proc Natl Acad Sci U S A* 119(41):e2209150119.

80. Ouellette SP*, et al.* (2022) Localized cardiolipin synthesis is required for the assembly of MreB during the polarized cell division of *Chlamydia trachomatis*. *PLoS Pathog* 18(9):e1010836.

81. Fu G*, et al.* (2018) MotAB-like machinery drives the movement of MreB filaments during bacterial gliding motility. *Proc Natl Acad Sci U S A* 115(10):2484-2489.

82. Waidner B*, et al.* (2009) A novel system of cytoskeletal elements in the human pathogen *Helicobacter pylori*. *PLoS Pathog* 5(11):e1000669.

83. Lartigue C*, et al.* (2022) Cytoskeletal components can turn wall-less spherical bacteria into kinking helices. *Nat Commun* 13(1):6930.

84. Kiyama H, Kakizawa S, Sasajima Y, Tahara YO, & Miyata M (2022) Reconstitution of a minimal motility system based on *Spiroplasma* swimming by expressing two bacterial actins in synthetic minimal bacterium. *Sci Adv* 8(48):eabo7490.

85. Harne S*, et al.* (2020) MreB5 is a determinant of rod-to-helical transition in the cell-wall-less bacterium *Spiroplasma*. *Curr Biol* 30(23):4753-4762.e4757.

86. Wadhwa N & Berg HC (2022) Bacterial motility: machinery and mechanisms. *Nat Rev Microbiol* 20(3):161-173.

87. Miyata M*, et al.* (2020) Tree of motility - A proposed history of motility systems in the tree of life. *Genes Cells* 25(1):6-21.

88. Purcell EM (1977) Life at low Reynolds number. *Am J Phys* 45(1):3-11.

89. Minamino T, Imada K, & Namba K (2008) Molecular motors of the bacterial flagella. *Curr Opin Struct Biol* 18(6):693-701.

90. Nakamura S & Minamino T (2019) Flagella-driven motility of bacteria. *Biomolecules* 9(7):279.

91. Minamino T & Namba K (2004) Self-assembly and type III protein export of the bacterial flagellum. *Microb Physiol* 7(1-2):5-17.

92. Mondino S, San Martin F, & Buschiazzo A (2022) 3D cryo-EM imaging of bacterial flagella: Novel structural and mechanistic insights into cell motility. *J Biol Chem* 298(7):102105.

93. Santiveri M*, et al.* (2020) Structure and function of stator units of the bacterial flagellar motor. *Cell* 183(1):244-257.e16.

94. Deme JC*, et al.* (2020) Structures of the stator complex that drives rotation of the bacterial flagellum. *Nat Microbiol* 5(12):1553-1564.

95. Minamino T, Terahara N, Kojima S, & Namba K (2018) Autonomous control mechanism of stator assembly in the bacterial flagellar motor in response to changes in the environment. *Mol Microbiol* 109(6):723-734.

96. Berg HC (2003) The rotary motor of bacterial flagella. *Annu Rev Biochem* 72(1):19-54.

97. Magariyama Y*, et al.* (1994) Very fast flagellar rotation. *Nature* 371(6500):752-752.

98. Coleman GA*, et al.* (2021) A rooted phylogeny resolves early bacterial evolution. *Science* 372(6542):eabe0511.

99. Kojima S*, et al.* (2018) The helix rearrangement in the periplasmic domain of the flagellar stator B subunit activates peptidoglycan binding and ion influx. *Structure* 26(4):590-598.e595.

100. Razin S & Hayflick L (2010) Highlights of mycoplasma research—An historical perspective. *Biologicals* 38(2):183-190.

101. Razin S (1997) The minimal cellular genome of mycoplasma. *Indian J Biochem Biophys* 34(1-2):124-130.

102. Fraser CM*, et al.* (1995) The minimal gene complement of *Mycoplasma genitalium*. *Science* 270(5235):397-404.

103. Rosengarten R, Kirchhoff H, Kerlen G, & Seack K-H (1988) The surface layer of *Mycoplasma mobile* 163K and its possible relevance to cell cohesion and group motility. *J Gen Microbiol* 134(2):275-281.

104. Claessen D & Errington J (2019) Cell wall deficiency as a coping strategy for stress. *Trends Microbiol* 27(12):1025-1033.

105. Miyata M & Hamaguchi T (2016) Integrated information and prospects for gliding mechanism of the pathogenic bacterium *Mycoplasma pneumoniae*. *Front Microbiol* 7:960.

106. Miyata M & Hamaguchi T (2016) Prospects for the gliding mechanism of

Mycoplasma mobile. Curr Opin Microbiol 29:15-21.

107. Daniels MJ*, et al.* (1973) Axenic culture of a plant pathogenic *Spiroplasma. Nature* 244(5417):523-524.

108. Cole RM, Tully JG, Popkin TJ, & Bové JM (1973) Morphology, ultrastructure, and bacteriophage infection of the helical mycoplasma-like organism (*Spiroplasma citri* gen. nov., sp. nov.) cultured from "stubborn" disease of citrus. *J Bacteriol* 115(1):367-384.

109. Wada H & Netz RR (2009) Hydrodynamics of helical-shaped bacterial motility. *Phys Rev E Stat Nonlin Soft Matter Phys* 80(2 Pt 1):021921.

110. Shaevitz JW, Lee JY, & Fletcher DA (2005) *Spiroplasma* swim by a processive change in body helicity. *Cell* 122(6):941-945.

111. Liu P*, et al.* (2017) Chemotaxis without conventional two-component system, based on cell polarity and aerobic conditions in helicity-switching swimming of *Spiroplasma eriocheiris. Front Microbiol* 8:58.

112. Cohen-Krausz S, Cabahug PC, & Trachtenberg S (2011) The monomeric, tetrameric, and fibrillar organization of Fib: The dynamic building block of the bacterial linear motor of *Spiroplasma melliferum* BC3. *J Mol Biol* 410(2):194-213.

113. Trachtenberg S*, et al.* (2008) Structure of the cytoskeleton of *Spiroplasma melliferum* BC3 and its interactions with the cell membrane. *J Mol Biol* 378(4):778-789.

114. Kürner J, Frangakis AS, & Baumeister W (2005) Cryo-electron tomography reveals the cytoskeletal structure of *Spiroplasma melliferum. Science* 307(5708):436-438.

115. Trachtenberg S, Gilad R, & Geffen N (2003) The bacterial linear motor of *Spiroplasma melliferum* BC3: from single molecules to swimming cells. *Mol Microbiol* 47(3):671-697.

116. Masson F, Pierrat X, Lemaitre B, & Persat A (2021) The wall-less bacterium *Spiroplasma poulsonii* builds a polymeric cytoskeleton composed of interacting MreB isoforms. *iScience* 24(12):103458.

117. Nakamura S (2022) Motility of the zoonotic spirochete *Leptospira*: Insight into association with pathogenicity. *Int J Mol Sci* 23(3):1859.

118. Kawai Y, Asai K, & Errington J (2009) Partial functional redundancy of MreB isoforms, MreB, Mbl and MreBH, in cell morphogenesis of *Bacillus subtilis. Mol Microbiol* 73(4):719-731.

119. Taylor JA*, et al.* (2020) Distinct cytoskeletal proteins define zones of enhanced cell wall synthesis in *Helicobacter pylori. eLife* 9:e52482.

120. Wagstaff JM*, et al.* (2022) Cytomotive actins and tubulins share a polymerisation switch mechanism conferring robust dynamics. *bioRxiv*:2022.2009.2008.507146.

121. Billaudeau C, Yao Z, Cornilleau C, Carballido-López R, & Chastanet A (2019) MreB forms subdiffraction nanofilaments during active growth in *Bacillus subtilis*. *mBio* 10(1):e01879-01818.

122. Salje J, van den Ent F, de Boer P, & Löwe J (2011) Direct membrane binding by bacterial actin MreB. *Mol Cell* 43(3):478-487.

123. Domínguez-Escobar J*, et al.* (2011) Processive movement of MreB-associated cell wall biosynthetic complexes in bacteria. *Science* 333(6039):225-228.

124. Oda T, Iwasa M, Aihara T, Maéda Y, & Narita A (2009) The nature of the globular-to fibrous-actin transition. *Nature* 457(7228):441-445.

125. Oosawa F & Asakura S (1975) *Thermodynamics of the polymerization of protein* (Academic Press).

126. Oosterheert W, Klink BU, Belyy A, Pospich S, & Raunser S (2022) Structural basis of actin filament assembly and aging. *bioRxiv*:2022.2003.2029.486216.

127. Belmont LD, Orlova A, Drubin DG, & Egelman EH (1999) A change in actin conformation associated with filament instability after P_i release. *Proc Natl Acad Sci U S A* 96(1):29-34.

128. Orlova A & Egelman EH (1992) Structural basis for the destabilization of F-actin by phosphate release following ATP hydrolysis. *J Mol Biol* 227(4):1043-1053.

129. Chou SZ & Pollard TD (2019) Mechanism of actin polymerization revealed by cryo-EM structures of actin filaments with three different bound nucleotides. *Proc Natl Acad Sci U S A* 116(10):4265-4274.

130. Kanematsu Y*, et al.* (2022) Structures and mechanisms of actin ATP hydrolysis. *Proc Natl Acad Sci U S A* 119(43):e2122641119.

131. Pande V, Mitra N, Bagde SR, Srinivasan R, & Gayathri P (2022) Filament organization of the bacterial actin MreB is dependent on the nucleotide state. *J Cell Biol* 221(5):e202106092.

132. Ku C, Lo WS, & Kuo CH (2014) Molecular evolution of the actin-like MreB protein gene family in wall-less bacteria. *Biochem Biophys Res Commun* 446(4):927-932.

133. Awuni E & Mu Y (2019) Effect of A22 on the conformation of bacterial actin MreB. *Int J Mol Sci* 20(6):1304.

134. Tsai YM, Chang A, & Kuo CH (2018) Horizontal gene acquisitions contributed to genome expansion in insect-symbiotic *Spiroplasma clarkii*. *Genome Biol Evol* 10(6):1526-1532.

135. Paredes JC, *et al.* (2015) Genome sequence of the *Drosophila melanogaster* male-killing *Spiroplasma* strain MSRO endosymbiont. *mBio* 6(2):e02437-02414.

136. Gasparich GE (2002) Spiroplasmas: evolution, adaptation and diversity. *Front Biosci* 7(4):619-640.

137. Brown CT, *et al.* (2015) Unusual biology across a group comprising more than 15% of domain Bacteria. *Nature* 523(7559):208-211.

138. Rinke C, *et al.* (2013) Insights into the phylogeny and coding potential of microbial dark matter. *Nature* 499(7459):431-437.

139. Zheng R, *et al.* (2021) Characterization of the first cultured free-living representative of *Candidatus* Izemoplasma uncovers its unique biology. *ISME J* 15(9):2676-2691.

140. Antunes A, *et al.* (2011) Genome sequence of *Haloplasma contractile*, an unusual contractile bacterium from a deep-sea anoxic brine lake. *J Bacteriol* 193(17):4551-4552.

141. Megrian D, Taib N, Jaffe AL, Banfield JF, & Gribaldo S (2022) Ancient origin and constrained evolution of the *division and cell wall* gene cluster in Bacteria. *Nat Microbiol* 7(12):2114-2127.

142. Santana-Molina C, Saz-Navarro Dd, & Devos DP (2023) Early origin and evolution of the FtsZ/tubulin protein family. *Front Microbiol* 13:1100249.

143. Schirner K & Errington J (2009) The cell wall regulator σI specifically suppresses the lethal phenotype of *mbl m*utants in *Bacillus subtilis*. *J Bacteriol* 191(5):1404-1413.

144. Formstone A & Errington J (2005) A magnesium-dependent *mreB* null mutant: implications for the role of *mreB* in *Bacillus subtilis*. *Mol Microbiol* 55(6):1646-1657.

145. Carballido-López R, *et al.* (2006) Actin homolog MreBH governs cell morphogenesis by localization of the cell wall hydrolase LytE. *Dev Cell* 11(3):399-409.

146. Sasajima Y, *et al.* (2022) Isolation and structure of the fibril protein, a major component of the internal ribbon for *Spiroplasma* swimming. *Front Microbiol* 13:1004601.

147. Nakane D, Ito T, & Nishizaka T (2020) Coexistence of two chiral helices produces kink translation in *Spiroplasma* swimming. *J Bacteriol* 202(8):e00735-00719.

148. Boudet JF, *et al.* (2018) Large variability in the motility of spiroplasmas in media of different viscosities. *Sci Rep* 8:17138.

149. Awuni Y, Jiang S, Robinson RC, & Mu Y (2016) Exploring the A22-bacterial actin

MreB interaction through molecular dynamics simulations. *J Phys Chem B* 120(37):9867-9874.

150. Aylett CHS, Löwe J, & Amos LA (2011) Chapter one - new insights into the mechanisms of cytomotive actin and tubulin filaments. *Int Rev Cell Mol Biol*, ed Jeon KW (Academic Press), Vol 292, pp 1-71.

151. Iwasa M, Maeda K, Narita A, Maéda Y, & Oda T (2008) Dual roles of Gln[137] of actin revealed by recombinant human cardiac muscle α-actin mutants. *J Biol Chem* 283(30):21045-21053.

152. Wang M, Fang C, Ma B, Luo X, & Hou Z (2020) Regulation of cytokinesis: FtsZ and its accessory proteins. *Curr Genet* 66(1):43-49.

153. Sedgwick B & Lindahl T (2002) Recent progress on the Ada response for inducible repair of DNA alkylation damage. *Oncogene* 21(58):8886-8894.

154. Käll L, Krogh A, & Sonnhammer EL (2004) A combined transmembrane topology and signal peptide prediction method. *J Mol Biol* 338(5):1027-1036.

155. Kovacs-Simon A, Titball RW, & Michell SL (2011) Lipoproteins of bacterial pathogens. *Infect Immun* 79(2):548-561.

156. Mirdita M*, et al.* (2022) ColabFold: making protein folding accessible to all. *Nat Methods* 19(6):679-682.

157. Buddelmeijer N (2015) The molecular mechanism of bacterial lipoprotein modification-how, when and why? *FEMS Microbiol Rev* 39(2):246-261.

158. Jan G, Fontenelle C, Le Hénaff M, & Wróblewski H (1995) Acylation and immunological properties of *Mycoplasma gallisepticum* membrane proteins. *Res Microbiol* 146(9):739-750.

159. Jan G, Le Hénaff M, Fontenelle C, & Wróblewski H (2001) Biochemical and antigenic characterisation of *Mycoplasma gallisepticum* membrane proteins P52 and P67 (pMGA). *Arch Microbiol* 177(1):81-90.

160. Mühlradt PF, Kiess M, Meyer H, Süssmuth R, & Jung G (1998) Structure and specific activity of macrophage-stimulating lipopeptides from *Mycoplasma hyorhinis*. *Infect Immun* 66(10):4804-4810.

161. Serebryakova MV*, et al.* (2011) The acylation state of surface lipoproteins of Mollicute *Acholeplasma laidlawii*. *J Biol Chem* 286(26):22769-22776.

162. Shimizu T, Kida Y, & Kuwano K (2008) A triacylated lipoprotein from *Mycoplasma genitalium* activates NF-κB through toll-like receptor 1 (TLR1) and TLR2. *Infect Immun* 76(8):3672-3678.

163. Le Hénaff M & Fontenelle C (2000) Chemical analysis of processing of spiralin, the major lipoprotein of *Spiroplasma melliferum*. *Arch Microbiol* 173(5):339-345.

164. Duret S*, et al.* (2014) Invasion of insect cells by *Spiroplasma citri* involves spiralin relocalization and lectin/glycoconjugate-type interactions. *Cell Microbiol* 16(7):1119-1132.

165. Andersson SGE & Kurland CG (1998) Reductive evolution of resident genomes. *Trends Microbiol* 6(7):263-268.

166. Kumar S, Stecher G, Li M, Knyaz C, & Tamura K (2018) MEGA X: Molecular evolutionary genetics analysis across computing platforms. *Mol Biol Evol* 35(6):1547-1549.

167. Song Y*, et al.* (2013) High-resolution comparative modeling with RosettaCM. *Structure* 21(10):1735-1742.

168. Meng EC, Pettersen EF, Couch GS, Huang CC, & Ferrin TE (2006) Tools for integrated sequence-structure analysis with UCSF Chimera. *BMC Bioinformatics* 7:339.

169. Sievers F*, et al.* (2011) Fast, scalable generation of high-quality protein multiple sequence alignments using Clustal Omega. *Mol Syst Biol* 7(1):539.

170. Sievers F & Higgins DG (2018) Clustal Omega for making accurate alignments of many protein sequences. *Protein Sci* 27(1):135-145.

171. Crooks GE, Hon G, Chandonia JM, & Brenner SE (2004) WebLogo: a sequence logo generator. *Genome Res* 14(6):1188-1190.

172. Buchan DWA & Jones DT (2019) The PSIPRED protein analysis workbench: 20 years on. *Nucleic Acids Res* 47(W1):W402-W407.

173. Sapay N, Guermeur Y, & Deléage G (2006) Prediction of amphipathic in-plane membrane anchors in monotopic proteins using a SVM classifier. *BMC Bioinformatics* 7(1):255.

174. Terahara N, Tulum I, & Miyata M (2017) Transformation of crustacean pathogenic bacterium Spiroplasma eriocheiris and expression of yellow fluorescent protein. *Biochem Biophys Res Commun* 487(3):488-493.

175. Wang W, Rong L, Gu W, Du K, & Chen J (2003) Study on experimental infections of Spiroplasma from the Chinese mitten crab in crayfish, mice and embryonated chickens. *Res Microbiol* 154(10):677-680.

176. Zivanov J*, et al.* (2018) New tools for automated high-resolution cryo-EM structure determination in RELION-3. *eLife* 7:e42166.

177. Nurse P & Marians KJ (2013) Purification and characterization of *Escherichia coli* MreB protein. *J Biol Chem* 288(5):3469-3475.

178. Shaw N*, et al.* (2007) (NZ)CH...O Contacts assist crystallization of a ParB-like nuclease. *BMC Struct Biol* 7(1):46.

179. Walter TS, *et al.* (2006) Lysine methylation as a routine rescue strategy for protein crystallization. *Structure* 14(11):1617-1622.

180. Shi H, Quint DA, Grason GM, Gopinathan A, & Huang KC (2020) Chiral twisting in a bacterial cytoskeletal polymer affects filament size and orientation. *Nat Commun* 11(1):1408.

181. Fujiwara I, Zweifel ME, Courtemanche N, & Pollard TD (2018) Latrunculin A accelerates actin filament depolymerization in addition to sequestering actin monomers. *Curr Biol* 28(19):3183-3192.e3182.

182. Bean GJ & Amann KJ (2008) Polymerization properties of the *Thermotoga maritima* actin MreB: roles of temperature, nucleotides, and ions. *Biochemistry* 47(2):826-835.

183. Blanchoin L & Pollard TD (1999) Mechanism of interaction of *Acanthamoeba* actophorin (ADF/Cofilin) with actin filaments. *J Biol Chem* 274(22):15538-15546.

184. Melki R, Fievez S, & Carlier M-F (1996) Continuous monitoring of P_i release following nucleotide hydrolysis in actin or tubulin assembly uing 2-amino-6-mercapto-7-methylpurine ribonucleoside and purine-nucleoside phosphorylase as an enzyme-linked assay. *Biochemistry* 35(37):12038-12045.

185. Webb MR (1992) A continuous spectrophotometric assay for inorganic phosphate and for measuring phosphate release kinetics in biological systems. *Proc Natl Acad Sci U S A* 89(11):4884-4887.

186. Esue O, Cordero M, Wirtz D, & Tseng Y (2005) The assembly of MreB, a prokaryotic homolog of actin. *J Biol Chem* 280(4):2628-2635.

187. Ozyamak E, Kollman J, Agard DA, & Komeili A (2013) The bacterial actin MamK: *In vitro* assembly behavior and filament architecture. *J Biol Chem* 288(6):4265-4277.

188. Polka JK, Kollman JM, Agard DA, & Mullins RD (2009) The structure and assembly dynamics of plasmid actin AlfA imply a novel mechanism of DNA segregation. *J Bacteriol* 191(20):6219-6230.

189. Singh P, *et al.* (2013) Assembly of *Bacillus subtilis* FtsA: Effects of pH, ionic strength and nucleotides on FtsA assembly. *Int J Biol Macromol* 52:170-176.

190. Kikumoto M & Oosawa F (2017) Thermodynamic measurements of actin polymerization with various cation species. *Cytoskeleton* 74(12):465-471.

191. Mayer JA & Amann KJ (2009) Assembly properties of the *Bacillus subtilis* actin, MreB. *Cell Motil Cytoskeleton* 66(2):109-118.

192. Matsuzaki M, *et al.* (2020) D-Loop mutation G42A/G46A decreases actin

dynamics. *Biomolecules* 10(5):736.

193. Barkó S*, et al.* (2016) Large-scale purification and in vitro characterization of the assembly of MreB from *Leptospira interrogans*. *Biochem Biophys Acta* 1860(9):1942-1952.

194. Popp D*, et al.* (2010) Filament structure, organization, and dynamics in MreB sheets. *J Biol Chem* 285(21):15858-15865.

195. Battye TG, Kontogiannis L, Johnson O, Powell HR, & Leslie AG (2011) iMOSFLM: a new graphical interface for diffraction-image processing with MOSFLM. *Acta Crystallogr D Biol Crystallogr* 67(Pt 4):271-281.

196. Kabsch W (2010) XDS. *Acta Crystallogr D Biol Crystallogr* 66(Pt 2):125-132.

197. Adams PD*, et al.* (2010) PHENIX: a comprehensive Python-based system for macromolecular structure solution. *Acta Crystallogr D Biol Crystallogr* 66(Pt 2):213-221.

198. Emsley P, Lohkamp B, Scott WG, & Cowtan K (2010) Features and development of Coot. *Acta Crystallogr D Biol Crystallogr* 66(Pt 4):486-501.

199. Szatmári D*, et al.* (2020) Intracellular ion concentrations and cation-dependent remodelling of bacterial MreB assemblies. *Sci Rep* 10(1):12002.

200. Castaneda N*, et al.* (2018) Cations modulate actin bundle mechanics, assembly dynamics, and structure. *J Phys Chem B* 122(14):3826-3835.

201. Tang JX & Janmey PA (1996) The polyelectrolyte nature of F-actin and the mechanism of actin bundle formation. *J Biol Chem* 271(15):8556-8563.

202. Shapovalov MV & Dunbrack RL (2011) A smoothed backbone-dependent rotamer library for proteins derived from adaptive kernel density estimates and regressions. *Structure* 19(6):844-858.

203. Inaba H*, et al.* (2022) Generation of stable microtubule superstructures by binding of peptide-fused tetrameric proteins to inside and outside. *Sci Adv* 8(36):eabq3817.

204. Patel A*, et al.* (2017) ATP as a biological hydrotrope. *Science* 356(6339):753-756.

205. Nishizawa M*, et al.* (2021) Effects of weak nonspecific interactions with ATP on proteins. *J Am Chem Soc* 143(31):11982-11993.

206. Dolinsky TJ*, et al.* (2007) PDB2PQR: expanding and upgrading automated preparation of biomolecular structures for molecular simulations. *Nuc Acid Res* 35(suppl_2):W522-W525.

207. Dolinsky TJ, Nielsen JE, McCammon JA, & Baker NA (2004) PDB2PQR: an automated pipeline for the setup of Poisson–Boltzmann electrostatics calculations. *Nuc Acid Res* 32(suppl_2):W665-W667.

208. Tang CL, Alexov E, Pyle AM, & Honig B (2007) Calculation of pKas in RNA:

On the structural origins and functional roles of protonated nucleotides. *J Mol Biol* 366(5):1475-1496.

209. Sitkoff D, Sharp KA, & Honig B (1994) Accurate Calculation of Hydration Free Energies Using Macroscopic Solvent Models. *J Phys Chem* 98(7):1978-1988.

210. Søndergaard CR, Olsson MHM, Rostkowski M, & Jensen JH (2011) Improved Treatment of Ligands and Coupling Effects in Empirical Calculation and Rationalization of pKa Values. *J Chem Theory Comput* 7(7):2284-2295.

211. Rostkowski M, Olsson MHM, Søndergaard CR, & Jensen JH (2011) Graphical analysis of pH-dependent properties of proteins predicted using PROPKA. *BMC Struc Biol* 11(1):6.

212. Olsson MHM, Søndergaard CR, Rostkowski M, & Jensen JH (2011) PROPKA3: Consistent Treatment of Internal and Surface Residues in Empirical pKa Predictions. *J Chem Theory Comput* 7(2):525-537.

213. Mattei S*, et al.* (2020) Structure of native glycolipoprotein filaments in honeybee royal jelly. *Nat Commun* 11(1):6267.

214. Tokmakov AA, Kurotani A, & Sato K-I (2021) Protein pI and intracellular localization. *Front Mol Biosci* 8:775736.

215. Colombo J*, et al.* (2021) A functional family of fluorescent nucleotide analogues to investigate actin dynamics and energetics. *Nat Commun* 12(1):548.

216. Monterroso B*, et al.* (2019) Bacterial FtsZ protein forms phase-separated condensates with its nucleoid-associated inhibitor SlmA. *EMBO rep* 20(1):e45946.

217. Kotila T*, et al.* (2022) Structural basis of rapid actin dynamics in the evolutionarily divergent *Leishmania* parasite. *Nat Commun* 13(1):3442.

218. Ti S-C & Pollard TD (2011) Purification of actin from fission yeast *Schizosaccharomyces pombe* and characterization of functional differences from muscle actin. *J Biol Chem* 286(7):5784-5792.

219. Sasajima Y & Miyata M (2021) Prospects for the mechanism of *Spiroplasma* swimming. *Front Microbiol* 12:706426.

220. Manka SW & Moores CA (2018) The role of tubulin–tubulin lattice contacts in the mechanism of microtubule dynamic instability. *Nat Struct Mol Biol* 25(7):607-615.

221. Ramamurthi KS & Losick R (2008) ATP-driven self-assembly of a morphogenetic protein in *Bacillus subtilis*. *Mol Cell* 31(3):406-414.

222. Wu IL*, et al.* (2015) A versatile nano display platform from bacterial spore coat proteins. *Nat Commun* 6(1):6777.

223. Castaing J-P, Nagy A, Anantharaman V, Aravind L, & Ramamurthi KS (2013)

ATP hydrolysis by a domain related to translation factor GTPases drives polymerization of a static bacterial morphogenetic protein. *Proc Natl Acad Sci U S A* 110(2):E151-E160.

224. Merino F*, et al.* (2018) Structural transitions of F-actin upon ATP hydrolysis at near-atomic resolution revealed by cryo-EM. *Nat Struct Mol Biol* 25(6):528-537.

225. Colavin A, Hsin J, & Huang KC (2014) Effects of polymerization and nucleotide identity on the conformational dynamics of the bacterial actin homolog MreB. *Proc Natl Acad Sci U S A* 111(9):3585-3590.

226. De La Cruz EM & Pollard TD (1995) Nucleotide-free actin: Stabilization by sucrose and nucleotide binding kinetics. *Biochemistry* 34(16):5452-5461.

227. Kasai M, Nakano E, & Oosawa F (1965) Polymerization of actin free from nucleotide and divalent cations. *Biochim Biophys Acta* 94(2):494-503.

228. Reynolds MJ, Hachicho C, Carl AG, Gong R, & Alushin GM (2022) Bending forces and nucleotide state jointly regulate F-actin structure. *Nature* 611(7935):380-386.

List of achievements

Publications

1. **Daichi Takahashi**, Makoto Miyata, "Sequence analyses of a lipoprotein conserved with bacterial actins responsible for swimming motility of wall-less helical *Spiroplasma*", 2023, *microPublication Biology*, *in press*.

2. **Daichi Takahashi**, Ikuko Fujiwara, Yuya Sasajima, Akihiro Narita, Katsumi Imada, Makoto Miyata, "ATP-dependent polymerization dynamics of bacterial actin proteins involved in *Spiroplasma* swimming", 2022, *Open Biology*, 12(10):220083.

3. **Daichi Takahashi**, Ikuko Fujiwara, Makoto Miyata, "Phylogenetic origin and sequence features of MreB from the wall-less swimming bacteria *Spiroplasma*", 2020, *Biochemical and Biophysical Research Communications*, 553(4):638-644.

Chapters 1 is prepared based on Takahashi D *et al*. 2020 *Biochem Biophys Res Commun*. and Takahashi D and Miyata M 2023 *MicroPubl Biol*. Chapter 2 is prepared based on Takahashi D *et al*. 2022 *Open Biol*.

Preprint

1. **Daichi Takahashi**, Makoto Miyata, Ikuko Fujiwara, "Assembly properties of *Spiroplasma* MreB involved in swimming motility", 2023, *bioRxiv*, doi.org/10.1101/2023.01.26.525654.

Chapter 3 is prepared based on the preprint.

Book chapter

1. **Daichi Takahashi**, Ikuko Fujiwara, Makoto Miyata, "Purification and ATPase activity measurement of *Spiroplasma* MreB", 2023, *Bacterial and Archaeal Motility* (*Springer*, ISBN: 978-1-0716-3059-4), chapter 30, *in press*.

Presentations in international meetings (The first author of each was presented)

1. **Daichi Takahashi**, Ikuko Fujiwara, Katsumi Imada, Makoto Miyata, "Polymerization Dynamics and Structure of MreB Proteins Involved in *Spiroplasma* Swimming", 23rd Congress of the International Organization for Mycoplasmology, Online, Nov 2021 (**Oral, with review**)

2. **Daichi Takahashi**, Ikuko Fujiwara, Makoto Miyata, "POLYMERIZATION OF BACTERIAL ACTIN MREB INVOLVED IN SWIMMING MOTILITY OF

SPIROPLASMA ERIOCHEIRIS", BLAST XVI, Online, Jan 2021 (Poster, without review)

3. **Daichi Takahashi**, Ikuko Fujiwara, Makoto Miyata, "DEVELOPMENT OF *SPIROPLASMA* SWIMMING MOTOR FROM BACTERIAL ACTIN MREB", BLAST XVI, Online, Jan 2021 (Poster, without review)

4. **Daichi Takahashi**, Ikuko Fujiwara, Makoto Miyata, "Polymerization of bacterial actin MreB involved in swimming motility of *Spiroplasma eriocheiris*", The 11th Toyota Riken International Workshop "Actin Filament: beyond the atomic resolution structures", Aichi Japan, Nov 2019 (Poster, without review)

5. Ikuko Fujiwara, **Daichi Takahashi**, Yuya Sasajima, Hana Kiyama, Ayami Arakawa, Takayuki Kato, Tomoko Miyata, Shigeyuki Kakizawa, Keiichi Namba, Makoto Miyata, "Bacterial actin homolog, MreBs and fibril are essential for the swimming motility of *Spiroplasma eriocheiris*", The 11th Toyota Riken International Workshop "Actin Filament: beyond the atomic resolution structures", Aichi Japan, Nov 2019 (Oral, without review, invited)

6. **Daichi Takahashi**, Makoto Miyata, "Polymerization of bacterial actin MreB involved in swimming motility of *Spiroplasma eriocheiris*", International Workshop on Quantum Sensing & Biophotonics 2019, Osaka Japan, Sep 2019 (Poster, without review)

7. **Daichi Takahashi**, Makoto Miyata, "Dynamics and Structure of MreB proteins from *Spiroplasma eriocheiris*", 10th OCARINA International Symposium, Osaka Japan, Mar 2019 (Poster, without review)

8. **Daichi Takahashi**, Aya Kodama, Katsumi Imada, Makoto Miyata, "Structure and function of six cytoskeletal proteins in *Spiroplasma swimming*", 22nd Congress of the International Organization for Mycoplasmology, Portsmouth NH USA, Jul 2018 (Poster, without review)

9. **Daichi Takahashi**, Aya Kodama, Katsumi Imada, Makoto Miyata, "Structural and functional analyses of five MreB proteins involved in the swimming of *Sprioplasma eriocheiris*", Joint Congress of The 7th Meeting of the Asian Organization for Mycoplasmology (7th AOM), The 45th Meeting of the Japanese Society of Mycoplasmology (45th JSM), Tokyo Japan, May 2018 (**Oral, with review**)

10. **Daichi Takahashi**, Aya Kodama, Katsumi Imada, Makoto Miyata, "Structure and function of six cytoskeletal proteins in *Spiroplasma* swimming", 9th OCARINA International Symposium, Osaka Japan, Mar 2018 (Poster, without review)

Presentations in domestic meetings and others (The first author of each was presented)

1. **Daichi Takahashi**, Ikuko Fujiwara, Akihiro Narita, Makoto Miyata, "Filament structural polymorphism of bacterial actin MreB", Group meeting for motility 2023, Tokyo Japan, Jan 2023 (Oral, without review)
2. **Daichi Takahashi**, Ikuko Fujiwara, Katsumi Imada, Makoto Miyata, "ATP hydrolysis mechanism of bacterial actin MreB", The 45th Annual Meeting of the Molecular Biology Society of Japan, Chiba Japan, Dec 2022 (Poster, without review)
3. **Daichi Takahashi**, Ikuko Fujiwara, Akihiro Narita, Makoto Miyata, "Filament structural polymorphism of bacterial actin MreB" The 60th Annual Meeting of the Biophysical Society of Japan, Hakodate Japan, Sep 2022 (Poster, without review)
4. **Daichi Takahashi**, Ikuko Fujiwara, Makoto Miyata, "Filament structural polymorphism of bacterial actin MreB", The 22nd Annual Meeting of the Protein Science Society of Japan, Tsukuba Japan, Jun 2022 (Oral, without review)
5. **Daichi Takahashi**, Ikuko Fujiwara, Katsumi Imada, Makoto Miyata, "Structural basis of ATPase activity in bacterial actin MreB3 of *Spiroplasma*", The 49th Meeting of the Japanese Society of Mycoplasmology, Sapporo Japan, May 2022 (Oral, without review)
6. **Daichi Takahashi**, Ikuko Fujiwara, Katsumi Imada, Makoto Miyata, "ATP hydrolysis mechanism of bacterial actin MreB", Group meeting for motility 2022, Nagoya Japan, Jan 2022 (Oral, without review)
7. **Daichi Takahashi**, Ikuko Fujiwara, Katsumi Imada, Makoto Miyata, "ATP hydrolysis mechanism of bacterial actin MreB", The 59th Annual Meeting of the Biophysical Society of Japan, Online, Nov 2021 **Awarded for the student presentation award** (OnDemand Oral presentation, without review)
8. **Daichi Takahashi**, Ikuko Fujiwara, Katsumi Imada, Makoto Miyata, "ATP hydrolysis mechanism of bacterial actin MreB", 4th CREST-PRESTO "Genome programming" joint conference, Online, Nov 2021 (Poster, without review)
9. **Daichi Takahashi**, Ikuko Fujiwara, Katsumi Imada, Makoto Miyata, "ATP hydrolysis mechanism of bacterial actin MreB", The 61st summer school for Young Researchers Society of Biophysics, Online, Sep 2021 (Poster, without review)
10. **Daichi Takahashi**, Ikuko Fujiwara, Katsumi Imada, Makoto Miyata, "Mechanism of ATP hydrolysis bacterial actin MreB of *Spiroplasma*", The 21st Annual Meeting of the Protein Science Society of Japan, Online, Jun 2021 (Poster, without review)
11. **Daichi Takahashi**, Ikuko Fujiwara, Katsumi Imada, Makoto Miyata, "ATP hydrolysis mechanism of bacterial actin MreB", The 1st research exchange meeting for Young Researchers Society of Protein Science, Online, Jun 2021 (Poster, without review)
12. **Daichi Takahashi**, Ikuko Fujiwara, Katsumi Imada, Makoto Miyata, "Structural

basis of bacterial actin MreB involved in *Spiroplasma* swimming", The 94th annual meeting of Japanese Society for Bacteriology, Online, Mar 2021, **Awarded for the excellent presentation award** (OnDemand Oral presentation, without review)

13. **Daichi Takahashi**, Ikuko Fujiwara, Katsumi Imada, Makoto Miyata, "Structural basis of slow P_i release of MreB3 in *Spiroplasma eriocheiris*", 3rd CREST-PRESTO "Genome programming" joint conference, Online, Jan 2021 (Poster, without review)

14. **Daichi Takahashi**, Ikuko Fujiwara, Makoto Miyata, "Polymerization of bacterial actin MreB involved in swimming motility of *Spiroplasma eriocheiris*", 3rd CREST-PRESTO "Genome programming" joint conference, Online, Jan 2021 (Poster, without review)

15. **Daichi Takahashi**, Ikuko Fujiwara, Makoto Miyata, "Development of Spiroplasma swimming motor from bacterial actin MreB", 3rd CREST-PRESTO "Genome programming" joint conference, Online, Jan 2021 (Poster, without review)

16. Ikuko Fujiwara, **Daichi Takahashi**, Yuhei O. Tahara, Yuya Sasajima, Hana Kiyama, Makoto Miyata, "Polymerization of bacterial actin, MreBs from *Spiroplasma eriocheiris*", The 43rd Annual Meeting of the Molecular Biology Society of Japan, Online, Dec 2020, (Oral, without review)

17. **Daichi Takahashi**, "Insight of *Spiroplasma* motility based on Tree of Motility - helicity switching swimming driven by bacterial actin MreB-", The 2nd seminar of Kansai branch in Society of young scientists in biophysics, Online, Oct 2020, (Oral, without review, **invited**)

18. **Daichi Takahashi**, Ikuko Fujiwara, Makoto Miyata, "Development of *Spiroplasma* swimming motor from bacterial actin, MreB", The 58th Annual Meeting of the Biophysical Society of Japan, Online, Sep 2020 (Poster, without review)

19. **Daichi Takahashi**, Ikuko Fujiwara, Makoto Miyata, "Development of *Spiroplasma* swimming motor from bacterial actin, MreB", The 47th Meeting of the Japanese Society of Mycoplasmology, magazine meeting, Aug 2020

20. **Daichi Takahashi**, Ikuko Fujiwara, Katsumi Imada, Makoto Miyata, "Structures and dynamics of bacterial actin homolog, MreB proteins involved in swimming motility of *Spiroplasma eriocheiris*", The 20th Annual Meeting of the Protein Science Society of Japan, Jul 2020, the abstract is opened on the meeting HP (the meeting itself is canceled due to COVID-19)

21. **Daichi Takahashi**, Makoto Miyata, "Development of *Spiroplasma* swimming motor from bacterial actin, MreB", The 93rd annual meeting of Japanese Society for Bacteriology, Aichi Japan, Feb 2020 (Poster, without review)

22. **Daichi Takahashi**, Ikuko Fujiwara, Katsumi Imada, Makoto Miyata, "Bacterial actin

MreB essential for *Spiroplasma* swimming", Group meeting for motility 2020, Kyoto Japan, Jan 2020, (Oral, without review)

23. **Daichi Takahashi**, Ikuko Fujiwara, Makoto Miyata, "Polymerization of bacterial actin "MreB" with novel functions", The 3rd exchange meeting by graduate students in the biology division of the department of biology and geoscience in the graduate school of science of Osaka City University, Osaka Japan, Nov 2019 (Poster, without review)

24. **Daichi Takahashi**, Makoto Miyata, "Polymerization of bacterial actin MreB involved in swimming motility of *Spiroplasma eriocheiris*", The 57th Annual Meeting of the Biophysical Society of Japan, Miyazaki Japan, Sep 2019, (Poster, without review)

25. **Daichi Takahashi**, Ikuko Fujiwara, Makoto Miyata, "Polymerization of bacterial actin "MreB" with novel functions", The 59th summer school for Young Researchers Society of Biophysics, Hyogo Japan, Aug 2019 (Poster, without review)

26. **Daichi Takahashi**, Makoto Miyata, "Polymerization character of actin homolog "MreB" derived from *Spiroplasma eriocheiris*", The 46th Meeting of the Japanese Society of Mycoplasmology, Hokkaido Japan, May 2019 (Oral, without review)

27. **Daichi Takahashi**, Aya Kodama, Katsumi Imada, Makoto Miyata, "Polymerization character of MreB proteins involved in *Spiroplasma eriocheiris* swimming", The 92nd annual meeting of Japanese Society for Bacteriology, Hokkaido Japan, Apr 2019 (Poster, without review)

28. Makoto Miyata, Yuya Sasajima, **Daichi Takahashi**, Hana Kiyama, Shigeyuki Kakizawa, "*Spiroplasma* swims by reversing helices of cytoskeleton", The 92nd annual meeting of Japanese Society for Bacteriology, Hokkaido Japan, Apr 2019 (Oral, without review)

29. **Daichi Takahashi**, Aya Kodama, Katsumi Imada, Makoto Miyata, "Structure and function of six cytoskeletal proteins in *Spiroplasma* swimming", The 2nd exchange meeting by graduate students in the biology division of the department of biology and geoscience in the graduate school of science of Osaka City University, Osaka, Feb 2019 (Poster, without review)

30. **Daichi Takahashi**, "*Spiroplasma* swimming", presentation contest for graduate students in science and technology courses, Osaka Japan, Nov 2018 (Oral, without review)

31. **Daichi Takahashi**, Aya Kodama, Katsumi Imada, Makoto Miyata, "Structural and functional analyses of five MreB proteins involved in swimming motility of *Sprioplasma eriocheiris*", The 56th Annual Meeting of the Biophysical Society of Japan, Okayama Japan, Sep 2018 (Oral, without review)

32. **Daichi Takahashi**, Aya Kodama, Katsumi Imada, Makoto Miyata, "Structure and function of six cytoskeletal proteins in *Spiroplasma* swimming", The 91st annual meeting of Japanese Society for Bacteriology, Fukuoka Japan, Mar 2018 (Poster, without review)

Awards
1. Student presentation award, The 59th annual meeting of the biophysical society of Japan (Nov 2021)
2. Outstanding research award, Public interest incorporated foundation ONO-SYOUGAKUKAI (Sep 2021)
3. Outstanding scholastic attainments award, Public interest incorporated foundation ONO-SYOUGAKUKAI (Sep 2021)
4. Excellent presentation award, The 94th annual meeting of Japanese Society for Bacteriology (Mar 2021)
5. Second place in presentation contest for graduate students in science and technology courses, Osaka University (Nov 2018)